Imperial College London
Department of Bioengineering

# Towards Ultrasound Full-Waveform Inversion in Medical Imaging

Thomas Robins

February 2021

Supervised by Mengxing Tang

Submitted in part fulfilment of the requirements for the degree of
Doctor of Philosophy of Imperial College London
and the Diploma of Imperial College London

PUBLISHED BY THE IMPERIAL COLLEGE OF SCIENCE, TECHNOLOGY AND MEDICINE



*First Edition, February 2021*

# Declaration of Originality

I hereby declare that all material in this thesis other than the contributions that have been properly acknowledged is my own original work.

Thomas Robins

# Abstract

Ultrasound imaging is a front-line clinical modality with a wide range of applications. However, there are limitations to conventional methods for some medical imaging problems, including the imaging of the intact brain. The goal of this thesis is to explore and build on recent technological advances in ultrasonics and related areas such as geophysics, including the ultrasound data parallel acquisition hardware, advanced computational techniques for field modelling and for inverse problem solving. With the significant increase in the computational power now available, a particular focus will be put on exploring the potential of full-waveform inversion (FWI), a high-resolution image reconstruction technique which has shown significant success in seismic exploration, for medical imaging applications. In this thesis a range of technologies and systems have been developed in order to improve ultrasound imaging by taking advantage of these recent advances.

In the first part of this thesis the application of dual frequency ultrasound for contrast enhanced imaging of neurovasculature in the mouse brain is investigated. Here we demonstrated a significant improvement in the contrast-to-tissue ratio that could be achieved by using a multi-probe, dual frequency imaging system when compared to a conventional approach using a single high frequency probe. However, without a sufficiently accurate calibration method to determine the positioning of these probes the image resolution was found to be significantly reduced. To mitigate the impact of these positioning errors, a second study was carried out to develop a sophisticated dual probe ultrasound tomography

acquisition system with a robust methodology for the calibration of transducer positions. This led to a greater focus on the development of ultrasound tomography applications in medical imaging using FWI. A 2.5D brain phantom was designed that consisted of a soft tissue brain model surrounded by a hard skull mimicking material to simulate a transcranial imaging problem. This was used to demonstrate for the first time, as far as we are aware, the experimental feasibility of imaging the brain through skull using FWI. Furthermore, to address the lack of broadband sensors available for medical FWI reconstruction applications, a deep learning neural network was proposed for the bandwidth extension of observed narrowband data. A demonstration of this proposed technique was then carried out by improving the FWI image reconstruction of experimentally acquired breast phantom imaging data. Finally, the FWI imaging method was expanded for 3D neuroimaging applications and an *in silico* feasibility of reconstructing the mouse brain with commercial transducers is demonstrated.

# List of Acronyms

| | |
|---|---|
| **1D** | One Dimension |
| **2D** | Two Dimensions |
| **3D** | Three Dimensions |
| **AIC** | Akaike information criterion |
| **BOLD** | Blood-Oxygen-Level Dependent |
| **CFI** | Colour Flow Imaging |
| **CNN** | Convolutional Neural Network |
| **CT** | Computed Tomography |
| **CTR** | Contrast-to-Tissue Ratio |
| **DNN** | Deep Neural Network |
| **EEG** | Electroencephalography |
| **fMRI** | Functional Magnetic Resonance Imaging |
| **fMRI** | functional Magnetic Resonance Imaging |
| **FPS** | Frames per Second |
| **fUS** | functional Ultrasound |
| **FWI** | Full-Waveform Inversion |
| **GAN** | Generative Adversarial Network |
| **GPS** | Global Positioning System |
| **HU** | Hounsfield Units |
| **IP** | IntraPeritoneal |
| **KIT** | Karlsruhe Institute of Technology |
| **MRI** | Magnetic Resonance Imaging |

| | |
|---|---|
| **NMO** | Normal Move Out |
| **PAM** | PhotoAcoustic Microscopy |
| **PCB** | Printed Circuit Board |
| **PET** | Positron Emission Tomography |
| **PNP** | Peak Negative Pressures |
| **PVA** | Polyvinyl Alcohol |
| **SNR** | Signal-to-Noise Ratio |
| **TOF** | Time-Of-Flight |
| **TRUST** | Transmission and Reflection Ultrasound Tomography |
| **UCA** | Ultrasound Contrast Agent |
| **USCT** | Ultrasound Computed Tomography |

# Contents

# List of Tables

# List of Figures

# Chapter 1

# Introduction

## 1.1 Motivation

Ultrasound imaging is an invaluable modality used in a wide range of clinical applications including obstetrics, cardiovascular diseases and cancer. It has been used throughout patient pathways from disease screening, detection and diagnosis to treatment planning, treatment monitoring and evaluation. Compared to other modalities, ultrasound imaging has the advantages of being real-time, non-ionizing, highly affordable and accessible. While ultrasound has been widely used in both clinical imaging and in pre-clinical research, there are still significant challenges to the existing technology. Currently in a typical ultrasound imaging setup, a short pulse with a central frequency at MHz range, a frequency far beyond what human ears can detect, is transmitted, and echoes received based on which an image can be formed by e.g. delay and sum in the so-called pulse echo imaging. While such methods can work well for imaging soft tissues, it has difficulties in imaging intact brain through the skull, even in small animals when the skull is thin. This is partly due to the significant attenuation, aberration and reflection of ultrasound signal by the skull, and partly due to the assumption of a constant speed of sound in image formation. A number of recent advances in ultrasound imaging and allied areas offer opportunities to address some of the challenges particularly when

imaging the brain. Ultrafast data acquisition at very high frame rate, as well as microbubble contrast agents, can significantly improve the signal to noise ratio obtained. Furthermore, recent advances in exploring tomographic imaging using transmission measurements and advanced computational techniques, in particular the full waveform inversion (FWI), have shown great promise to generate high resolution deep tissue brain imaging even in the presence of bone tissue. In this thesis a number of technological developments were made, taking advantage of the recent advances in ultrasonics and high performance computing, in order to achieve high resolution high tissue contrast imaging in vivo.

## 1.2 Thesis Structure

This thesis is organised as follows:

- *Chapter 2* describes background and literature on a number of current imaging technologies, including pulse echo imaging, functional imaging, dual-frequency imaging, and ultrasound tomography, in order to provide a technological context for the engineering developments reported in this thesis.
- *Chapter 3* will introduce the work, done at the early stage of the PhD, on using ultrafast, dual-frequency, contrast enhanced ultrasound to achieve functional imaging of mouse brain.
- *Chapter 4* describes the development of an imaging data acquisition system using two independently translated clinical ultrasound probes.
- *Chapter 5* reports the development of a 2.5D brain mimicking phantom, and the first experimental demonstration of brain tomography on the phantom using FWI and the data acquisition setup developed in Chapter 4.
- *Chapter 6* reports a deep learning based method for improving 2D FWI imaging by expanding the bandwidth of the measurement data.

- *Chapter 7* describes the initial demonstration of expanding FWI application to 3D small animal brain imaging.

- *Chapter 8* concludes the thesis.

# Chapter 2

# Background

## 2.1 Pulse Echo Ultrasound Imaging

This section provides information on the fundamentals of pulse echo ultrasound imaging. It will provide context for the first part of this thesis, which involves an investigation of ultrasound methods in transcranial neurovascular imaging for functional ultrasound applications.

Pulse echo ultrasound imaging involves the use of ultrasound transducer arrays, each typically consisting of 1D or 2D arrays of piezoelectric elements, to image tissue [Manbachi and Cobbold, 2011]. These arrays are used to both transmit wideband pulses into a medium and detect the resulting backscattered echoes. The goal of pulse echo ultrasound is to reconstruct features in the sonified region using the travel time for reflected ultrasound signals to be received relative to the transmission of ultrasound waves [Szabo, 2014]. This image reconstruction method is referred to as beamforming [Van Veen and Buckley, 1988]. Pulse echo ultrasound is by far the most widely used ultrasound modality, both for medical imaging and in non-destructive testing (NDT) applications [Zhang, 2016], due to being safe, low cost and computational cheap enough for real-time imaging to be performed.

### 2.1.1 Conventional Focused Ultrasound

For a linear array of transducers parallel to the positive x-axis and facing tissue in the positive z-axis, conventional focused ultrasound uses dynamic focusing to form the output image line by line. This is done by insonifying tissue with a narrow beam at the lateral position of each line, $x_f$, using cylindrical transmit delays to focus on a given point $(x_f, z_f)$. For a line produced at $x_f$, the transmit and receive delay of the transmitted wave to a point on the aperture $x_1$ can be described as:

$$\tau(x_1, x_f, z_f) = \frac{(z + \sqrt{z^2 + (x_f - x_1)^2}))}{c} \tag{2.1}$$

However, the resulting image is only at optimal contrast and resolution at the focusing depth, and the resulting image tends to degrade away from this focal area. A multifocus image can be produced through the recombination of partial images using different focal depths, can dramatically reduce the frame rate and so in practice no more than four focusing depths are used.

### 2.1.2 Ultrafast Ultrasound

When compared to the other major imaging modalities, including magnetic resonance imaging (MRI) and computed tomography (CT), ultrasound benefits from being able to perform high frame rate imaging in real-time. For this reason, ultrasound has been applied widely for imaging blood flow dynamics. However, while the acquisition rate for medical ultrasound devices is only limited by the velocity of ultrasound waves through tissue, conventional focused ultrasound requires several sequential transmit events to generate images line by line, giving a practical frame rate of 30-40 frames per second (fps).

To overcome this limitation, a method was proposed by Delannoy *et al.* in 1979 to produce a full frame from a single acoustic pulse using the parallel processing of plane waves [Delannoy et al., 1979]. However, due to the technical limitations in parallel computing at that time this approach would only be fully realised in 1999

by Sandrin *et al.* [Sandrin et al., 1999] in their work on transient elastography. In this work, they demonstrated ultrasound frame rates higher than 5000 fps [Sandrin et al., 1999], albeit of low quality in terms of contrast and resolution compared to conventional focused ultrasound. This reduction in image quality was addressed using coherent plane wave compounding to recover high quality images comparable in terms of contrast, resolution and signal-to-noise ratio (SNR) of the optimal results of conventional multifocus ultrasound without compromising the signal penetration or frame rate [Montaldo et al., 2009]. The results of this work have since been applied to other fields beyond ultrasound electrography, including ultrafast contrast enhanced imaging, high sensitivity ultrafast Doppler imaging and functional Ultrasound (fUS) imaging of the brain [Tanter and Fink, 2014]. The proposed method does, however, assume that the imaged object is not moving as the compounding takes place. This is an acceptable assumption for this application as the head can be fixed relative to the transducer.

### 2.1.3 Coherent Plane-Wave Compounding

For a linear array consisting of $n_t$ transducer elements with the same orientation described in Section 2.1.1, ultrafast ultrasound is used to form a frame using a single wave. By transmitting a unique pulse wave from each of the transducers in the array simultaneously, a single large beam is formed from the combined wave front of these pulses, insonifying the tissue as it propagates in the z-direction. Backscatter of this wave is then received as the echo signal $RF(x_1, t)$.

$$\tau(x_1, x, z) = \frac{(z + \sqrt{z^2 + (x - x_1)^2}))}{c} \tag{2.2}$$

Where the speed of sound c is assumed to be constant in the medium.

When the transmit beam is not focused, the image resolution is obtained through the coherent addition of $RF(x_1, t)$ signals at each point (x, z) by applying a delay of $\tau(x_1, x, z)$ while summing along the array. This calculation is shown in the

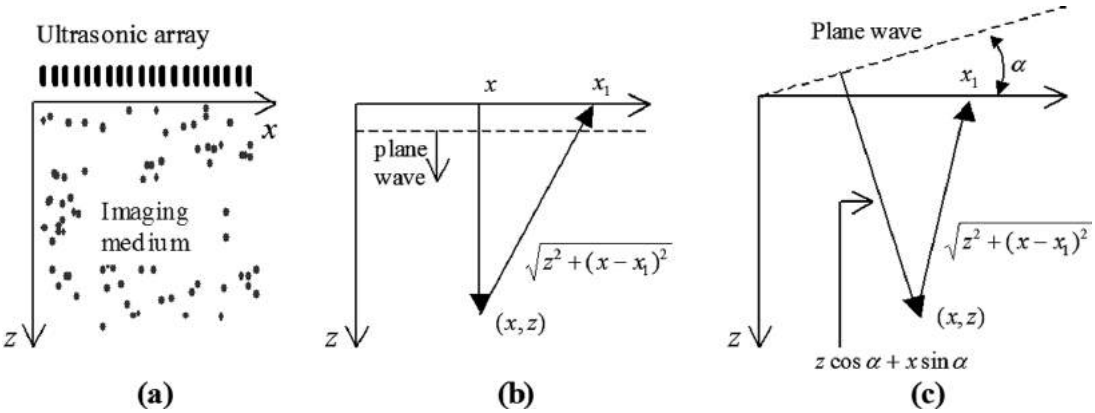


Figure 2.1: (a) Example of transducer orientation (b) time delays for a plane wave propagation with angle 0° (c) time delays for a plane wave propagation with angle $\alpha$. Modified after [Montaldo et al., 2009]

following equation:

$$\mathrm{s(x,z)} = \int_{\mathrm{x-a}}^{\mathrm{x+a}} \mathrm{RF}(\mathrm{x_1}, \tau(\mathrm{x_1}, \mathrm{x}, \mathrm{z}))\, \mathrm{dx_1} \tag{2.3}$$

The low resolution and contrast of the resulting image can be overcome through the compounding of plane wave acquisitions, each produced by applying an angle $\alpha$ in transmission. In this case the transmit time can be found using equation:

$$\tau_{\mathrm{ec}}(\alpha, \mathrm{x}, \mathrm{z}) = \frac{(\mathrm{z}\cos\alpha + \mathrm{x}\sin\alpha)}{\mathrm{c}} \tag{2.4}$$

While the time to return to point $\mathrm{x_1}$ on the transducer can be found by the following calculation:

$$\tau_{\mathrm{rec}}(\mathrm{x_1}, \mathrm{x}, \mathrm{z}) = \frac{\sqrt{\mathrm{z}^2 + (\mathrm{x} - \mathrm{x_1})^2}}{\mathrm{c}} \tag{2.5}$$

The sum of these two time delays, $\tau(\mathrm{a}, \mathrm{x_1}, \mathrm{x}, \mathrm{z}) = \tau_{\mathrm{ec}} + \tau_{\mathrm{rec}}$, can then be used in Equation (2.3) to generate the ultrasound image. The time delays for the plane wave in this case can be seen in Figure 2.1(c).

By compounding coherently, the images obtained over a range of angles (prior to taking the envelope of the beamformed data) undergo a synthetic focusing, providing a focus in the lateral and axial directions. The angles are chosen such

that the focusing is equivalent to that of the optimal results of conventional multi-focus. This results in producing images of comparable quality to those generated using multi-focus imaging but at significantly higher frame rates.

## 2.2 Functional Imaging Modalities

Functional imaging is an area of medical imaging concerned with changes in metabolism and blood flow but it is most closely associated with the study of brain functionality. The imaging modalities used for this task may take the direct detection route, which involves measuring action potentials as the propagation of electrical currents (this includes electroencephalography (EEG), micro-electrode arrays [Miller and Wilson, 2008]) and optical methods (such as light-sheet microscopy [Ahrens et al., 2013]). Alternatively, there are methods which instead measure localised haemodynamic changes in cerebral blood flow to detect brain activation, including positron emission tomography (PET) [Schulz et al., 2011], functional magnetic resonance imaging (fMRI) [Lahti et al., 1998] and photoacoustic microscopy [Yao et al., 2015]. In this section, the advantages and disadvantages of these different modalities will be briefly discussed in terms of their suitability for functional imaging in moving subjects.

### 2.2.1 Electroencephalography and Micro-Electrode Arrays

EEG and micro-electrode arrays offer the highest temporal sampling rates of functional imaging techniques and as such are best suited for the measurement of action potentials, which can propagate along neurons at speeds within the range of 0.50-130 m/s [Anderson, 2010]. There has already been extensive use of both EEG and micro-electrode arrays in freely moving subjects in both clinical and animal model applications, including nanofabricated polyimide-based microelectrodes proposed by Choi *et al.* [Choi et al., 2010]. This puts these modalities at an advantage compared to existing indirect functional imaging

modalities such as fMRI and PET, which have temporal resolutions in the order of seconds and require immobilised subjects. One limitation of EEG and micro-electrode arrays is that spatial resolution in full brain imaging is directly limited by the number of electrodes that can be applied. This disadvantage is not present using the aforementioned indirect methods [Kondylis et al., 2014]. The high-temporal resolution EEG may be acquired simultaneously with other higher-spatial resolution imaging modalities, such as fMRI and functional near-infrared spectroscopy. However, recording from several such devices simultaneously can make matching brain activity challenging, and in the case of fMRI, induction can occur in EEG electrodes due to the large magnetic field of MRI devices. This would not be a problem for imaging modalities such as ultrasound which do not require large magnetic fields [Robins, 2016].

### 2.2.2 Functional Magnetic Resonance Imaging

PET and fMRI are among the most widely used functional imaging modalities whenever a noninvasive method is required for studying brain activation. As indirect methods they are able to image brain activation by detecting haemodynamic changes in the neurovasculature supporting the neurons of the brain. As neuronal activity exceeds immediate oxygen and nutrient supplies, blood vessels need to adapt in order to increase blood flow to these regions and meet the demand. fMRI is able to measure the blood-oxygen-level dependent signal (BOLD) to detect these haemodynamic changes deep into the brain. fMRI is often considered the gold standard for functional imaging and remains one of the most popular of the existing methods, both clinically and when researching small-animal models. It does, however, have limitations. Due to the small size of the animal models, high magnetic fields are required to achieve sufficient spatial resolution (150/350 $ms^{-1}$) [Yu et al., 2010, Yu et al., 2012]. As a result, this provides poor temporal resolution. Furthermore, subjects being imaged using fMRI need to be sedated and secured due to the degradation in image quality brought about by motion (for rodents this could involve the use of anaesthesia, a bite bar and a heated

water pad to maintain rectal temperature [Logothetis, 2008]). These limitations make it difficult to image transient events using fMRI and makes the method unsuitable for in-vivo studies of freely moving animals [Robins, 2016].

### 2.2.3 Photoacoustics

Imaging using the photoacoustic effect involves the delivery of laser pulses to tissue in order to produce broadband ultrasonic waves from thermoelastic expansion of the optical absorption. These ultrasonic waves are then detected using ultrasound transducers and can be used to measure haemodynamic activity in soft tissue at a microvascular level. Fast, functional photoacoustic imagery through animal skull tissue has been proposed by Yao *et al.* using their photoacoustic microscopy (PAM) method for 3D high resolution [Yao et al., 2015]. However, like other optical techniques, this method performs poorly with depth and is not suitable for full brain imaging for penetrations greater that  1 mm.

### 2.2.4 Functional Ultrasound

With the advent of ultrafast plane wave ultrasound, the ability to image at higher frame rates has enabled the measurement of blood dynamics in smaller vessels and at slower flow rates than previously possible using conventional medical ultrasound devices [Bercoff et al., 2011]. This improved sensitivity has allowed for the functional ultrasound imaging of the brain using ultrafast Doppler, a method first proposed by Macé *et al.* in 2011 [Macé et al., 2011]. This power Doppler approach then allows for the measurement of haemodynamic changes in cerebral blood volume for the detection of brain activity at high spatiotemporal resolution. Ultrasound has several advantages over other imaging modalities, such as being low cost, safe and portable. Furthermore, there is evidence that it can provide greater spatiotemporal resolution over existing gold standard functional imaging technologies, such as fMRI and PET in small animal models [Macé et al., 2013]. All of these factors combined indicate that fUS may be a potentially disruptive

functional imaging technology that can applied to areas of neurological research of complex transient behaviour that could not previously be investigated.

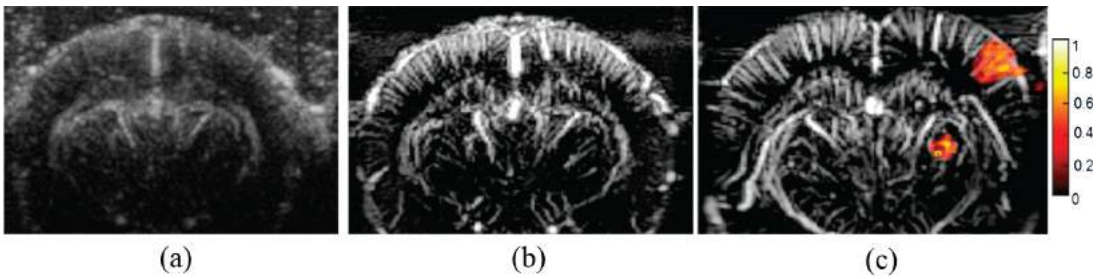


Figure 2.2: Functional imaging of the brain using a) conventional focused ultrasound, b) ultrafast Doppler c) fUS imaging with notable increasing in cerebral blood volume in regions as a response to whisker stimulation

While conventional ultrasound technology is the most widely used image modality for measuring blood flow, the image quality and frame rate trade-offs required for duplex/triplex Doppler modes (where B-mode and Doppler signals are simultaneously processed and displayed) have limited the acquisition of temporal samples in large-field images to below kilohertz frame rates. As a result, this poor sensitivity has limited applications to only imaging the major vessels. By using ultrafast imaging instead of focused ultrasound, a significantly greater number of temporal samples can be acquired per pixel for Doppler processing over a given acquisition time for the whole field of view. Furthermore, by performing coherent compounding on these acquisitions it is also possible to produce images with greater resolution and noise suppression. This gain in sensitivity when using ultrafast Doppler in place of conventional colour flow imaging (CFI) due to these factors can be calculated for a given depth z as:

$$G_{UD}(z) = \frac{S_{UD}}{S_{CFI}} = N_{angles}\frac{\sqrt{\lambda z}}{D}\sqrt{\frac{n_{eff}^{UD}}{|n_{eff}^{CFI}|}} \tag{2.6}$$

Here the signal intensities for ultrafast and conventional CFI Doppler are given by $S_{UD}$ and $S_{CFI}$ respectively, the number of plane wave angles used in the plane wave imaging is $N_{angles}$, the wavelength is given by $N_{Lambda}$, D is the transmit focus aperture used in the conventional CFI Doppler, and the respective time samples available for each method are denoted by $n_{eff}^{UD}$ and $n_{eff}^{CFI}$.

The original method showed great promise in terms of sensitivity and was shown to achieve excellent spatiotemporal resolutions of (∼100 $\mu$m, 50 ms) when using a high frequency probe (∼15 MHz) when imaging brain activation in vivo [Macé et al., 2013] (compared to the poor temporal resolution and spatial resolution limit of fMRI when studying small animal models [Yu et al., 2010, Yu et al., 2012]). However, a craniotomy was required in order to overcome the strong beam attenuation of skull tissue when imaging signal of cerebral blood flow [Droste and Metz, 2004]. This removal of tissue could affect the outcome of neurological studies requiring the natural behaviour of healthy animals and introduces increased risk of infection and brain tissue damage that could negatively affect results. This was recently addressed by Errico *et al.* through the bolus injection of microbubble contrast agent into the circulatory system to improve the SNR of signal traversing the skull, demonstrating that transcranial fUS was feasible at a spatiotemporal resolution of (100 $\mu$m, 1 ms) while claiming imaging was possible up to a depth of 12.5 mm [Errico et al., 2015]. By finding the vascular map produced in these results comparable to those acquired in the thinned skull acquisitions, it was concluded that no aberration correction was required for transcranial fUS through the rat skull. Therefore, contrast enhanced transcranial fUS imaging of the brain shows potential as an imaging modality for use in studies requiring the measurement of transient brain activity of freely-moving subjects.

## 2.3 Dual Frequency

While transcranial fUS has been demonstrated to overcome the attenuation of the skull, the use of a high-frequency probe still places constraints on the imaging depth when skull tissue is present and produces sub-optimal resonance for the microbubble contrast agents. By decreasing the transmit frequency this attenuation can be reduced, allowing for greater penetration depths when imaging [O'Reilly and Hynynen, 2013]. Furthermore, the response from microbubbles is greatest when excitation occurs near the resonant frequency, which tends to be

in the 1-4 MHz range for most commercially available lipid shell microbubbles. This is much lower than the frequencies used in high frequency imaging systems, making it challenging to use these systems for non-linear imaging [Doinikov and Dayton, 2007, Gessner et al., 2010]. Reducing the transmit frequency, however, will also reduce the spatial resolution of the ultrasonic images, preventing the imaging of small blood vessels required for studying the brain. For contrast enhanced imaging, it has been proposed that optimal results could be achieved using a dual frequency system with separate confocal transducer components for transmitting and receiving in different frequency ranges: a low frequency transducer array dedicated to producing transmissions for optimal microbubble excitation and a high frequency transducer array for receiving the high frequency of the broadband ultrasound energy produced by the non-linear behaviour of the microbubbles.

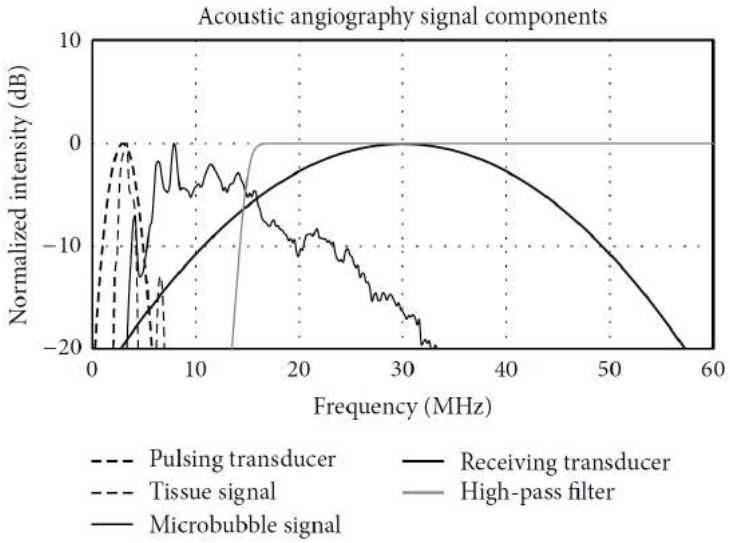


Figure 2.3: Demonstrates the broadband range of microbubble response

The proof of concept for this method was first demonstrated by Kruse *et al.* [Kruse and Ferrara, 2005] using two different transducers to excite and receive signal from microbubbles simultaneously. The results of their dual frequency system showed similar resolution, higher echo signal amplitude and reduced propagation attenuation when compared to that of a single high frequency transducer acquisition. It was also found that the excitation of the contrast agent with pulses

at 2.25 MHz produced broadband energies that exceeded 45 MHz (see Figure 2.3). In more recent work, specialised dual frequency prototypes have been developed and tested *in vivo*, including work by Gessner *et al.* which demonstrated the high resolution, significant tissue suppression and low susceptibility to degradation by tissue motion when using the confocal dual frequency system in their novel acoustic angiography image modality [Gessner et al., 2013]. This confocal system consists of an element made up of two components: a centre 30 MHz transducer element for high frequency reception and a surrounding low frequency annulus transducer element of 4 MHz.

## 2.4 Ultrasound Tomography

### 2.4.1 Full-Waveform Inversion

Full-waveform inversion is an iterative image-reconstruction technique originally developed for imaging the subsurface in seismic exploration applications [Tarantola, 1984].

In conventional FWI the goal is to find a model $\mathbf{m}$ of physical properties that impact the propagation of acoustic waves to explain the observed real-world data $\mathbf{d}$ being inverted. A synthetic predicted dataset $\mathbf{p}$ corresponding to $\mathbf{d}$ can then be defined numerically by solving the forward problem:

$$\mathbf{G}(\mathbf{m}) = \mathbf{p} \tag{2.7}$$

Where $\mathbf{G}$ is the acoustic wave equation solved using a high-order finite-difference time-stepping algorithm. The solution to when running FWI is then to find $\mathbf{m}'$ such that:

$$\mathbf{G}^{-1}(\mathbf{d}) = \mathbf{m}' \tag{2.8}$$

As $\mathbf{G}$ is a non-linear function and cannot be directly inverted [Warner et al.,

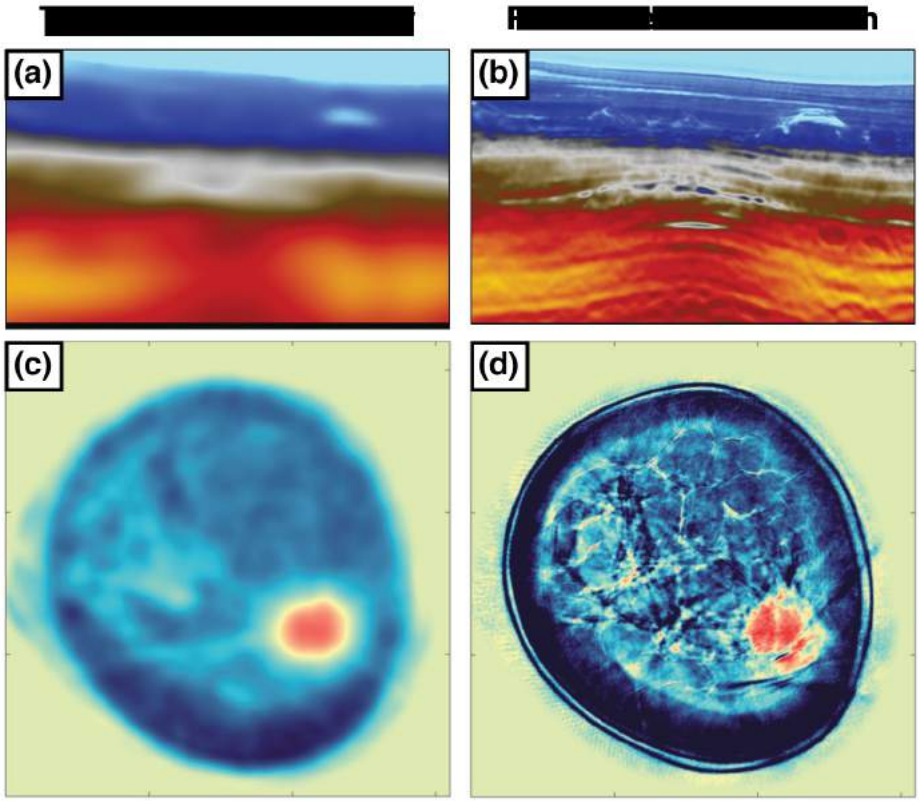


Figure 2.4: **A comparison between travel time tomography and full-waveform inversion in geophysical and medical imaging applications**. (a) & (b) 3D travel time tomography and FWI results when applied to a seismic exploration dataset of petroleum reservoirs in the Western Black Sea. (c) & (c) 2D travel time tomography and FWI results when applied to an *in vivo* ultrasound tomography dataset of a breast.

2013], FWI is instead performed by approximating the Equation (2.8) by solving a non-linear least-squares local optimisation problem with respect to $\mathbf{m}$, giving the objective function:

$$f(\mathbf{m}) = \frac{1}{2}\|\delta\mathbf{d}\|_2^2 = \frac{1}{2}\sum^{n_s}\sum^{n_r}\sum^{n_t}|d-p|_2^2 \tag{2.9}$$

where $n_s$, $n_r$ and $n_t$ are the numbers of sources, receivers and time samples in the data and $f(\mathbf{m})$ is the functional that needs to be minimised. Due to the non-linearity of the problem, the misfit function does not reach the global minimum in one step. Instead the model is updated over several iterations until either the global minimum is reached or a maximum number of iterations is

reached [Virieux and Operto, 2009]. Given $\mathbf{m}_0$ as the model at the start of an iteration, the assumption is made that there is a linear relationship between a small change in the residual between observed and modelled data $\delta\mathbf{d}$ and a small perturbation in the model $\delta\mathbf{m}$ that minimises the objective function given in (2.9), giving the updated model for the next iteration as $\mathbf{m} = \mathbf{m}_0 + \delta\mathbf{m}$. This model update term can be defined as:

$$\delta\mathbf{m} = -\mathbf{H}^{-1}\frac{\partial f}{\partial \mathbf{m}} \tag{2.10}$$

Here $\mathbf{H}$ is the square symmetric Hessian matrix, which contains all second-order differentials of the functional $f$ given in Equation (2.9) with respect to a combination of the model parameters. In practice, inverting the full Hessian is too computationally expensive for this task, so an approximation of only the diagonal values of $\mathbf{H}$ are used instead. Here $\partial f/\partial \mathbf{m}$ is the gradient, which is calculated through an adjoint method [Tarantola, 1984] by performing a forward propagation for each source being modelled and a backward propagation of residual between the observed and modelled data for all receivers. The gradient is found by cross-correlating these two wavefields at every point in the model.

Using the gradient it is possible to determine in which direction to update the model, however it does not provide the magnitude in which the model parameters should be updated. This magnitude is called the step length $a$. This can be computed by perturbing the starting model $\mathbf{m}_0$ (which was used to generate the dataset $\mathbf{d}_0$ and residuals $\delta\mathbf{d}_0$) in the opposite direction to that given by the gradient by a small change $\delta\mathbf{m}$. This gives the model $\mathbf{m}_1 = \mathbf{m}_0 + \delta\mathbf{m}$ which can be used to generate the dataset $\mathbf{d}_1$ and residuals $\delta\mathbf{d}_1$. The step length can then be optimised by assuming a linear relationship between changes in the residuals and changes in the model $\mathbf{m}_a = \mathbf{m}_0 + a\delta\mathbf{m}$ where $a$ minimises:

$$\frac{1}{2}\|\mathbf{d}_a\| \tag{2.11}$$

such that:

$$\delta \mathbf{d}_a = \delta \mathbf{d}_0 + a(\mathbf{d}_1 - \mathbf{d}_0) = \delta \mathbf{d}_0 + a(\delta \mathbf{d}_1 - \delta \mathbf{d}_0)$$

By then differentiating Equation (2.11), setting the differential to zero, $a$ is given by:

$$a = \frac{\delta \mathbf{d}_0^T \mathbf{q}}{\mathbf{q}^T \mathbf{q}} \quad \text{where} \quad \mathbf{q} = (\delta \mathbf{d}_0 - \delta \mathbf{d}_1) \tag{2.12}$$

Finally, once the step length has been calculated, the model update for each model parameter $m_i$ is given by:

$$\delta m_i = \frac{a}{h_{ii}} \frac{\partial f}{\partial m_i} \tag{2.13}$$

where $h_{ii}$ is the approximate magnitude of corresponding diagonal element for the model parameter $m_i$ in the Hessian.

Within the scope of this thesis the acoustic wave equation will be solved while assuming that media can be considered isotropic. Further applications of this FWI method will be discussed in more detail in Chapters 4 to 7.

### 2.4.2 Ultrasound Tomography in Medical Imaging

Breast cancer is globally the most frequently diagnosed cancer in women, and the most frequent cause of death due to cancer [Ferlay et al., 2019]. In recent decades, the introduction of screening programmes to improve early detection and diagnosis of breast cancer has lead to a reduction in the rates of advanced breast cancer and mortality rates [Broeders et al., 2018, Duffy et al., 2020]. Typically, breast-cancer screenings are performed using X-ray mammography due to their high resolution, short acquisition time, and low cost. However, as this modality uses ionising radiation, it poses a non-negligible risk of inducing breast cancer [Miglioretti et al., 2016]. Additionally, it is not recommended for pregnant women.

Furthermore, despite women with dense breast tissue being more likely to be diagnosed with breast cancer than those with less dense breasts, the sensitivity of

mammograms decreases with breast-tissue density, as lesions are more likely to be obscured [Razimi et al., 2019, Harvey et al., 2013]. This has led to a significantly high rate of false negatives in younger women and women with dense breast tissue [Kolb et al., 2002].

In cases where it is not possible to distinguish between cancerous and dense breast tissue, high-frequency US is used to complement mammograms and better characterise lesions [Madjar, 2010]. In addition to being better suited for imaging dense breast tissue, ultrasound-imaging devices are less expensive than the hardware and infrastructure costs required to safely perform X-ray mammography. Furthermore, as ionising radiation is not required, this modality is also significantly safer. However, the conventional pulse-echo ultrasound imaging of the whole breast is currently a time-consuming procedure that needs to be carried out by specialized physicians using hand-held probes, making this approach more costly to perform compared to mammography. Evaluating lesions using ultrasound breast imaging is also highly dependent on the expertise of the clinician, and does not generate high-quality images that can be assessed at a later date. For these reasons, conventional pulse-echo ultrasound is not considered to be suitable as the sole imaging modality for screening programs.

To overcome the limitations of conventional ultrasound in breast imaging, ultrasound computed tomography (USCT) was proposed as a safer and more affordable alternative to mammography. With this approach, hand-held imaging is replaced with arrays of ultrasound transducers that completely surround imaging targets, allowing for the recording of both reflection and transmission data. With these data, tomographic algorithms can be used to reconstruct quantitative models of acoustic breast-tissue properties such as speed of sound (SoS), density, and sound attenuation, allowing for the classification of different breast tissue types and the detection of cancerous masses [Li et al., 2009].

Research into the application of USCT for medical imaging has been ongoing since the 1970s [Greenleaf et al., 1974] and has primarily been applied to breast tissue imaging for cancer detection using time-of-flight (TOF) tomography. In

this approach, the X-ray CT ray approximation is used to model the propagation of acoustic waves and can be considered equivalent to the travel-time tomography method developed for seismic exploration in the infrasound range [Williamson, 1991]. Instead of using the attenuation of signal along these rays like in CT imaging, in USCT TOF tomography models of acoustic properties are reconstructed from travel-time delays of acoustic waves between sources and receivers. These delays are brought about by changes in velocity along the trajectory of ray paths and are typically used to reconstruct speed-of-sound maps [Huthwaite et al., 2010]. This approximation provides a computationally inexpensive method for producing tomograms of the breast [Pérez-Liva et al., 2017] which, like in mammography, can be performed using data acquired quickly by technicians. This allows for clinicians to analyse the resulting quantitative models at a later date using diagnostic imaging software, allowing for this procedure to be more cost effective compared to conventional ultrasound breast imaging. However, as the influence of structures near ray paths are not accounted for when considering this oversimplified model of wave behavior, it has been shown that the maximum theoretical spatial resolution that can be achieved using TOF tomography is limited by the order of the diameter of the first Fresnel zone [Williamson and Worthington, 1993]. Given that many USCT protoypes for breast imaging will consist of transducers transmitting at frequencies around 2 MHz ($\lambda = 0.75$ mm) to ensure the full penetration of the breast, and that the maximum resolution that can be achieved using TOF tomography is $\sqrt{\lambda D}$ where $D$ is the distance between source and receiver elements (which typically range from 200-400 mm), this gives an expected resolution range of 10-15 mm when using these TOF tomography with these devices [Dahlen, 2004]. This prevents this reconstruction approach from being diagnostically useful when screening for breast cancer. Examples for both travel-time tomography reconstruction of petroleum reservoirs and TOF tomography when applied to *in vivo* breast imaging can be seen in Figures 2.4a and 2.4c respectively.

Improvements in available computing power for medical-imaging applications

recently allowed for more computationally expensive USCT techniques to be considered for breast imaging, such as full-waveform inversion (FWI), an iterative data-fitting method that was originally developed for seismic exploration. FWI can be used to produce high-quality, high-resolution reconstructions of 3D breast tissue compared to ray-based USCT methods [Calderon Agudo et al., 2018, Perez-Liva et al., 2020]. To perform FWI, a forward model with a numerical wave equation is used to simulate wave propagation through an acoustic model of the breast being imaged that, when sampled at receiver positions, provides a corresponding synthetic dataset for all source–receiver pairs observed in real data. This acoustic breast model is then updated at each iteration, such that the misfit between observed and synthetic data is minimised. As the full propagation of the wave is modelled, this approach is able to account for multiple scattering in the wavefield, and resolve features at subwavelength resolutions, significantly improving the spatial resolution that can be achieved using ray-based methods.

### 2.4.3 Transducer Positioning Calibration

Given that USCT methods such as TOF tomography and FWI derive acoustic models by modeling the transmission between source-receiver transducer element pairs, the precise positioning of these elements are required to successfully run these algorithms. For data acquired using USCT imaging systems, such as the 3D USCT system being developed for breast imaging at the Karlsruhe Institute of Technology (KIT) [Hopp et al., 2014], the maximum travel-time error that can be tolerated to ensure successfully tomographic reconstructions has been shown to be one fourth of the wavelength used ($\lambda/4$) [Tan et al., 2015]. In the second part of this thesis I will investigate FWI applications in USCT for medical imaging problems using data acquired experimentally using the novel imaging system described in Chapter 4. Due to the nature of this system, which uses rotary and 3D linear motors to provide a high degree of flexibility when positioning the ultrasound probes, the transducer positions are assumed to be unknown for any given experiment. A robust transducer calibration method to estimate these

positions was therefore required without any a-priori information in order to achieve high quality USCT reconstructions. In this section I will review existing transducer position calibration techniques to achieve this. A further discussion about how this USCT data was acquired can be found in Chapter 4. .

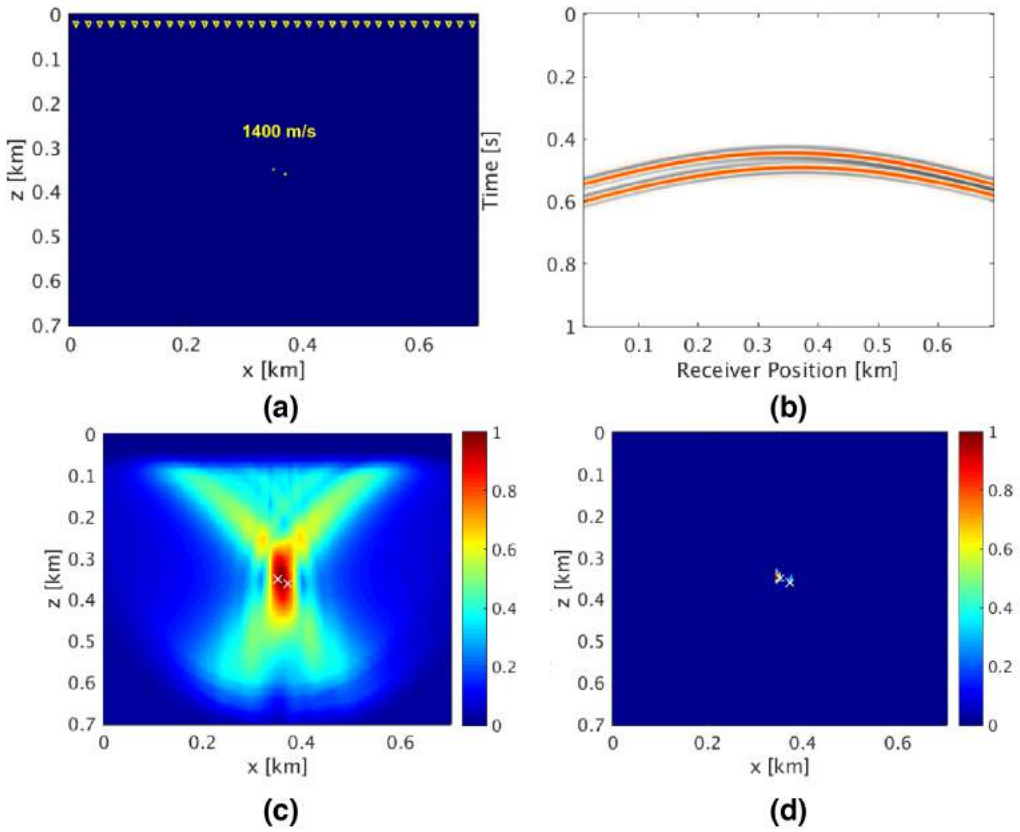


Figure 2.5: **A synthetic example of microseismic source inversion**. (a) Velocity model with microseismic source positions. Receiver positions are indicated by the yellow triangles. (b) Received acoustic data acquired from the two microseismic sources. (c) Back propagation source image. (d) Sparsity-promoting of the microseismic sources (with true positions plotted by white crosses) following 10 preconditioned iterations using the dual formulation of the linearized Bregman algorithm proposed by Sharan *et al.*. Modified after [Sharan et al., 2018]

### Source inversion

FWI has been proposed as a method for source estimation of microseismic events. Here the gradient of the model update used in conventional FWI, as described in Section 2.4.1, is computed using the adjoint state method to model both

the wavelet and spatial radiation of multiple sources simultaneously, allowing for their locations and transmission origin times to be predicted [Kaderli et al., 2015]. However, while the back propagation - also known as time-reversal in photoacoustic applications - of the observed data has been shown to be an effective approach for modelling the wavefield of a given source, blurring in the recovered wavefield can be observed from a lack of aperture and noise, resulting in uncertainties that prevent the precise recovery of source positions. This can be seen in the synthetic microseismic source inversion example shown in Figure 2.5c. To address this problem, sparsity-promoting solutions have been proposed to achieve higher resolution source estimates of sources in both microseismic and photosacoustic imaging problems [Sharan et al., 2018][Sharan et al., 2019]. As these methods allow for the sparse estimation of multiple sources to be performed simultaneously, one exciting application of this approach would be to recover multiple finite point source positions and source wavelet estimates that collectively model the behaviour of larger sources of any given dimension using the Huygens principle [Pinto, 2010]. This could potentially allow for precise modelling of source arrays for 3D USCT applications that cannot be modelled as point sources. However, these methods rely on the relative positions of receivers being known when recovering these sources. When using the experimental setup discussed in Chapter 4, the relative positions of receiving elements within the fixed transducer array of an ultrasound probe can be assumed to be known to a high degree of precision for this task. However, we can not assume to know the true relative positions of multiple transducer arrays for a given scan. The proposed source inversion methods are therefore not ideal for the USCT calibration problem posed in this thesis as both the receiving and source transducer array positions are considered to be unknowns to be solved by calibration.

### Time-of-Flight Based Transducer Calibration

A TOF based auto-calibration method comparable to global positioning systems (GPS) was proposed by Filipik *et al.* to calibrate the positions of source and

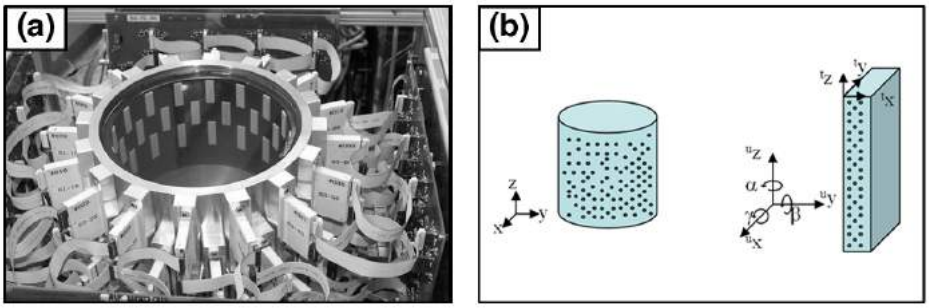


Figure 2.6: (a) The 48 mounted array 3D USCT prototype system developed by KIT. (b) A comparison of co-ordinate systems when solving for the positions in a system of individual element position (left) and a system of transducer arrays (right) using the time-of-flight calibration approach proposed by Filipik *et al.*. Modified after [Filipík et al., 2012]

receiver transducer elements of the 48 mounted array 3D USCT system developed by KIT, as shown in Figure 2.6a. This method was designed while considering all positions and delays to be unknown, which sets it apart from GPS navigation where the orbit of satellites are used as a reference system [Filipík et al., 2012].

In this method, data is first acquired when only water is present to provide watershot data for all source-receiver transducer element pairs. Here we assume the water to be homogeneous with a measured water velocity of $c$. The travel time of a received trace for such a source-receiver pair is given as the measured time-of-flight $\mathbf{MTOF}_p$ for that pair.

Let $\mathbf{x}_s = [x_s, y_s, z_s, \tau]$ and $\mathbf{x}_r = [x_r, y_r, z_r, \tau]$ be vectors for the unknown source and receiver transducer elements and time delays, which are considered to behave as point sources and receivers. The corresponding computed time-of-flight $\mathbf{CTOF}_p$ can then be found as a function dependent on a pair of these element position vectors:

$$CTOF_{\mathrm{p}}(\mathbf{x}_s, \mathbf{x}_r) = \frac{\sqrt{(x_s - x_r)^2 + (y_s - y_r)^2 + (z_s - z_r)^2}}{c} + \tau_s + \tau_r \qquad (2.14)$$

This then gives $\mathbf{MTOF}_p$ and $\mathbf{CTOF}_p$, two comparable vectors for measured and computed travel-times for all source-receiver pairs. The task can then be defined

as finding a set of $\mathbf{x}$ such that the difference between these two vector sets is minimised, giving:

$$minF_p(\mathbf{x}) = \left\{ \frac{1}{2} \|\mathbf{CTOF}_p - \mathbf{MTOF}_p\|^2 \right\} \tag{2.15}$$

where $F_p$ is the residual to be minimised.

The task can then be considered a non-linear least-squares problem where the functional $F$ is minimized iteratively by applying the Gauss-Newton method. For the $k^{th}$ iteration this gives the linear system:

$$\mathbf{J}(\mathbf{x}^k)^T \mathbf{J}(\mathbf{x}^k) \Delta(\mathbf{x}^k) = -\mathbf{J}(\mathbf{x}^k)^T \mathbf{f}(\mathbf{x}^k) \tag{2.16}$$

where $\mathbf{J}(\mathbf{x}^k)$ is the Jacobian matrix of the functional $F$ at $\mathbf{x}^k$ and $\mathbf{f}^k$ is the actual value of the residual. $\mathbf{f}^k$ can therefore be given as:

$$\mathbf{f}_p^k = [f_p^k] = \mathbf{MTOF}_p - \mathbf{CTOF}_p^k \tag{2.17}$$

Finally, $\Delta(\mathbf{x}^k)$ is given as the correction vector to find a new estimate of $\mathbf{x}$ such that the functional is minimized, which is given as:

$$\mathbf{x}^{k+1} = [\mathbf{x}^k] + \Delta\mathbf{x}^k \tag{2.18}$$

This approach is well suited for the calibration problems as presented in this thesis as both the full set of sources and receivers are considered to be unknowns. Likewise, Filipik *et al.* demonstrates that the problem can be simplified by positioning arrays of elements instead of individual elements [Filipík et al., 2012], which is applicable to the dual probe imaging system being developed.

# Chapter 3

# Transcranial Dual Frequency Ultrasound

To develop fUS as a functional imaging modality, in this chapter I explore the application of dual frequency ultrasound to improve the detection of microbubble contrast agents in the brain when imaging through the skull. This work was presented at the iUS 2017 conference in Washington DC (US):

> T. Robins, C. H. Leow, G. Chapuis, P. Chadderton and M. Tang, "Dual frequency transcranial ultrasound for contrast enhanced ultrafast brain functional imaging," 2017 IEEE International Ultrasonics Symposium (IUS), Washington, DC, 2017, pp. 1-4

The material presented at this conferences covers the final parts of this study pertaining to the *ex vivo* [1] and *in vivo* [2] experiments for dual frequency imaging.

For this work I would like to acknowledge the contributions of Gaëlle Chapuis, Sophie Morse and Tiffany Chan for their invaluable help during the *in vivo*

[1] ex vivo : "out of the living". In this context this refers to studies involving biological material that has been removed from an organism. In this work this refers to the use of skull tissue samples for transcranial imaging

[2] in vivo : "within the living". Here this is used to refer to studies of whole, living organisms. This work this involved transcranial imaging of a mouse under anaesthesia

portion of this study.

## 3.1 Introduction

Ultrafast, high sensitivity Doppler imaging has enabled the development of fUS, a novel functional imaging modality that is able to detect haemodynamic changes in small blood vessels at high spatialtemporal resolution ($\sim$100 $\mu$m, $\sim$1 ms). This is sufficient for imaging the neurovasculature of small animals to study complex brain activity. Furthermore, through the introduction of a microbubble contrast agent by bolus injection, it was shown that the attenuation of the skull can be overcome while maintaining a high spatiotemporal resolution, allowing fUS to be performed transcranially without requiring a craniotomy (either by thinning or removing sections of skull). However, the use of high frequency ultrasound probes for high resolution imaging of small blood vessels is not well suited for transcranial ultrasound as the attenuation by the skull is proportional to frequency. Furthermore, these high frequency transmissions can also be considered suboptimal for contrast enhanced ultrasound in that they cannot be used to excite microbubbles close to their resonant frequencies. However, imaging at lower frequencies would in turn decrease the spatial resolution of the images acquired. This would prevent small blood vessels from being imaged which would limit the potential applications of fUS. Alternatively, a dual frequency approach can be considered by transmitting with a low frequency transducer while sampling reflected signals with a high frequency probe. This is based on the observation that microbubbles behave in a non-linear fashion when stimulated, resulting in the emission of broadband ultrasound energy. This behaviour means that when these microbubbles are driven at low frequencies (close to their optimal resonance frequencies) the response will also contain higher frequency harmonics not seen in the transmitted signal. These can be used to resolve microbubbles at high spatial resolutions by filtering for superharmonic signal content. This dual frequency approach could be used to increase the signal strength from contrast agents for

functional imaging while also providing improved tissue suppression and reduced signal attenuation.

To investigate the application of dual frequency for ultrafast fUS, a multi-probe, dual frequency system was designed with a central frequency of 15.63 MHz and transmit frequencies in the 1.50-3.50 MHz range. An *in vitro* flow phantom was assembled to test this system and a method for beamforming dual frequency when imaging using multiple ultrasound transducers was developed. To simulate transcranial imaging, *ex vivo* skull tissue was introduced into these flow phantom imaging problems. Finally, an *in vivo* experiment was carried out to demonstrate dual frequency imaging in mice after microbubbles were introduced into their systems by bolus injection.

## 3.2 Contrast enhanced *ex vivo* transcranial dual frequency ultrasound

For *ex vivo* experiments, perfluorobutane lipid shell microbubbles were used as an ultrasound contrast agent (UCA). These were made in the lab using the procedure described by Sheeran et al [Sheeran et al., 2011]. An 8 mm length of 200 $\mu$m diameter cellulose tubing was placed in the cavity of a macerated mouse skull (female C57BL/6 mouse) to simulate cerebral blood vessel flow. This can be considered to be comparable to an intracerebral artery found in C57BL/6 mice, which range from 100 to 250 $\mu$m [Schambach et al., 2009]. The flow phantom was submerged in a tank of degassed water and received a continuous contrast enhanced flow of $10^6$ Mb ml$^{-1}$ at $\sim$ 0.09 cm $s^{-1}$.

To compare the UCA response for these different methods, a range of peak negative pressures (PNP) were measured for a number of different parameters. This included having the skull present and removed, changing the signal amplitude, using different clincal probes, imaging at different depths and transmitting at

different frequencies. Measurements were acquired using a 0.2 mm needle hydrophone (SN2344, Precision acoustic, Dorset, UK). During the data acquisition, contrast enhanced flow was imaged at 2000 frames/s, both with and without the skull, for 5 different PNPs when driving using the dual frequency or conventional transmit systems. Furthermore, the dual frequency acquisitions were repeated for 3 different transmit frequencies (1.50, 2.00 and 2.50 MHz). Only single angle transmissions were used in this study ($\theta = 0$).

## 3.3 Transcranial Dual Frequency In Vivo

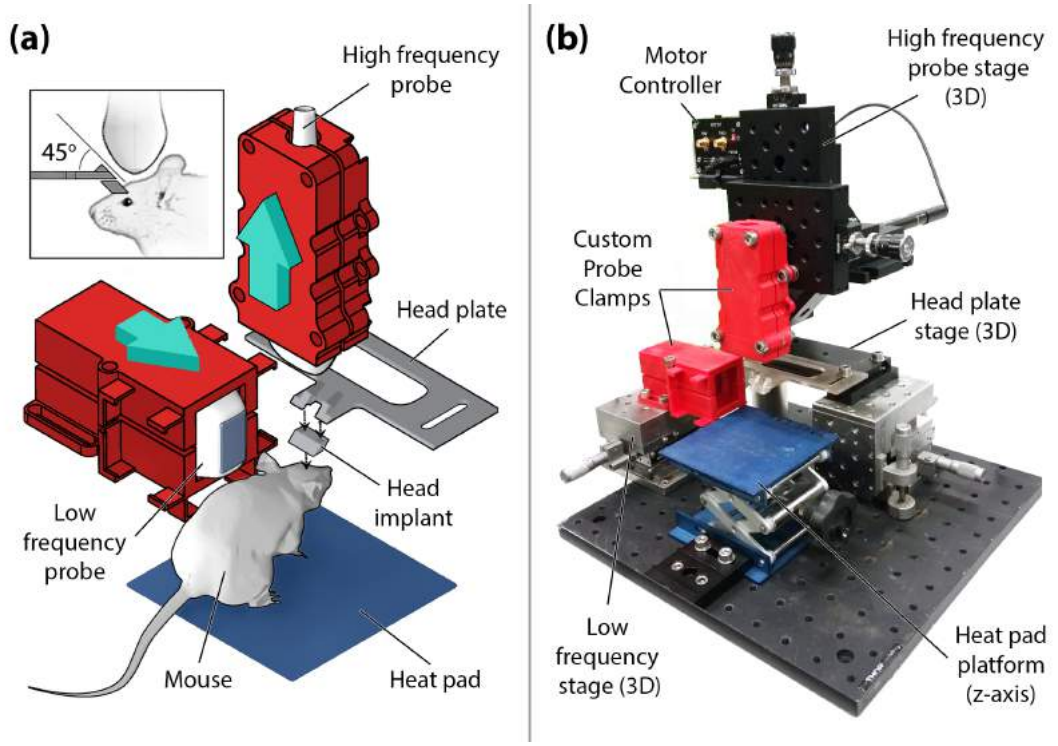


Figure 3.1: **Experimental *in vivo* dual frequency imaging setup**. (a) The implant was designed with a $45^o$ incline to avoid obstructing the high frequency probe casing. The blue arrow indicates low frequency pulse transmission and superharmonic reflection in receive. (b) Photo of the *in vivo acquisition system.*

### 3.3.1 Animal Preparation

For the *in vivo* portion of this study, adult (9 weeks) female BALB/c mice weighing 15-17 g were imaged. Anaesthesia was induced using an intraperitoneal (IP) injection of a fentanyl/midazolam/medetomidine mixture (0.05, 5.00, and 0.50 mg/kg) was maintained by hourly subcutaneous injections of 1/5 of the original dose [Sollini and Chadderton, 2016]. The scalp of the anesthetized mice were then shaved, sterilized and surgically removed to expose the top of the skull. A 3D printed head implant designed for securing the head while imaging was then secured to the frontal bone segment of the mouse skull using a skin adhesive (Histoacryl, Braun, Kronberg, Germany) before being more securely fastened using acrylic dental cement. The head implant and complementary head plate can be seen in Figure 3.1. The care and handling of animals used for this study were performed in accordance with the United Kingdom Home Office guidelines [ASP, 2014].

### 3.3.2 Experimental Setup and Data Acquisition

As shown in Figure 3.1a, to create a large shared imaging region for the dual frequency system, both probes were positioned so that their apertures lie on the same plane while fixed at $90^0$ to each other. As a result, all scattered echoes detected by the high frequency probe are received perpendicular to the direction of the low frequency transmission. This can be used to receive scatterers that produce omnidirectional reflections, such as oscillating microbubbles. Cardiac phase array probes P4-1 (*ex vivo* study, elements: 96, element width: 0.050 mm, pitch: 0.295 mm, ATL, Bothell, WA, US) and P4-2v (*in vivo* study, elements: 64, element width: 0.2500 mm, pitch: 0.300 mm, Verasonics, WA, US) were used to transmit and receive at low frequencies, ranging from 1.5-3 MHz. As the imaging depth of the low frequency probe is small ($\sim$ 20 mm), these transducers

are used to generate linear plane waves when performing dual frequency. For all experiments, an L22-14v small animal probe (centre frequency: 15.625 MHz) was used as the high frequency receive transducer (elements: 128, element width: 0.098 mm, pitch: 0.100 mm, Verasonics, WA, US). This probe was placed above the skull during each experiment to image in the coronal plane. The position of each transducer could be adjusted in 3 axes by manual stages and motorized actuators (Thorlabs Inc., Newton, NJ, US).

The transmission and acquisition of ultrasound signal using both probes was controlled as a single custom 256 element transducer by an ultrafast ultrasound research scanner (256 Verasonics Vantage system, WA, US) using scripts run in Matlab (MathWorks, Natick, MA, US).

### 3.3.3 *In vivo* pilot study

A bolus of 200 $\mu$l of 100% Sonovue microbbuble UCA was intravenously injected into a mouse through the tail vein, allowing for approximately 5 minutes of contrast enhanced brain imaging before the UCA are removed from the circulation. During this 5 minutes, the single frequency system was used to acquired cerebral blood flow imaging for 5 of the highest PNP it can achieve through mouse skull (70, 80, 90, 100 & 110 kPa), over 3 compounding angles, (max $3^o$). The decreased attenuation experienced in transmit meant the dual frequency system was less constrained in terms of achievable PNP and instead had a PNP range of (110, 170, 230, 290 & 350 kPa), which was repeated for transmit frequencies 2.00, 2.50 and 3.00 MHz.

To provide a transmit medium, ultrasound gel was applied to the heads of the mice. This gel had been centrifuged to ensure that is was degassed before being applied. A heat mat at $31^o$C was placed under the mouse to reduce the risk of hypothermia.

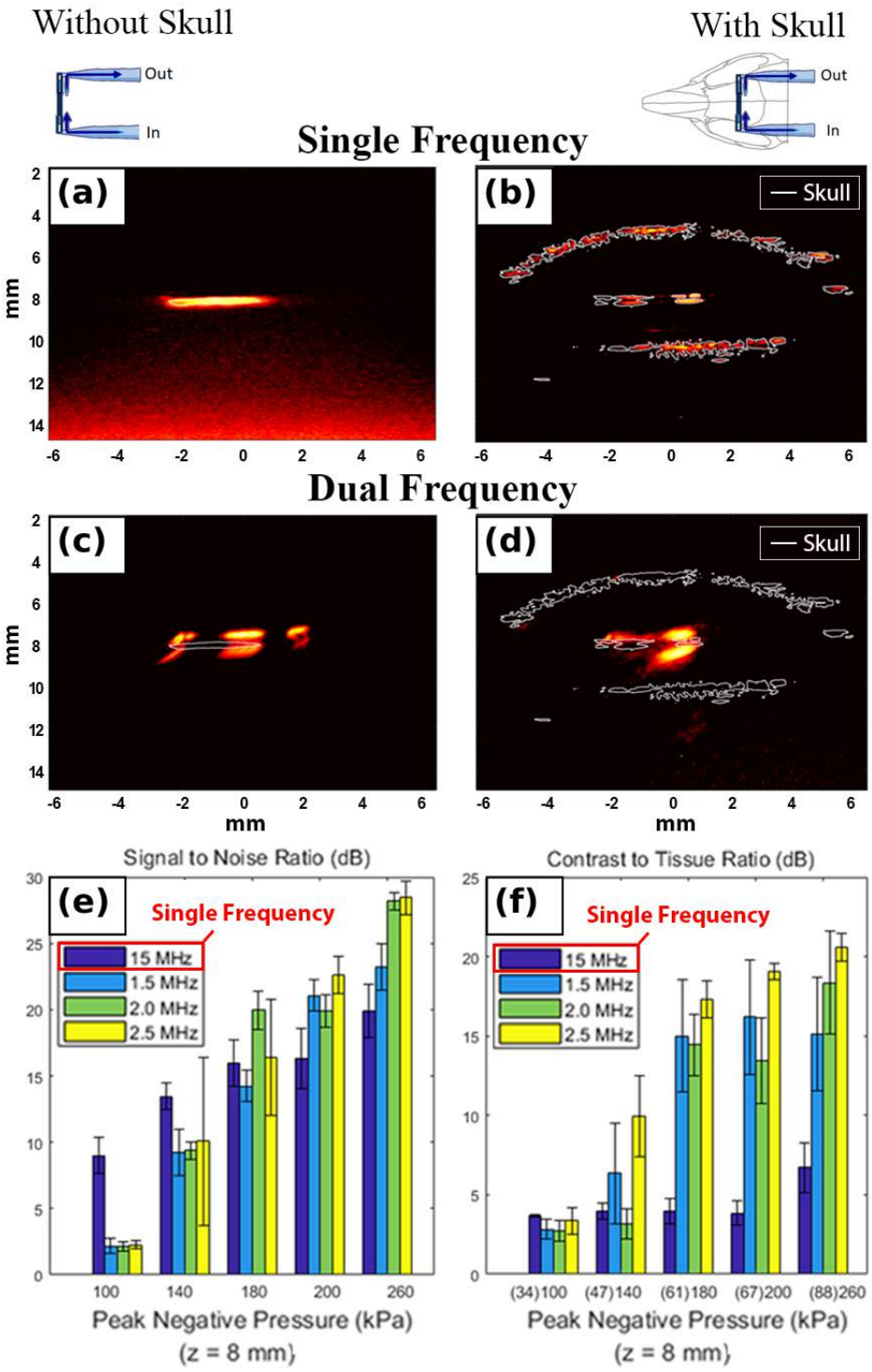


Figure 3.2: **Ex vivo single and dual frequency vascular imaging through a mouse skull**. (Top Left) Flow phantom without mouse skull. (Top Right) Flow phantom with mouse skull. (a-b) Vascular imaging with a single L22-14v transducer, with and without the mouse skull. (c-d) Vascular imaging with a dual frequency setup (P4-1 in transmit, L22-14v in receive), with and without the mouse skull. (e) Signal-to-noise ratio comparison for single frequency (15 MHz) and dual frequency (1.5-2.5 MHz) for a range of peak negative pressures, without the mouse skull. (f) Contrast-to-Tissue ratio comparison for single frequency (15 MHz) and dual frequency (1.5-2.5 MHz) for a range of peak negative pressures, with mouse skull.

### 3.3.4 Image processing

As described in [Demené et al., 2015], spatiotemporal clutter filtering by singular value decomposition was used alongside power Doppler processing to detect the blood flow signal.

## 3.4 Results

From the *ex vivo* results shown in Figure 3.2e, a stronger UCA response can be seen as PNP is increased, as indicated by the higher SNR values for all transmit frequency cases. These SNR values were measured by sampling regions of flow signal and noise values at equal depths. For PNP values at 180 kPa and greater, it can also be seen that the dual frequency system produced a greater UCA response compared to the single frequency system. This supports the observations by Kruse *et al.* who suggested that a strong microbubble response can be detected by driving the microbubbles at their resonant frequency while receiving with a high-frequency probe (centered at 15 MHz). This was observed to be greater than the signal acquired when transmitting and receiving with the same high frequency probe (for a given range of PNP values) [Kruse et al., 2003]. Despite the resonant frequency range of microbubbles being significantly lower than 15 MHz (resonance is microbubble dependent, but they are typically within the 1.5-4.0 MHz range), a high-power, high-frequency response can be detected at frequencies higher than 12 MHz due to the superharmonic response generated by oscillating microbubbles. A high pass filter with a cutt-off frequency at 10 MHz can then be used to isolate this high frequency superharmonic signal from the other, linear microbubble reflections at lower frequencies and those linear reflections from the surrounding tissue. This results in ultrasound data that effectively only contains reflections from microbubbles.

As shown in Figure 3.3f, in addition to increasing SNR (after exceeding the

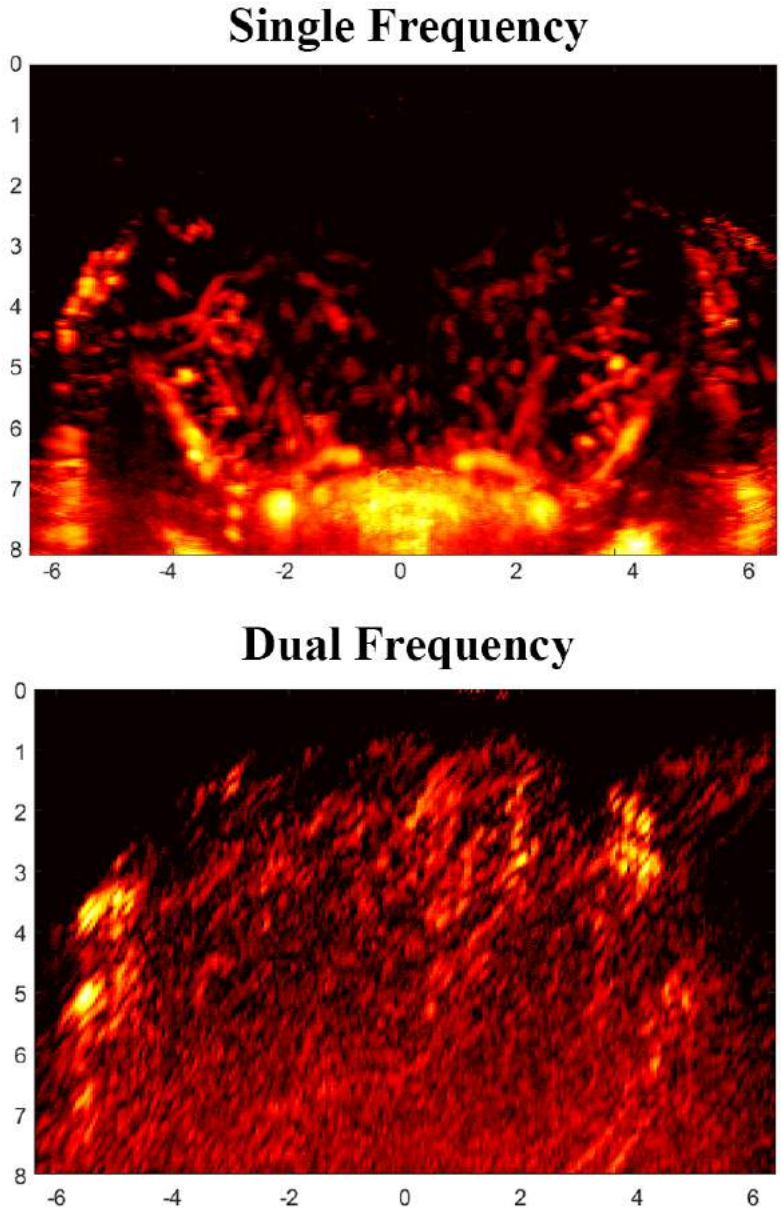


Figure 3.3: **In Vivo results**. (Top) Maximum intensity projection for single frequency (PNP = 110 kPA) coronal acquisition at P56. (Bottom) Maximum intensity projection for dual frequency (3MHz transmit, PNP = 350 kPA) coronal acquisition at P56 during microbubble destruction.

180 kPa PNP threshold), the dual frequency system demonstrated excellent tissue suppression when imaging through the macerated mouse skull. A +12 dB gain in CTR can be observed when comparing the highest CTR measured in the single frequency system and the dual frequency system. This is due to the linear reflections of the skull being filtered out when selecting for the high frequency superharmonic signal. Here it is worth noting that due to the attenuation of the skull, the effective PNP within the skull is severally reduced when trying to transmit through the skull with a high frequency signal using the single frequency system. Conversely, the low frequency transmission when using the dual frequency system was less affected by attenuation and was able to penetrate the skull to stimulate microbubbles at PNP greater than 110 kPa (little microbubble response was detected when driving microbubbles below this value).

When comparing the SNR and CTR values in Figure 3.3 for the different dual frequency transmission frequencies (1.5-2.5 MHz), the highest SNR and CTR values detected was found when transmitting with a signal with a 2.5 MHz centre frequency for PNP values greater than 200 kPa. This suggests that the resonant frequency of the microbubbles being imaged was likely close to or greater than 2.5 MHz. Images acquired from *in vivo* experiments where a mouse brain was imaged using with both the single and dual frequency imaging systems can be seen in Figure 3.3. The single frequency system performed well and acquired images comparable to the initial transcranial functional ultrasound paper by Errico *et al* [Errico et al., 2016]. Contrast enhanced flow allowed for the flow through the neurovasculature of the mouse brain to be detected through the mouse skull, allowing for structures of the brain to be observed. While the *ex vitro* results demonstrated the feasibility of using the dual frequency system for transcranial imaging of flow through a mouse skull, this was not observed when imaging the mouse brain using the dual frequency system *in vivo*. While some microbubble signal was observed, they could not be resolved into individual microbubbles be used to image neurovasculature due to uncertainties in the relative positions of the dual probe. This created travel time errors to resulted in the distorted dual

frequency image seen in Figure 3.3. Furthermore, while the microbubble signal using the single frequency system lasted the duration of the image acquisition, in the dual frequency experiment only a short burst of microbubble signal was observed. This suggests that the signal from the low frequency probe resulted in the destruction of microbubbles that was not observed in the *ex vivo study*.

## Conclusion

To summarise, this study has demonstrated that dual frequency imaging can produce a stronger microbubble response and has excellent tissue suppression compared to using a single high frequency probe and conventional pulse-echo imaging. To investigate the application of this phenomena for transcranial imaging in small animals, a novel neuroimaging acquisition system was designed to allow dual frequency neuroimaging to be performed without transducers being obstructed by a stereotaxic frame. Using this imaging system, *ex vivo* experiments were performed to demonstrate the feasibility of dual frequency when imaging through mouse skull tissue and to optimise imaging parameters to generate the strongest microbubble response and acheive the greatest suppression of tissue signal relative to the microbubble UCAs being imaged. From the *ex vivo* experiments discussed in Section 3.4 it was determined that the highest CTR was observed when imaging through the mouse skull while using a PnP of at least 200 kPa while transmitting in a frequency range close to 2.5 MHz. In addition to this, to perform the *in vivo* imaging experiments, the state of art for contrast enhanced transcranial neurovascular imaging as proposed by [Errico et al., 2015] was achieved. However, it can also be seen in Figures 3.2 and 3.3 that there is poor resolution and erroneous reconstructions in the dual frequency results when compared to the single frequency system. This is most likely due to the misalignment between the transmitting and receiving transducer arrays, resulting in travel time related errors when beamforming. Further work is therefore required to calibrate the positions of these ultrasound probes.

An additional area of investigation would be to improve the performance of the dual frequency imaging by exploring alternative configurations of the two ultrasound probes. A demonstration of one such alternative configuration can be seen in Figure 3.4. Both transducers were aligned along the length of their arrays while the P4-1 transmitted down at a 45 $^{o}$ angle and the high frequency probe was aligned vertically above the imaging target. This configuration was designed to more closely represent imaging with a single transducer probe capable of dual frequency imaging. Preliminary results from using this configuration to image contrast enhanced flow in a 300 $\mu$m were promising, as shown when comparing the single frequency and dual frequency Bmode images shown in Figure 3.4b and Figure 3.4c. By filtering for only the non-linear microbubble signal, the latex tubing seen in the single frequency Bmode image is no longer visible in the dual frequency image, allowing for the positions of microbubbles in the flow to be clearly seen.

Despite the focus on non-linear, vascular flow being investigated in this chapter being in contrast with the more ultrasound tomography focused research discussed in the remainder of this thesis, solving for this multi-probe, dual frequency system was the original inspiration for the dual probe imaging approach that was developed following this work. Likewise, the dual frequency imaging system described here was the precursor to what became the dual probe imaging system system discussed in Chapter 4.

Inspired by the multifunctional capabilities of MRI scanners, which are capable of performing both structural imaging using conventional MRI and functional imaging using fMRI, the ability to acquire both high resolution structural and temporal information from acoustic dataset suggests that there may also be great potential for tomographic ultrasound imaging systems that can simultaneously perform these tasks. For this reason, returning to functional ultrasound imaging methods, such as the one discussed in this chapter, to explore how they may be applied alongside transcranial ultrasound tomography methods remains an

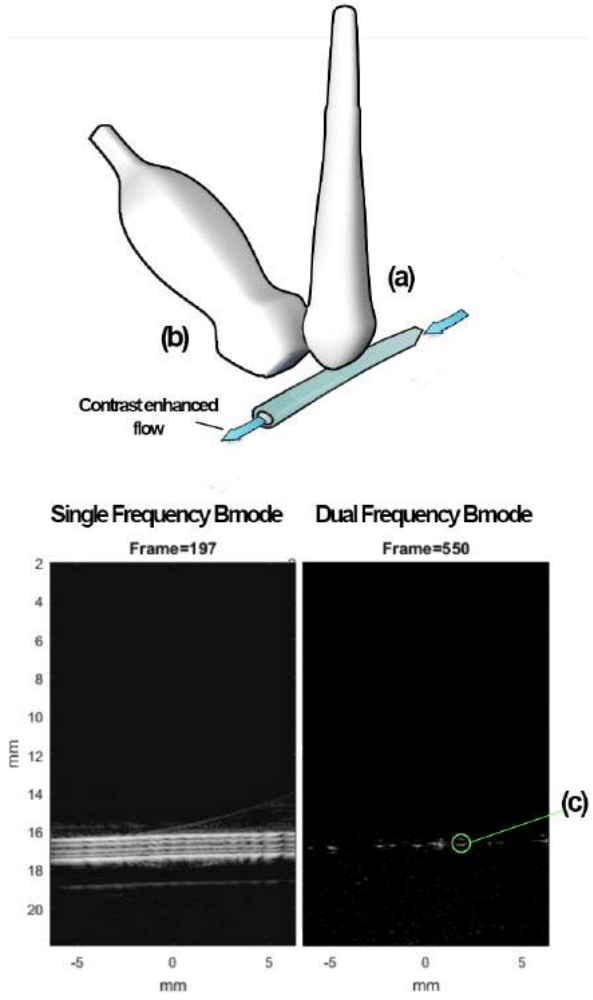


Figure 3.4: **Small angle multi-probe**. (a) High frequency probe held in place to receive signal from the contrast enhanced flow, (b) Angled low frequency transmit probe driving UCA in the 300 $\mu$m latex tube, (c) Individual/ small clusters of microbubbles can be clearly distinguished while little signal from the vessel is received. Bottom Left: B-mode results for single frequency acquisition, Bottom Right: B-mode results for dual frequency acquisition after correcting for different transducer positions.

exciting area of research for future work.

# Chapter 4

# Dual Probe Imaging System for Ultrasound Tomography

In this chapter I will cover the hardware and software solutions related to the development of the dual clinical probe imaging system that was used to acquire ultrasound computed tomography (USCT) data for the ultrasound tomography applications discussed in Chapters 5 to 7.

I would like to acknowledge the contributions of researchers who I worked alongside in the development of this imaging system as part of the Transmission and Reflection Ultrasound Tomography (TRUST) team, including: Javier Cudeiro (Department of Earth Science and Engineering, Imperial College London) who designed the perspex water tank and support structures of the imaging rig, and Carlos Cueto (Department of Bioengineering, Imperial College London), who contributed towards the development of the VerasonicsControl software used to control the dual probe imaging system. I would also like to acknowledge Oscar Calderon Agudo for providing software solutions for computing the wiener filter source matching used to calibrate source wavelets for use in FWI. Components for this imaging rig were acquired using a combination of funding allocated to the TRUST research project and from EPRSC for this PhD studentship.

## 4.1 Introduction

While originally setting out to explore the potential of using multiple probes to perform transcranial dual frequency imaging, while investigating solutions for calibrating multiple probe positions the direction of this PhD research project became increasingly focused on the field of ultrasound tomography. In these applications much larger arrays of transducers are typically used to fully image targets and acquire data in both transmission and reflection. These ultrasound datasets could then be used to solve inverse problems using tomographic algorithms to reconstruct models of acoustic properties, including acoustic velocity, density, echogenicity and attenuation [Li et al., 2009]. This field therefore provided a rich source of literature for the calibration of transducer positions and for modelling source transmissions within multi-transducer systems [Filipík et al., 2012]. It also became apparent that acoustic tomography was by no means an area of interest exclusive to medical imaging and there existed extensive literature of acoustic tomography in geophysics for seismic exploration and the study of earthquakes at the infrasound scale [Thurber and Ritsema, 2018].

It was at this time that I was invited to join the transmission and reflection ultrasound tomography (TRUST) cross-disciplinary research group created by Professor Mengxing Tang and Professor Mike Warner as a collaboration between the Bioengineering and Earth Science and Engineering Departments at Imperial College London. The original goal of this collaboration was to explore the potential of translating tomographic techniques developed in geophysics to medical imaging problems. This followed the recent demonstration of applying full-waveform inversion (FWI) for 3D imaging of a simulated human head *in silico* using Fullwave3D [Warner et al., 2013], a sophisticated FWI software package developed by the FULLWAVE imaging team.

To demonstrate the feasibility of applying FWI to medical imaging problems with real-world data, I designed a low cost and versatile dual probe USCT acquisition system using off-the-shelf and readily available imaging hardware. Here I will

discuss the assembly of this experimental acquisition system, the selection of ultrasound clinical probes used for imaging and finally the calibration methods used to allow FWI reconstructions to be performed using data acquired using this system.

## 4.2 Dual Probe USCT Acquisition System

As shown in the overview of the dual probe imaging system provided by Figure 4.1, this system consists of a pair of 3-axis linear motors ( BiSlide, Velmex, NY, US), placed either side of a large perspex water tank. These allow for the precise computer controlled 3D positioning of ultrasound probes and sensors within the tank. When rotary imaging sequences are used, a primary large aperture rotary motor (Standa, Lithuania) and smaller, secondary rotary motor (PRMTZ8/M, Thorlabs, Inc., NJ, US) can be introduced into the experimental setup, as discussed in Section 4.2.

Imaging tasks were performed in the centre of this water tank, as shown in the photo of the experimental setup provided in Figure 4.1b. This was to mitigate against the detection of signal from any reflective surfaces outside of the imaging region of interest, such as the surface of the water, the walls of the tank and any submerged support structures.

As demonstrated by the overhead shot seen in Figure 4.1c, imaging was performed using a pair of conventional ultrasound probes positioned to transmit and receive to one another while also being able to receive any potential reflections. These probes were connected to the two 128 channel ports of an ultrafast 256 Vantage acquisition system (Verasonics, WA, US) to control the transmission of sources across both probes while acquiring USCT data across all transducer elements acting as receivers. However, given the limited aperture of conventional medical transducers, the imaging region that can be sonified by only one set of stationary probe positions is limited.

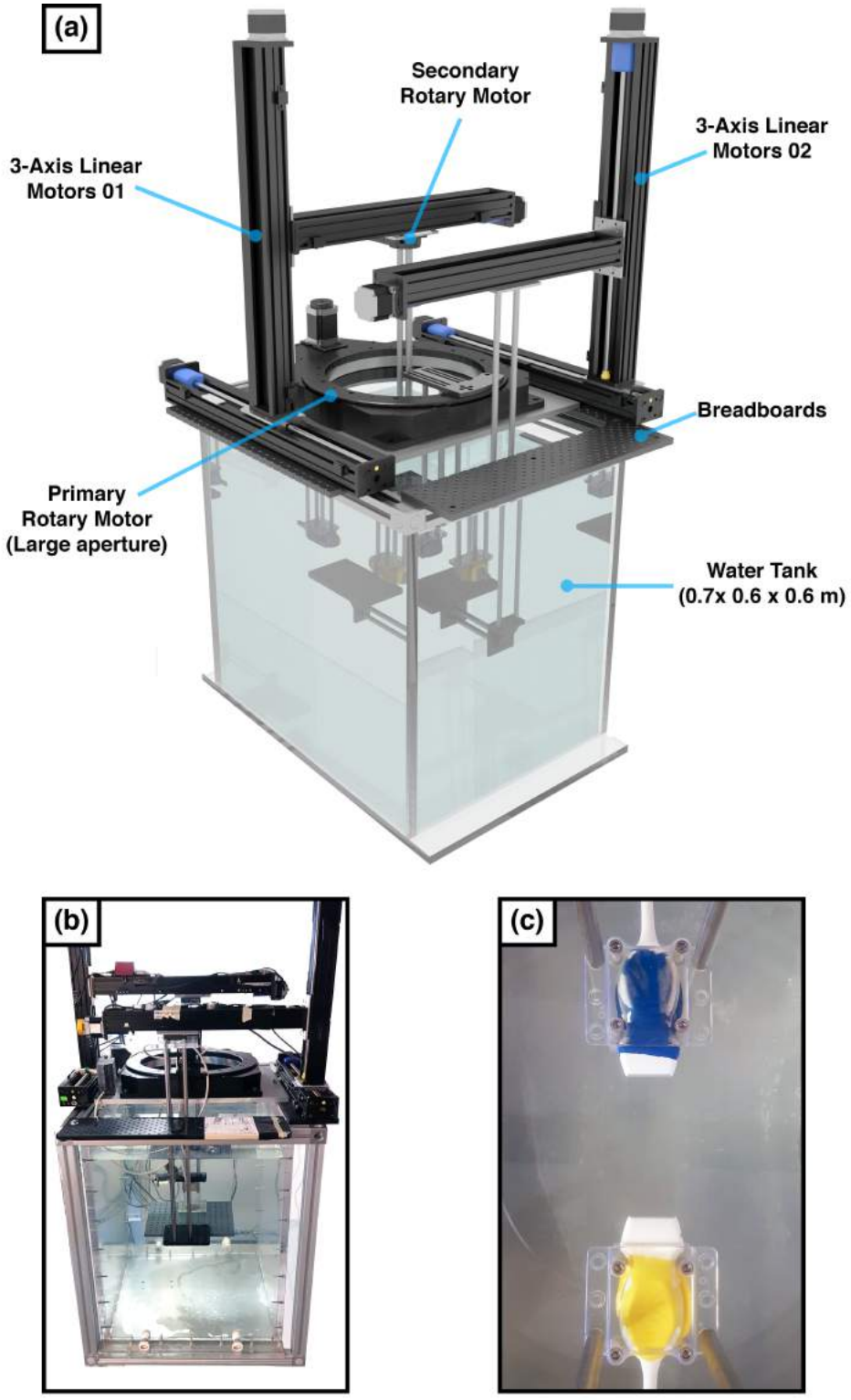


Figure 4.1: **Overview of the dual probe ultrasound imaging system in the rotary configuration**. (a) 3D Render providing an overview of motors used in the system. (b) Front facing photo of the system (c) Top down photo of the dual P4-1 probes in initialised positions.

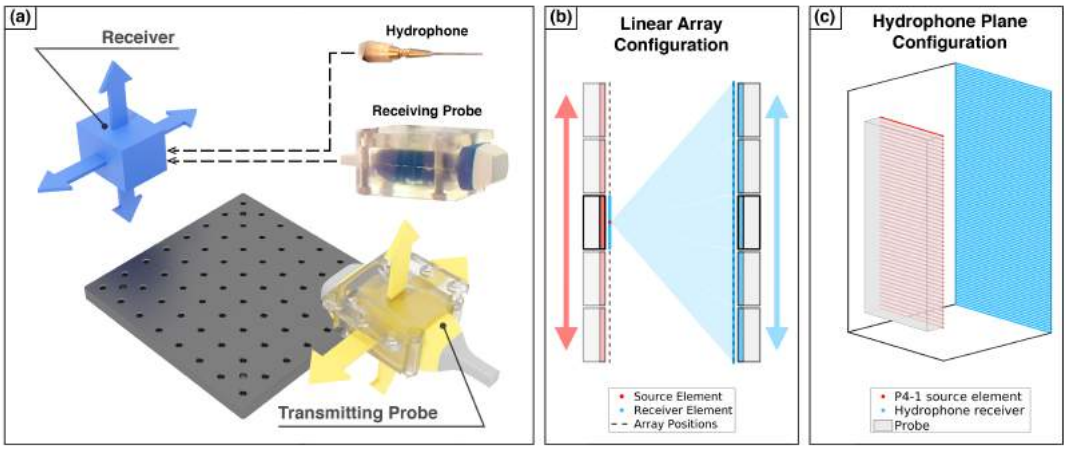


Figure 4.2: **Plane array imaging with the dual probe acquisition system** (a) A render of plane array configuration. Here the receiver could be a second clinical probe or a hydrophone depending on the imaging task. (b) The resulting linear array configuration for 2D USCT imaging using 5 transducer arrays either of the imaging region. (c) The resulting hydrophone plane of [113 101] hydrophone positions used to image the wavefield produced by transducer elements.

Therefore, to simulate much larger transducer arrays, these probes were independently translated using the acquisition system motors using commands provided by an input imaging sequences.

In this chapter we will discuss two such imaging sequences and the resulting configuration of transducer arrays they produce: **(1)** plane array translations, where each probe is translated using the linear motors, and **(2)** rotary array configuration, where both probes are rotated about an imaging target to provide full $360^o$ acquisitions.

### Plane Array Configuration

A simple method for extending the imaging range using the dual probe system was achieved by using imaging sequence that applies linear translation steps using the 3-axis linear motors. By translating each probe along a 1D trajectory parallel to the image regions, the effective aperture of each transducer can be extended by introducing new source and receiver positions into the system for imaging problems. An example of this can be seen in Figure 4.2b where linear arrays consisting of five probe position either side of the imaging region are formed to

allow the probes to image objects much larger then themselves. To acquire a full USCT dataset using this approach, an imaging sequence can be given to acquire data for all unique probe position combinations. For this application we assume that the imaging target is invariant in time for the duration of the scan, nor would we expect there to be a significant change in water velocity (which can be measured before and after imaging experiments).

Alternatively the linear motors can also be used to image over a 2D grid of receiving positions by also including vertical motor steps into the imaging sequence. This can be used to create a grid of hydrophone receiving positions to form a large receiving plane array, as shown in Figure 4.2c, which can be used to characterise the full 3D transmission of clinical probe source elements. To allow for a hydrophone to be passed into the Vantage 256 system as part of an imaging sequence, a simple printed circuit board (PCB) was designed and fabricated for use as a custom BNC-Verasonics interface. This was to allow for individual single channel ultrasound sensors to be passed as inputs into individual channels of a Vantage system cannon plugs. To achieve this, the plug and cable of a decommissioned ultrasound probe was repurposed so that the individual micro coaxial cables could be isolated and soldered to single channel BNC plug connectors.

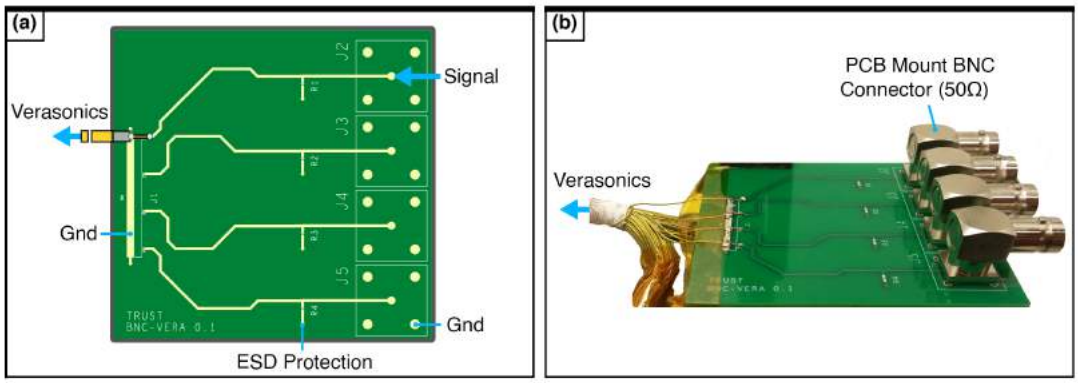


Figure 4.3: **BNC-Verasonics custom interface.** (a) PCB layout for the BNC-Verasonics interface. (b) Photo of the BNC-Verasonics interface with micro-coaxial cables and PCB mounted BNC connectors soldered in place.

### Rotary Array Configuration

To allow for full 360° Deg scans to be performed, the dual probe system can be setup in the rotary array configuration by introducing rotary motors, as shown in Figure 4.4. The size of the imaging region could then be adjusted by changing the radius of the resulting ring array formed by these rotated transducer array positions.

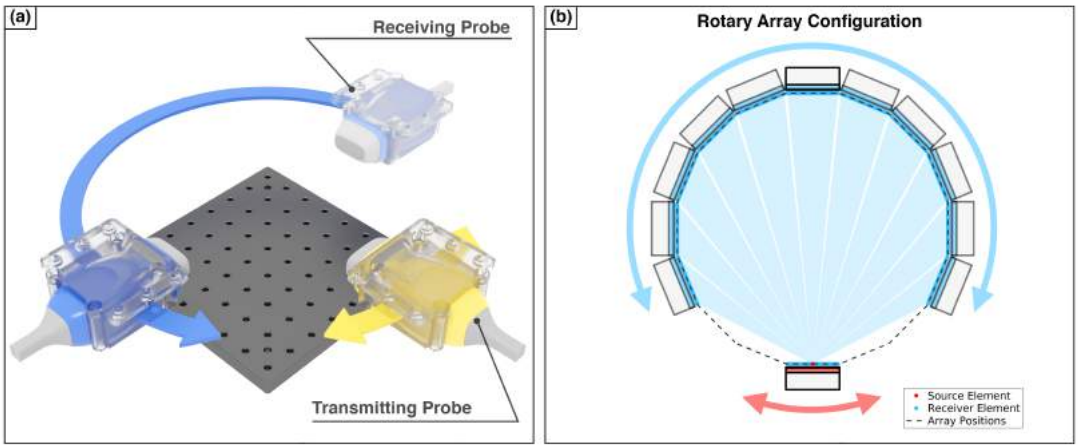


Figure 4.4: **Rotary array imaging with the dual probe acquisition system**

An example of such a ring array can be seen in Figure 4.4b. Here one probe can be designated as a source array while the second probe acts a receiver. For a given source array position, to resulting wavefields generated by the source elements can then be sampled by the receiving array at all possible receiver array positions. In practice, to avoid collisions between these probes a buffer regions of 2 array positions was created either side of the source array, (given a ring array of N positions, roughly 68% of transducer array positions can then used as as receiving positions). However, by setting the source array to also receive, directly reflected signal can also be received (this is also indicated in Figure 4.4b by the blue receiving positions along the aperture of the source array). Full USCT datasets can then be acquired by repeating this imaging sequence for all possible source array positions. This data can then be considered comparable to the data acquired across the elements of a fixed ring array.

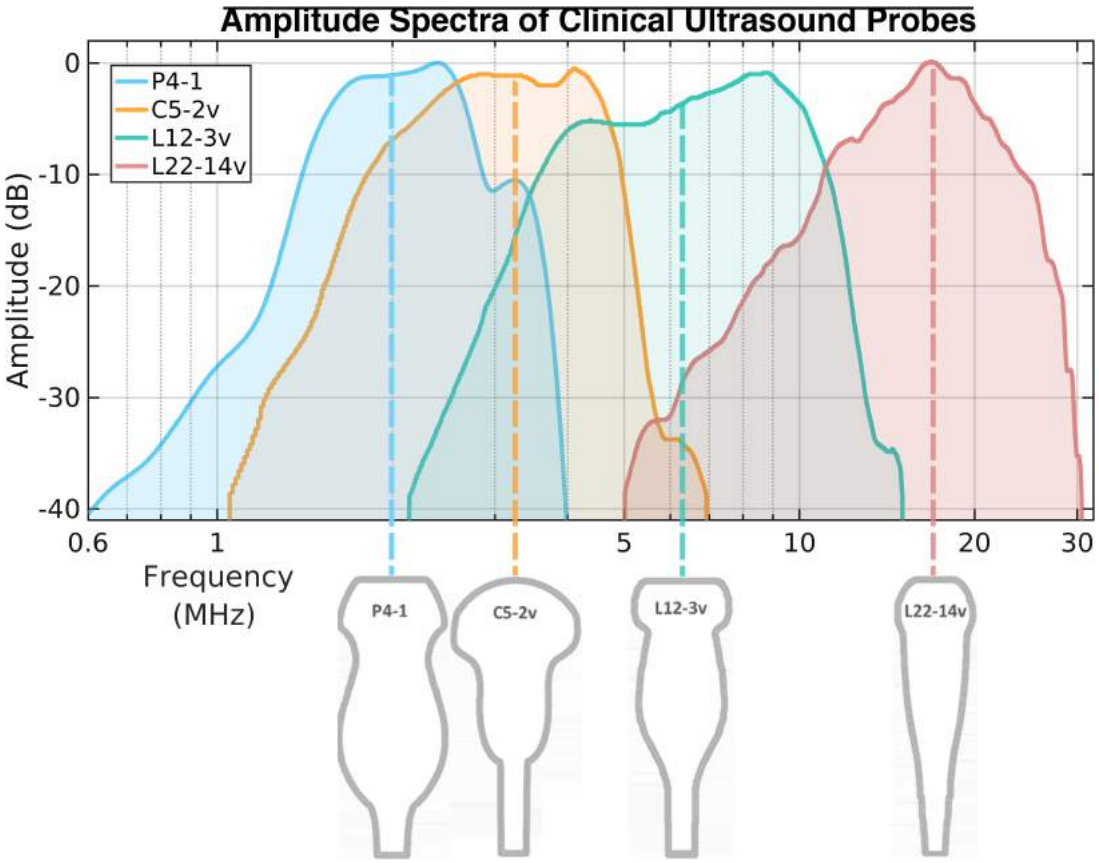


Figure 4.5: **Amplitude spectra for commonly found clinical ultrasound probes**

## 4.3 Ultrasound Probe Selection

To accommodate the diversity of the different applications of ultrasound imaging, there are a range of different clinical probe designs with varying aperture dimensions, bandwidths and centre frequencies. Here a number of these probes are compared in Table 4.1 as potential candidates for the dual probe imaging system.

The number of elements within the transducer array is significant as the ultrafast Vantage acquisiton system is able to transmit and receive data faster than it takes for probes to be translated by motors before imaging can take place again. Larger arrays could therefore mean fewer motor steps to improve the efficiency of imaging sequences, making long, multiplexing probes such as the L12-3v well suited to such tasks. As discussed in Section 2.4.3, many calibration and reconstructions rely on the assumption that transducer elements can be

assumed to be point sources. This can be assumed for transducers with small elements, such as the L22-14v.

However, the main deciding factor for selecting probes for this task will be on the ability to transmit and receive at low frequencies. This reasoning can be seen when noting that the design of USCT systems for breast imaging tend to have lower frequency transducers around 2 MHz to ensure there is sufficient penetration of the whole breast [Huthwaite et al., 2010]. For transcranial applications even lower frequencies tending towards the sub MHz range are required to overcome the strong attenuating effects of skull tissue [Smith et al., 1978]. From *in silico* FWI breast and transcranial imaging studies, even lower frequencies are sought after as inversions can fail due to cycle skipping, which occurs when the initial synthetic and real data are found to have a phase difference of more than $90^o$ [Calderon Agudo et al., 2018].

As can be seen in the comparison of ultrasound probes in Figure 4.5, it's clear that the P4-1 probe has the lowest frequency imaging capabilities. This is because these probes are designed to penetrate deep into the chest for cardiac imaging. This can also be said to be true for the P4-2v, another cardiac probe that also images in a similar range of frequencies. However, as the P4-2v only has 64 elements and the P4-1 has 96, the latter is still a better selection for the dual probe imaging system. The amplitude spectra for the C5-2v, L12-3v and L22-14v seen plotted in Figure 4.5 were all provided by the datasheets for these sheets by their manufacturer (Verasonics, WA, US). The amplitude spectra for the P4-1 was collected in the lab using hypdrophone measurements.

Table 4.1: A comparison of commonly found clinical ultrasound probes

| **Clinical Probe Height (mm)** | **Number of elements** | **Pitch (mm)** |
|---|---|---|
| L22-14v | 128 | 0.10 |
| L12-3v | 192 | 0.2 |
| C5-2v | 128 | 0.506-0.510 |
| P4-2v | 64 | 0.298-0.0302 |
| P4-1 | 96 | 0.295 |

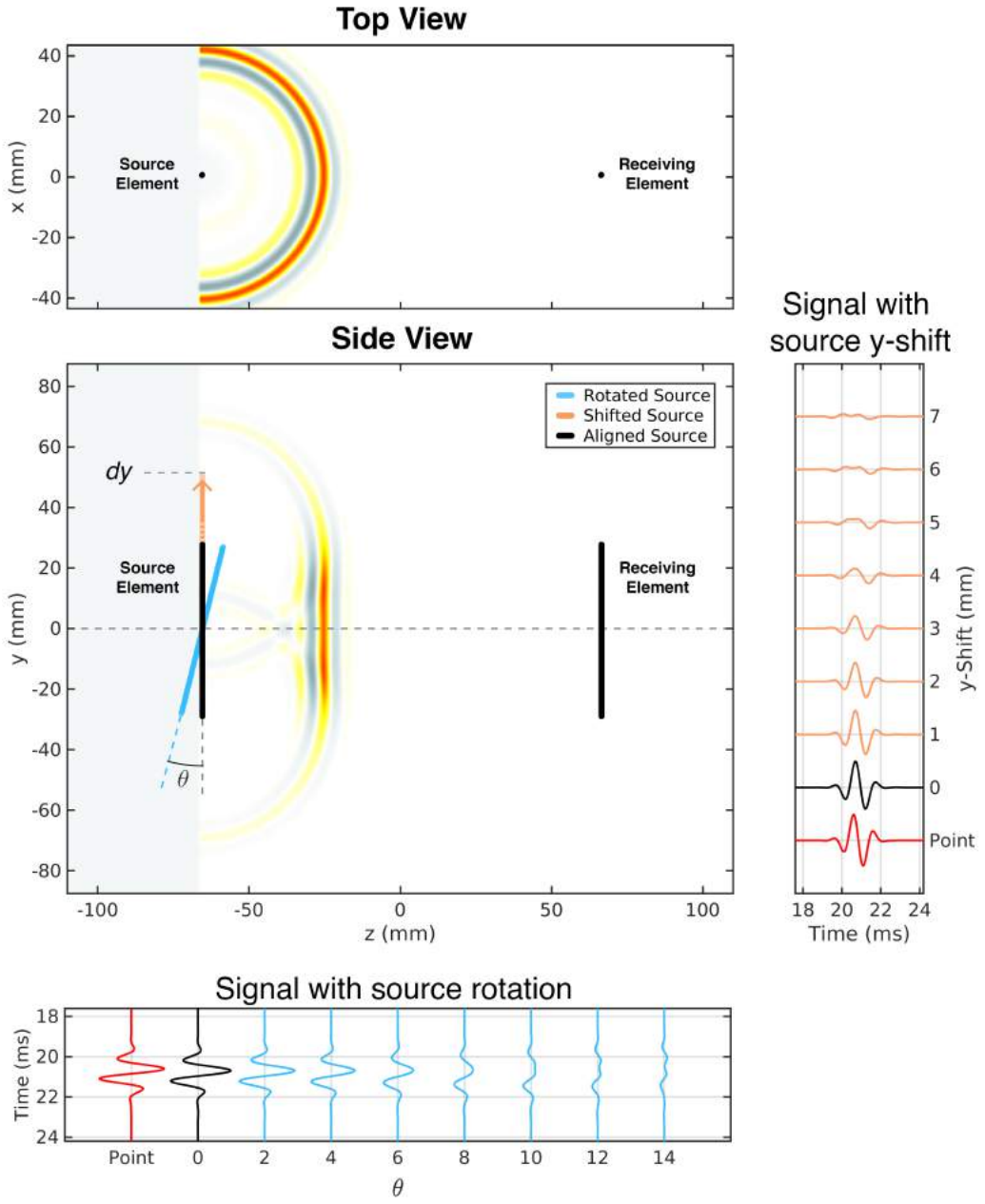


Figure 4.6: **Changes in received signal between two P4-1 elements with source rotation and shift in the y-direction**

## 4.4 Dual Probe Alignment

A challenging aspect of the P4-1 probe, however, is that while it has thin transducer elements when measured in the lateral direction (width = 2.45 x $10^{-1}$), which is ideal for modelling each element as a simple point source and receiver, they are also very long along their height (height$\simeq$13 mm). This was not a significant

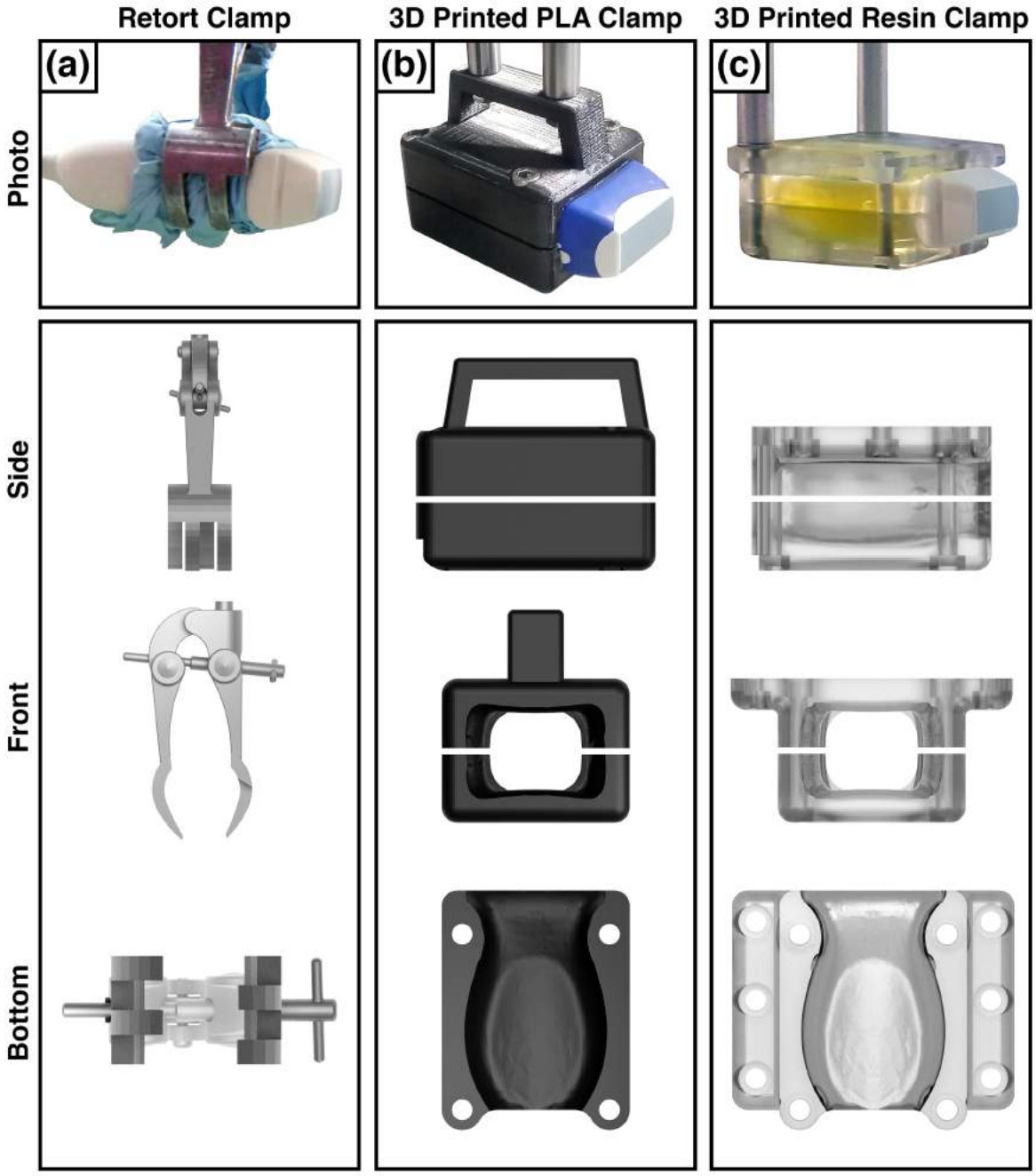


Figure 4.7: **Probe clamping solutions**. (a) Retort clamp holding the P4-1 probe level with padding for protection. (b) Front facing photo of the system. (c) Top down photo of the dual P4-1 probes in initialised positions.

problem for the FWI applications discussed in Chapters 5 and 6, however, as for these studies 2D FWI was used. For 2D applications the cylindrical sources can instead be modelled as points in the 2D plane. However, for this assumption to be valid it is vital for these probes to be positioned so that their elements are aligned with the vertical axis. This can be seen in Figure 4.6 which shows the received

signals of a P4-1 element transmitting to another P4-1 element as rotation and translation errors are introduced. As seen in the top view, when a cross-section is taken of the resulting wavefield, the P4-1 element appears to behave as a point source with a spherical wavefront. In reality, as can be seen in combination with the side view, this transmission is really a cylindrical wave. Should the source element be aligned vertically while both P4-1 elements are aligned with the vertical axis, the received (plotted in black) for this source-receiver can be considered comparable to the received signal of a true source-receiver point element pair, as seen plotted in red. As shown by the other plots, this results in a significant loss of amplitude in the received signals and the assumption that these elements can be modelled as points can no longer be considered valid.

To ensure that these probe elements remained vertically aligned throughout imaging sequences, custom 3D printed probe clamps, as shown in Figure 4.7, were designed. These were created by acquiring a high resolution micro-CT scan of a P4-1 probe so that a precise surface model of the probe could be extracted. Once the basic clamp had been designed as a CAD model, the P4-1 surface model was used to create a precisely matched mould of the probe, as seen in the FDM 3D printed clamp prototype seen in Figure 4.7b and the final SLA clamp design 3D printed in resin seen in Figure 4.7c.

Finally, prior to every imaging experiment, the linear motors are used to ensure that the dual probes are level and facing. This can be achieved by acquiring USCT for different travel times between probes by applying a stepping sequence of fine motor steps in the vertical and horizontal directions over 100 steps (typically with step sizes of 0.30 mm). By sampling traces of directly opposing source-receiver element pair, a vertical and horizontal correction is applied until the amplitude for the received signal for this element pair is maximised. Once this had been achieved, it would then be possible to model the elements of these dual probes as point sources and receivers for 2D USCT imaging applications.

## 4.5 Dual Probe System Calibration

### 4.5.1 Transducer position calibration

Due to the nature of the data acquisition, which involves the translation of the imaging probes, differences are likely to arise between expected and real transducer positions. Likewise, the SoS of water and source wavelets may also change between experiments due to environmental conditions such as temperature. An example of this can be seen in Figure 4.8, which shows a watershot USCT acquisition for a single element transmitting to a set of receiving transducer array positions. If we were to assume that all receiver array positions were at the provided nominal receiver positions, we would expect to observe the nominal travel times plotted in black. However, in practise this assumption would result in the travel time errors observed when comparing this set of nominal TOF values to the true TOF of each trace plotted in blue. Travel time errors would likewise arise should the water velocity value be significantly different to the true water velocity. For this reason, we initially consider the water velocity, transducer positions and source wavelets to be unknown parameters that need to be estimated. These are required to accurately reproduce the transmitted wavefields when modelling the experimental acquisitions.

An estimate for water velocity was found by measuring the travel time through water between the probes over a range of distances using a linear stepper motor. Using these acquisitions, the water velocity was found as the rate of change of travel time between source-receiver pairs as a function of distance. Given that the probes were aligned and facing each other, let $t_0$ be the initial travel time between two opposing probe elements, $t_n$ be the travel time for the same source-receiver pair after $n$ linear motor steps of size $x$ in the axial direction and $N$ the total number of steps. An estimate for water velocity $c$ is then given by:

$$c = \frac{\sum_{n=1}^{N} \left( \frac{nx}{t_n - t_0} \right)}{N}$$

In practice, the travel time differences were found by cross-correlating each new trace with the initial watershot trace and taking the position of the resulting maxima.

To estimate the position of transducer elements we developed a and time-of-flight (TOF)-based element-localisation method based on the USCT calibration approach proposed by Filipik *et al* [Filipík et al., 2012]. As discussed in Section 5.2.2, for each experiment a corresponding watershot dataset was acquired for calibration purposes. Using the measured water velocity value $c$, the TOF value of a given watershot trace can be considered to be the sum of the time required to traverse the distance $d$ from a source to a receiver (with coordinates $[x_s, y_s, z_s]$ and $[x_r, y_r, z_r]$ respectively), plus a system delay $\tau$ that is introduced by the acquisition system. This TOF value can be defined as:

$$TOF_{\text{sr}} = \frac{d_{sr}}{c} + \tau \tag{4.1}$$

where:

$$d_{\text{sr}} = \sqrt{(x_s - x_r)^2 + (y_s - y_r)^2 + (z_s - z_r)^2} \tag{4.2}$$

The value for $\tau$ is considered to be constant across all traces as all data were acquired using a pair of identical P4-1 probes. For a given experimental watershot dataset, the TOF for each trace was measured to give the set $\mathbf{TOF_m}$. While there is the potential here to introduce a systematic error in $\mathbf{TOF_m}$ by incorrectly selecting the starting time of the matched filter, any constant error can be absorbed by $\tau$ when optimising for a constant delay across all traces. Several methods can be used to measure the TOF of a trace, including by using a wavelet based Akaike information criterion (AIC) travel time picker [Zhang et al., 2003], by applying a matched filtering and by taking the position of the

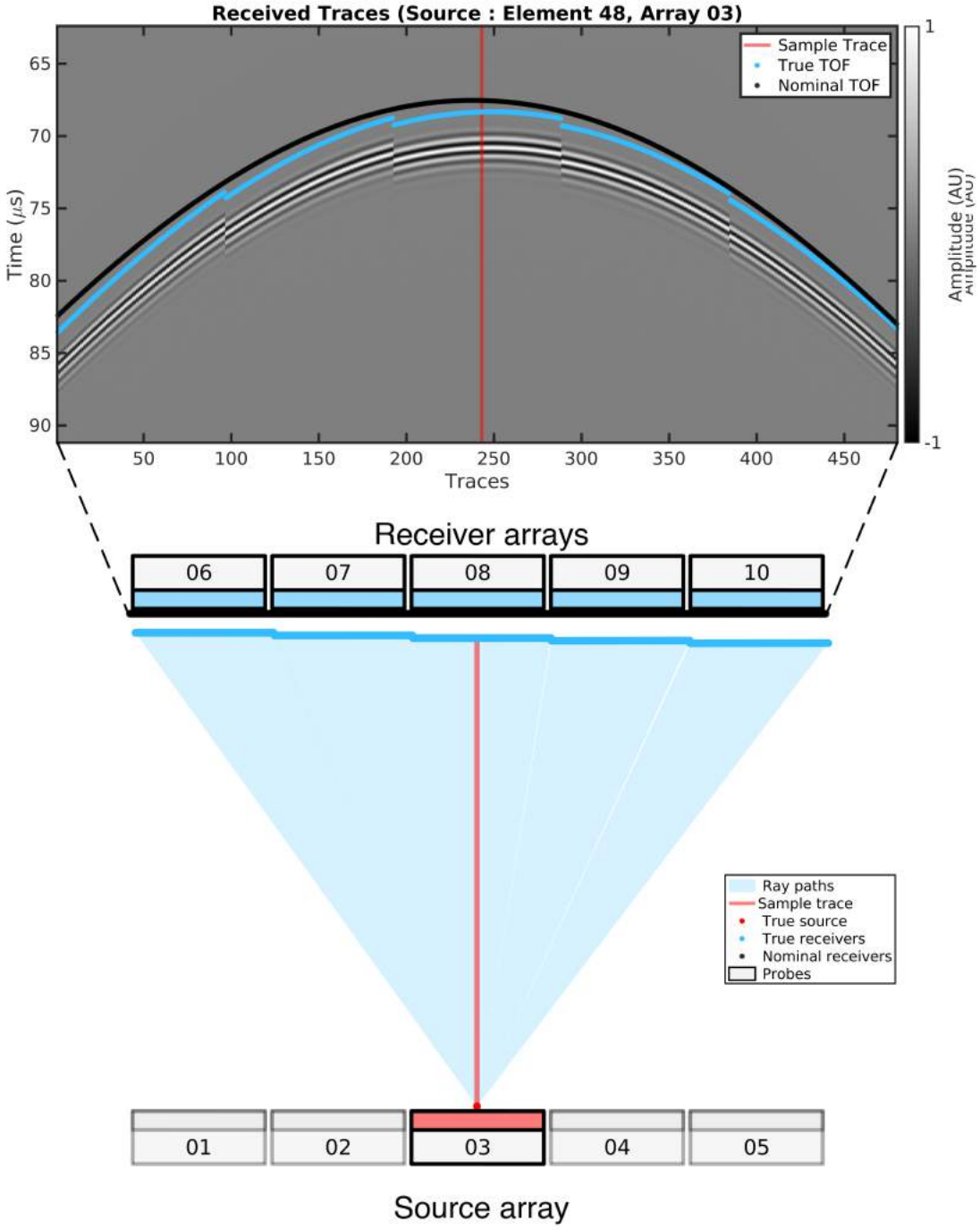


Figure 4.8: **Watershot USCT acquisition for a single element transmit event.**

maximum peak in the trace. AIC is an automatic method for detecting the first arrival of signal in traces by minimising the AIC, which corresponds to the point where signal can be distinguished from noise. Alternatively, given that we are searching for the arrival of a received wavelet seen across all traces, the TOF also be measured by searching for the position of this wavelet in each trace using

a matched filter. This matched filter is simply a sample of this wavelet taken from an ideal, directly transmitted trace (as seen by the sample trace plotted in Figure 5.8a). By cross-correlating each trace with this matched filter, the TOF is taken as the position of the resulting maximum peaks, which corresponds to the positions of greatest agreement between the matched filter and the wavelet contained in the traces. Finally, the simplest method for measuring travel time is to take the position of the maximum peak in each trace. While this will not correspond to the actual time point the signal was detected, for large sets of traces this can be used to quickly provide valuable information on the relative difference between arrival times across different traces.

Examples of the AIC, match filter and maximum peak TOF picking methods applied to a typical watershot trace can be seen in Figure 4.9. To compare each TOF method, we could consider the TOF picking error for each trace of a dataset, which is given by the difference between a measured TOF value and the true TOF value. However, as each method assigns the TOF position to a different part of the signal, the relative TOF picking error was considered instead. This was found by removing the mean offset between mean of the measured TOF error values for each method. This then allows for the performance of each method to be compared despite the different systematic errors of each method. An example of these realtive TOF picking errors can be seen plotted in and across a set of traces sampled from watershot USCT data in Figure 4.10. At first glance, this shows that the matched filter and max peak TOF both seem to remain within 0.02 $\mu$s of the true TOF values and both seem to give comparable results. Of the three methods the AIC TOF picking method seemed to show the greatest realtive TOF picking error. This is taken one step further in Figure 4.11 where the relative error was found and plotted across a full 115200 trace USCT dataset. Once again, the max peak and matched filter methods gave similar results while the AIC TOF method appears to show greater TOF picking error. Furthermore, the the AIC TOF picking method was the only method of the three that gave a set of outlier TOF values (a subset of 7885 measured TOF values), as seen

by the data points plotted in Figure 4.11 with relative error values greater than 0.2 $\mu$s. These observations are supported by the box plot for each method given in Figure 4.11. The max peak TOF picking method gave the smallest range of error values and the median closest to zero (range = [-0.0373,0.0482], median = -0.0049). The second smallest range and median were observed when using the match filter TOF picking method (range = [-0.0453,0.0565], median = -0.0057). Finally the AIC TOF picker performed the worst of the three methods, even after disregarding the outliers (range = [-0.3048,0.0741], median = -0.0110). From these observations, the $\mathbf{TOF_m}$ set for each dataset was acquired using the max peak picking method. It is worth noting that this is a specific application of TOF pickers in which the max peak method is well suited. The signal has high SNR and contains only one wavelet from measuring a single spherical transmission of a point source. Likewise, the element calibration method used favours methods which determines the most accurate a realtive difference of TOF between traces rather than the best method for detecting a value closest to the true TOF of each trace. This is because the element calibration relies on the $\mathbf{TOF_m}$ to provide information about the distance between sets of transducers. If the relative error between travel times is reliable and each TOF measurement shares the same constant systematic TOF error, this can be absorbed by $\tau$ during the element localisation. However, in other applications simply taking the max peak of a trace would not necessarily be the most reliable method for determineng the travel time of a signal.

Prior to starting the localisation optimisation, the set of modelled transducer-element positions $\mathbf{p}$ was initialised to estimated starting positions and $\tau$ was set to zero. These parameters were used to calculate a set of computed TOF values $\mathbf{TOF_c}$ using Equation (4.1). Calibrating these transducer positions could then be defined as a non-linear least-squares problem where the goal is to find a set of element positions and $\tau$, such that the difference between $\mathbf{TOF_m}$ and $\mathbf{TOF_c}$ is minimised. This can be defined by the objective function:

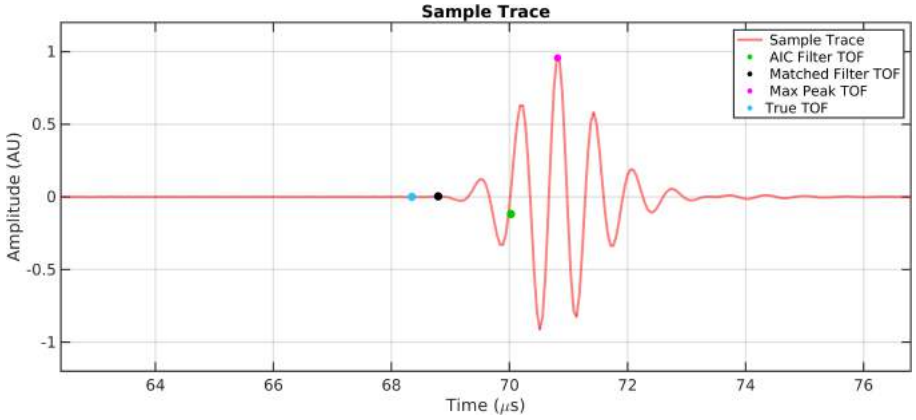


Figure 4.9: **A synthetic watershot trace with time-of-flight positions acquired using the AIC, matched filtering and maximum peak picking methods plotted alongside the true trace travel time**. This watershot trace was sampled from the example watershot acquisition given in Figure 4.8

$$minF_{\mathrm{p}}(\mathbf{p},\tau) = \left\{ \frac{1}{2} \|\mathbf{TOF_m} - \mathbf{TOF_c}\|^2 \right\} \tag{4.3}$$

by cross-correlating each trace with a matched filter and taking the position of the resulting maximum peaks. This matched filter was found by sampling the wavelet of an ideal, directly transmitted trace (as seen by the sample trace plotted in Figure 5.8a). where $F_{\mathrm{p}}$ is the residual between the measured and computed TOF sets. A Gauss-Newton algorithm was applied to minimise $F_{\mathrm{p}}$ iteratively until a sufficiently low error between these TOF vectors was achieved.

As each transducer element can be considered a point on the 2D imaging plane, the y-coordinate of each element can be set to zero. Therefore, for a localisation problem consisting of $\mathrm{P}_e$ transducer elements, there are a total of $2\mathrm{P_e} + 1$ unknowns to be solved for. When using the 3072 element ring array system discussed in Section 4.2, this gives 6,145 variables to be estimated. However, because these elements are translated as rigid transducer arrays (much like the transducer array system (TAS) discussed by Filipik *et al* [Filipík et al., 2012]), the number of unknowns can be significantly reduced by solving for the position and orientation of the probes instead of the elements. These transducer arrays can be modelled as having a position given by x,y,z-coordinates and an orientation given

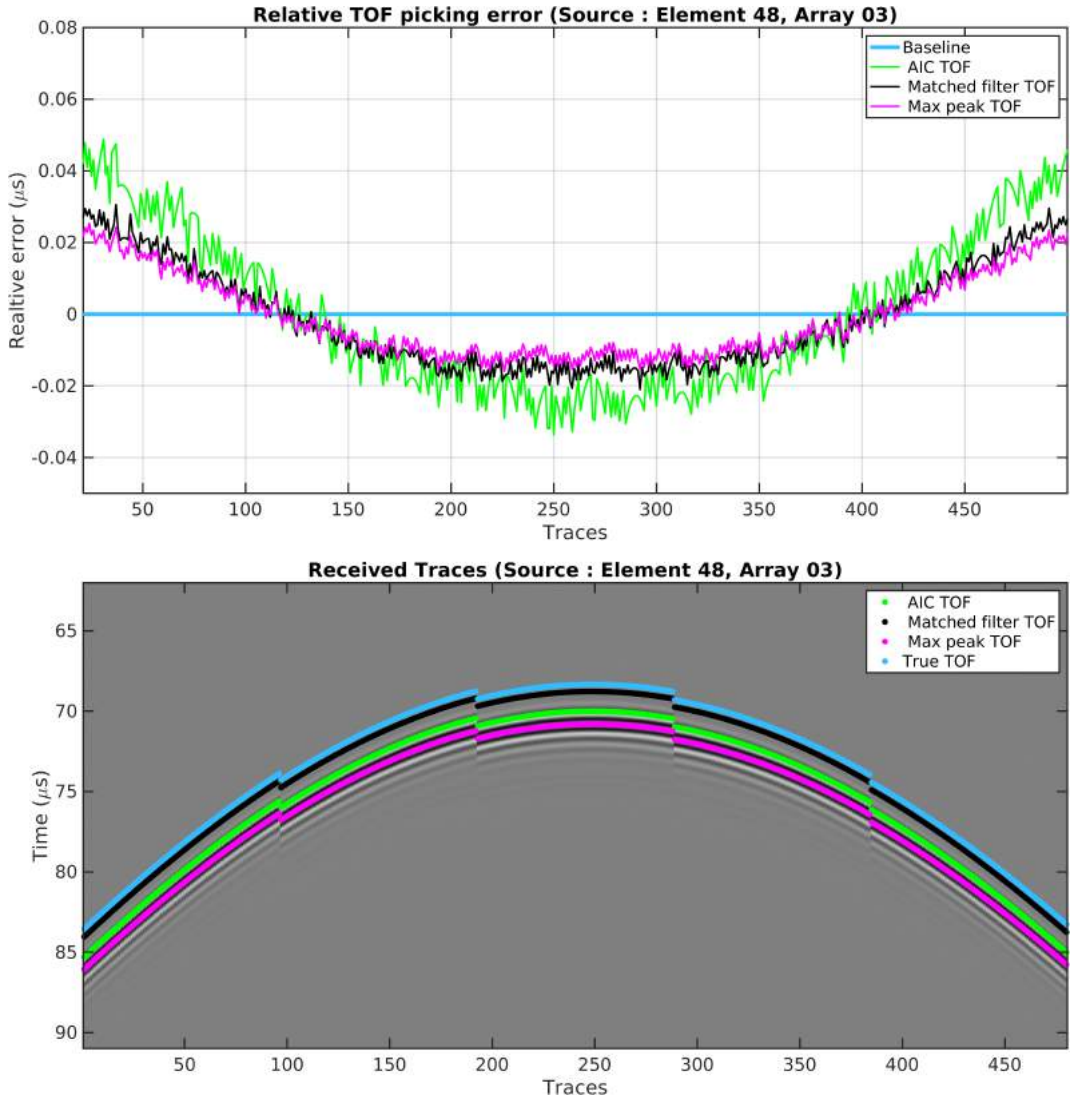


Figure 4.10: **TOF picking methods applied to a subset of watershot traces**

by the angles $\alpha, \beta, \gamma$ about the x,y,z-axes respectively. When modelling each array as a line of points (element pitch $= 2.95 \times 10^{-1}$ mm) lying on a 2D plane, however, the $\alpha, \gamma$ and the y-coordinate for each array can be set to zero. For a total of $\mathrm{P}_a$ probe positions, this gives $3\mathrm{P_a} + 1$ unknowns. When considering the 32 unknown probe positions in the ring array configuration (given that each probe will have its own unique set of 16 positions), this results in only 97 variables to be estimated. The objective function defined by Equation (4.3) remains unchanged when solving for these array positions instead of individual elements. As the goal of this optimisation method is to solve for relative positions and orientations between arrays, to anchor the solution to global coordinates the first array is

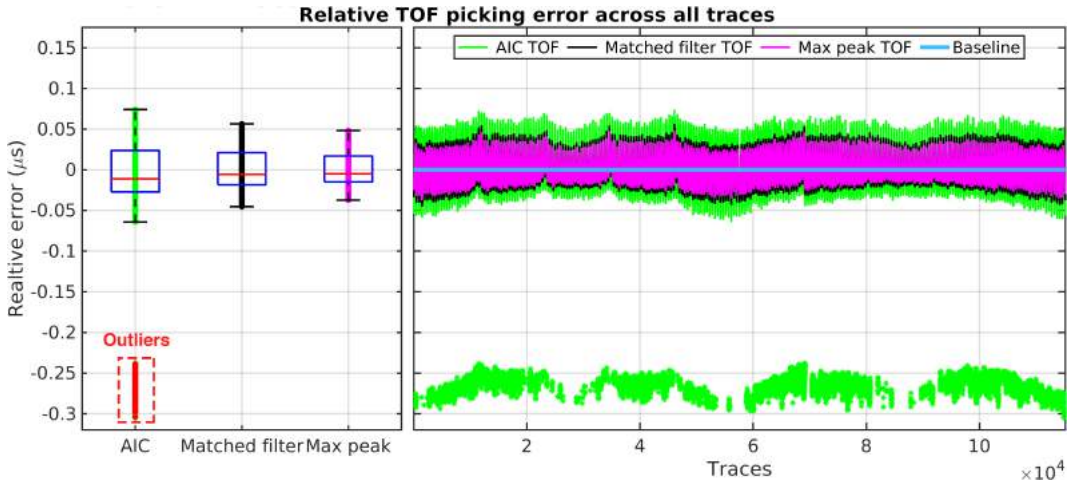


Figure 4.11: **Relative TOF picking error of the AIC, matched filter and max peak TOF picking methods**. Each method applied to 115200 of a complete USCT dataset. On the left is a box plot showing the distribution of relative errors across the set of values for each method.

fixed to the origin with a $\beta$ rotation set to zero.

### 4.5.2 Source Wavelet Calibration

To find source wavelets to be used as inputs for our 2D FWI algorithm we first assume that the received signals for each source seen in the watershot data can be considered the transmitted source wavelets shifted in time by an offset given by $\mathbf{TOF_m}$. For a set of received signals acquired for a given source, an estimate for the wavelet of that source can be extracted by applying the normal move out (NMO) correction method [Zhou, 2014]. Using this method the trace offsets are removed from all traces and the received wavelets are coherently aligned as a stack at $t = 0$. An initial guess for the wavelet for that source can then be found by taking the mean of this stack of corrected traces.

To ensure that the source wavelets used for running FWI are able to reproduce the true transmission of the sources, we first test our initial set of estimated source wavelets by passing them as inputs to our 2D forward model to generate a

corresponding synthetic watershot dataset. Using this synthetic watershot data, a Wiener filter [Vaseghi, 2008] could then be computed to match the resulting synthetic wavelets to the extract real wavelets seen in the observed watershot data. This allows for a corrected set of source wavelets estimates to be generated that accounts for any discrepancies seen between the 2D synthetic and observed watershot data. As these corrected source wavelets estimates are then sufficiently calibrated to produce synthetic watershot data that closely matches what was observed experimentally they can then be used to as inputs for imaging applications using our 2D FWI algorithm.

### 4.5.3 Evaluating Full-Waveform Inversion Parameters

In the case where FWI is run using the true water velocity, transducer positions and source wavelets, we would expect a reconstruction from watershot data to converge to a velocity model populated with values close to the true water velocity. This is due because the synthetic traces should already match well with the the observed traces. Therefore, to assess whether our calibrated array positions and source wavelets are sufficiently accurate for solving imaging problems our calibrated set of FWI parameters were tested by attempting to recover a water velocity model from the observed watershot data (for this example the rotary configuration was used). To show the impact of the calibration methods, FWI was run with the following inputs: **(a)** while using the calibrated water source wavelets and the uncalibrated nominal transducer array positions, **(b)** while using the initial source wavelets estimates and the calibrated transducer array positions **(c)** while using both the calibrated source wavelets and transducer array positions. These FWI runs were performed with a maximum frequency of 0.5 MHz while using a homogeneous water starting model set to 1481.40 m/s, the measured water velocity for this experiment. In each case the $15^{th}$ iteration was taken for comparison, as shown in Figure 4.12.

When comparing the nominal and calibrated transducer array positions, as

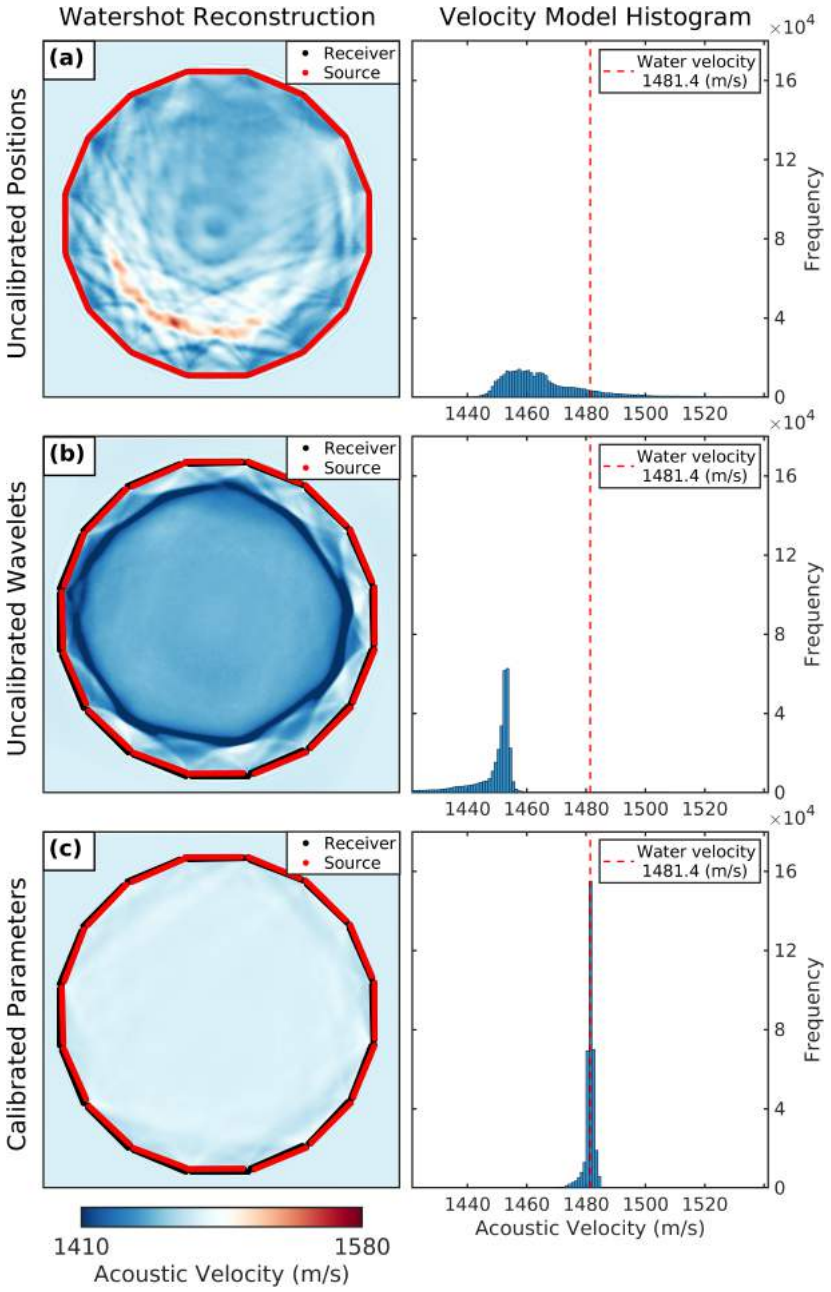


Figure 4.12: **Full-waveform watershot reconstructions to assess calibrated positioning and source wavelet parameters**. Reconstructions and corresponding histograms of recovered water velocity values are given for (a) Nominal, uncalibrated transducer positions and calibrated source wavelets. (b) Calibrated transducer positions and uncalibrated source wavelets. (c) Calibrated transducer positions and source wavelets.

shown plotted in Figures 4.12a and 4.12c respectively, the ring arrays appear to match closely. Despite this, the small differences between these sets of positions is enough to produce significantly different reconstructions, with strong artefacts appearing in the result for uncalibrated positions that were not present in the

calibrated case. As seen in the histogram of recovered velocity values for case **(a)**, the population of recovered velocities can be seen to be highly heterogeneous with a mean velocity of $1466.20 \pm 15.48$ m/s, a value significantly lower than the measured water velocity for this experiment. Likewise, in the result for case **(b)** for when uncalibrated source wavelets are used, as shown in Figure 4.12b, we can also see a population of recovered water velocities based around a value significantly lower than the measured water velocity, this time for a mean velocity of $1445.14 \pm 15.07$ m/s. In both of cases these lower values are introduced because of phase differences between the real observed watershot traces and the synthetic traces. These are caused by the errors in the relative distances between elements or by having a poorly matched source wavelets. These artefacts are created are then produced as the FWI sequence attempts to correct these phase differences by changing values in the velocity model.

Contrary to these results, the FWI watershot reconstruction for case **(c)**, when both calibrated transducer array positions and source wavelets were used, was found to have a mean water velocity of $1481.28 \pm 1.54$ m/s that matched closely with the measured water velocity. Furthermore, the population of recovered velocity values was found to have little variance, as seen in the histogram of Figure 4.12c, supporting the observation that the recovered velocity model was mostly homogeneous. This can be attributed to the minimal mismatch between observed and synthetic traces once these when using these calibrated FWI parameters. From this result we would we then consider these FWI parameters to suitable for solving imaging data using data acquired by the dual probe USCT system.

# Chapter 5

# Full-Waveform Inversion Brain Phantom Feasibility Study

## 5.1 Introduction

The accessibility, portability, inherent safety and low cost of ultrasound imaging devices has made medical ultrasound one of the most widely used non-invasive imaging modalities. For these reasons, transcranial sonography has become an indispensable imaging modality for the routine care of newborns. Despite these benefits, high-resolution ultrasound imaging can not be performed to image adult human brains using this approach. This is due to the severe degradation of high frequency ultrasound signals used in conventional transcranial sonography (5-12 MHz) when developed skulls are present (this is typically observed in patients older than 6 months) [Gupta et al., 2016]. Some structural imaging of the brain has be demonstrated by using low frequency ultrasound (below 1.00 MHz) and conventional ultrasound imaging techniques, such as pulse echo B-mode [Smith et al., 1978]. Unfortunately, sonifying at these lower frequencies comes at the expense of spatial resolution. Furthermore, the presence of skull tissue can result in the distortion and scattering of ultrasonic waves [**?**]. This prevents high resolution, diagnostically useful images of the brain from being acquired when imaging

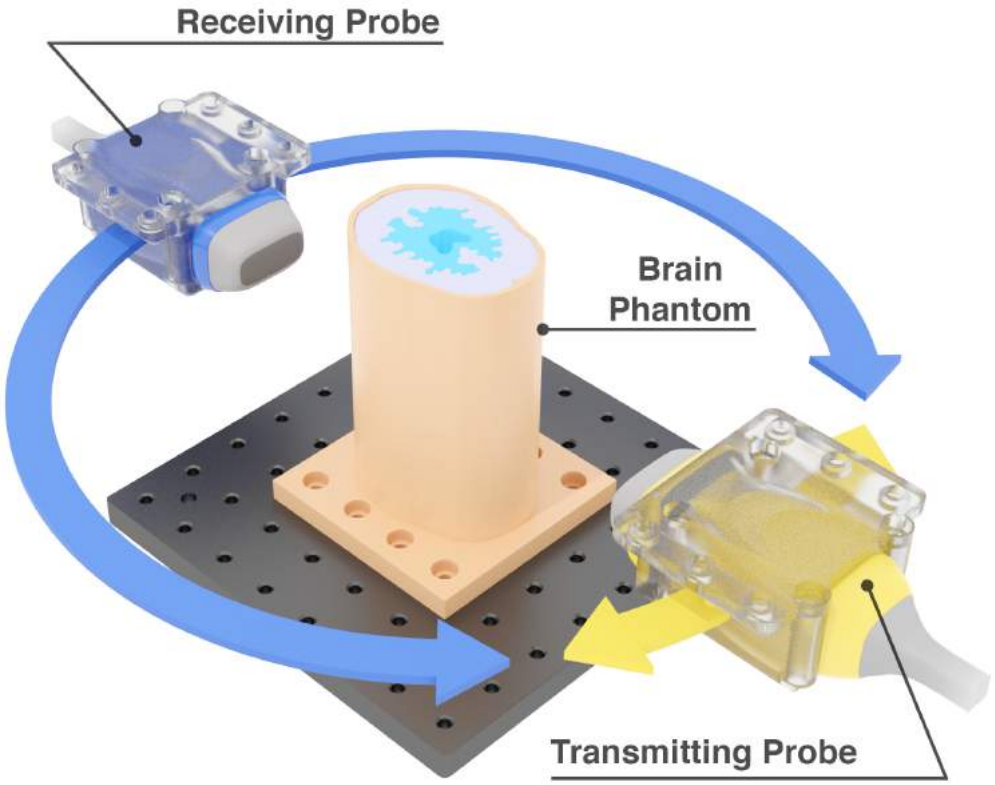


Figure 5.1: **Dual probe ultrasound tomography experimental setup**. A pair of medical probes are translated independently about a 2.5D brain and skull mimicking phantom to acquire transcranial ultrasound tomography data

at these lower frequencies. However, imaging the brain through thin sections of skull at these lower frequencies has been shown to be useful for measuring blood flow in major intracranial arteries [Naqvi et al., 2013].

In this chapter, I demonstrate *in vitro* for the first time the feasibility of applying FWI to reconstruct a brain-tissue phantom surrounded by a skull-mimicking layer. To achieve this, we designed a novel ultrasound computed tomography (USCT) acquisition system using a pair of translated off-the-shelf clinical cardiac probes (P4-1, ATL, USA) to image both reflections and transmissions. While it has been shown that 3D FWI is required for imaging complex geometries such as the head due to out-of-plane effects [Calderon Agudo et al., 2018]. However, a 3D FWI imaging problem would require a USCT acquisition that encompasses an

imaging target in 3D (using either a cylindrical, spherical or hemispherical array of ultrasound transducers), which would be time consuming to acquire using conventional ultrasound probes compared to a 2D scan. Furthermore, significantly higher computational costs and run times are required to run 3D FWI compared to 2D FWI. We therefore chose to constrain the dimensionality of the problem to 2D for this feasibility study. This was to minimise the run time when completing USCT acquisitions and to run FWI as many different transducer configurations and FWI parameters were investigated. For this reason, the dimensionality of the imaging models considered in this study were constrained to 2D images. This was done to simplify the acquisition of USCT data and to reduce computational costs when running FWI. Therefore, we designed a brain and skull mimicking phantom that consisted of a 2D brain and skull image extended along the vertical axis to provide a 2.5D imaging phantom. A render of this phantom can be seen in Figure 5.4c. This phantom was designed to provide an imaging target that mimics the skull and brain tissue we would expect to encounter when imaging patients in a clinical setting.

## 5.2 Methods

### 5.2.1 2.5D Brain Mimicking Phantom

A cross-section of the realistic numerical MIDA head model [Iacono et al., 2015] was used to design a 2.5D brain and skull phantom. The skull 3D printed resin skull layer (acoustic velocity $\simeq$ 2500 m/s) and polyvinyl alcohol (PVA) cryo-gel brain tissue mimicking material (acoustic velocities ranging from 1500-1520 m/s). As seen in the 2D numerical brain and skull model of this phantom in the Figure 5.2a, the brain model was given a simplified, easy to fabricate design consisting of an outer white matter layer ($\sim$1500 m/s), an inner grey matter layer ($\sim$1520 m/s) and a large water filled cavity to form three distinct regions of contrasting acoustic velocities.

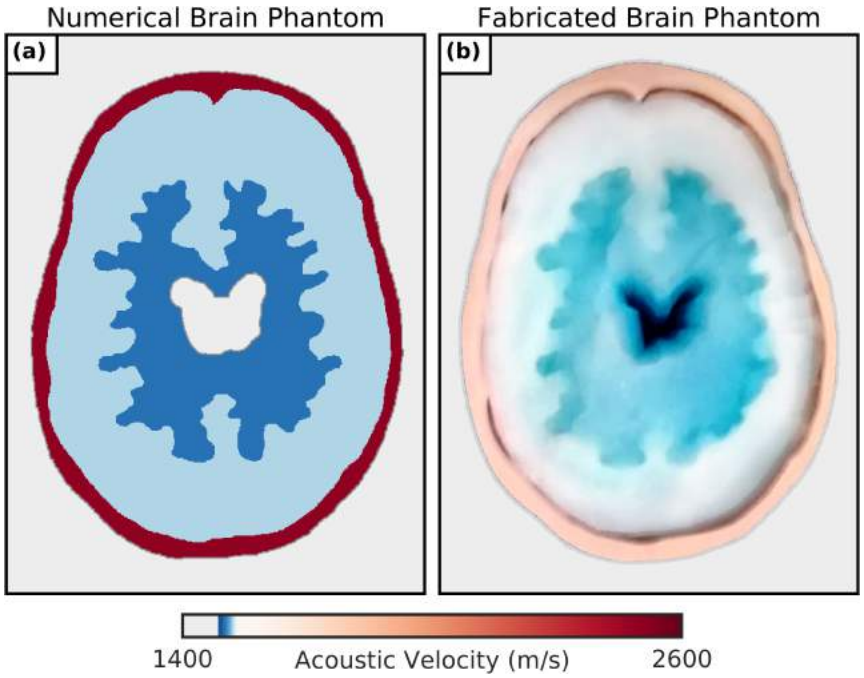


Figure 5.2: **Axial view of the numerical and fabricated 2.5D Brain Phantom**: (a) The numerical brain phantom consisting of a skull, a simplified brain structure and water filled cavity. (b) A photo of the final fabricated brain phantom with a 3D printed resin skull and a a PVA cyrogel tissue mimmiciking material.

Acquiring USCT data with sufficiently low frequency can be used to mitigate cycle-skipping. This is a well documented phenomenon in geophysical FWI applications that occurs when the predicted and observed wavefield data are found to be more than 90° out-of-phase [Bunks et al., 1995]. This can be seen demonstrated in Figure 5.3 which shows the inversion solution for two starting models from the same imaging problem while starting at different frequency bands. The starting model wavefield results given in Figure 5.3a represents the broadband case where the USCT dataset has sufficiently low frequency content for the starting wavefield dataset to be within the half wave cycle. Model updates from the inversion solution would then tend towards the global minimum, as shown in Figure 5.3c. However, when starting in a higher frequency band as seen in Figure 5.3b, the lag is now greater than the half wave cycle. Consequently, the inversion solution still moves to minimise the observed and synthetic data

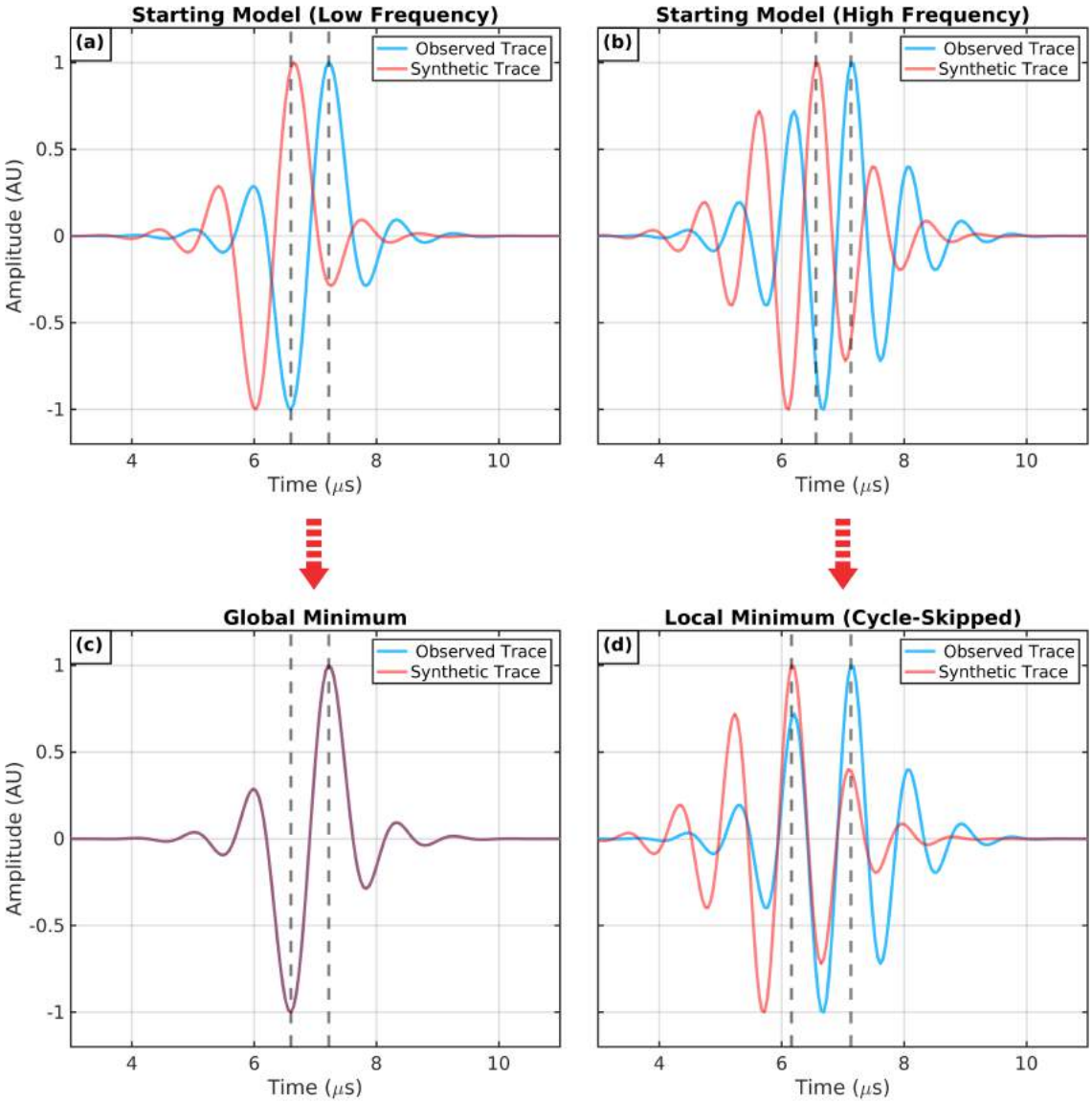


Figure 5.3: **Demonstration of cycle-skipping when running full-waveform inversion**. (a) Starting wavefield data and observed data when starting from a lower frequency band such that the lag is less than the half cycle. (b) Starting wavefield data and observed data when starting from a higher frequency band such that the lag is greater than the half cycle. (c) As the lag was less than the half cycle the inversion solution tended towards the global minimum. (d) As the lag was greater than the half cycle the inversion solution tended towards local minima.

but while converging to a local minima instead. In this case cycle-skipping has occurred, resulting in reconstructions with erroneous information. In the *in silico* FWI brain imaging study discussed by Guasch *et al* [Guasch et al., 2020], USCT with a bandwidth of 0.10-0.85 MHz was selected to mitigate the effects of cycle-skipping due to the traveling time differences observed in received

signals when imaging through high speed of sound (SoS) skull tissue. However, medical ultrasound probes are typically not designed to image at sub-megahertz frequencies, making them poorly suited for acquiring data in this frequency range. In this study we have selected a pair of cardiac probes (P4-1, ATL, WA, US), with a frequency range of 0.50-3.50 MHz measured at $-40$ dB, making them among the lowest frequency medical transducers currently available. To account for the difference in bandwidth between these cardiac probes and the ideal bandwidth found for FWI brain imaging in silico, the brain phantom was proportionally reduced to a 2:5 scale relative to the original MIDA model. This gave a skull model with a width of 60.54 mm, a length of 78.87 mm, a height of 130.00 mm and a mean thickness of $2.24 \pm 0.48$ mm, which can be seen in Figure 5.4d.

To create the PVA cryogel brain tissue mimicking material a similar approach was taken to the tissue fabrication protocol proposed by Chee *et al* [Chee et al., 2016]. Here the brain tissue was prepared using a 10% PVA powder (341584; Sigma-Aldrich, St. Louis, MO, USA), 90% distill water solution heated at 90°C with a magnetic stirrer for 1 hour while covered with clingfilm to reduce water loss by evaporation.The solution was then left to cool to 40°C where it can be handled while still being in a liquid state for pouring. The PVA cyrogel was formed over several 24 hour freezing-thawing cycles (12 hours stored in a freezer at -20°C followed by 12 hours left at room temperature): increasing the number of these cycles increases the amount of polymerisation of the PVA, resulting in higher acoustic velocities as the density of the material increases. By selecting for these freeze-thaw cycles the two brain layers could be set with contrasting acoustic velocities.

To ensure that the complex, irregular structures seen in Figure 5.2a remain consistent along the length of the 2.5D phantom, a pair of 3D printed resin moulds were created: **(1)** an inner mould to form the irregular boundary between the two brain layers, as shown in Figure 5.4a, and **(2)** a cavity mould to shape the inner brain layer and water cavity boundary, as shown in Figure 5.4c. To create these

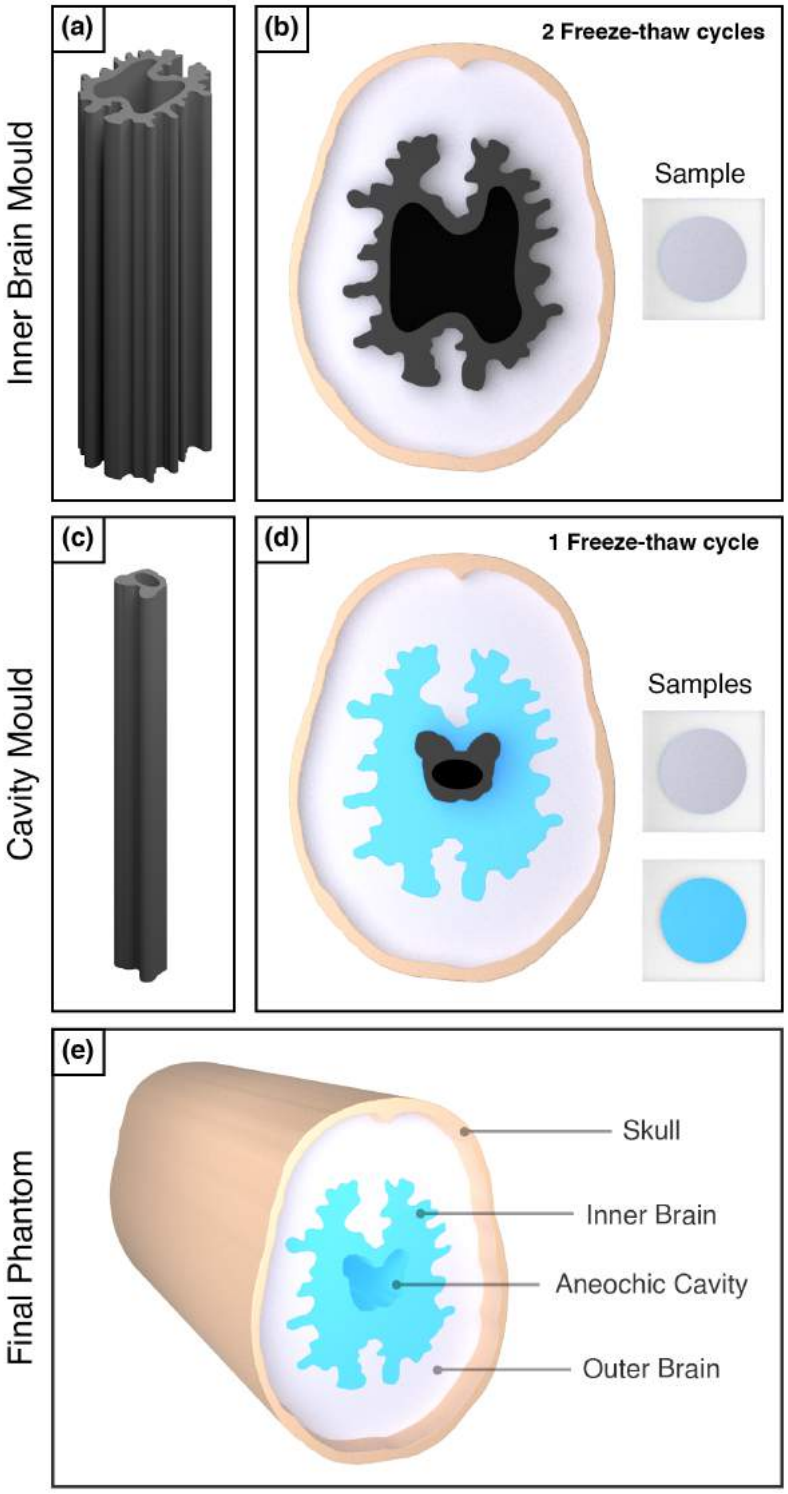


Figure 5.4: **2.5D brain and skull phantom fabrication**: (a) A 3D printed resin mould providing the irregular boundary between the inner and outer brain layers. (b) The 2.5 phantom and outer brain tissue mimic sample during the first cryogel conditioning step. (c) A 3D printed resin mould providing the boundary of the central cavity of the brain model. (d) The 2.5 phantom and brain tissue mimic samples during the second cryogel conditioning step. (e) The final skull and brain 2.5D phantom

brain layers, the PVA solution was first poured into the space created between the inside of the skull wall and the outer surface of the inner brain mould place before the phantom was left to undergo 2 freeze-thaw cycles, as shown in Figure 5.4b. Once completed, the inner mould was removed, leaving only the outer brain layer within the phantom. To create the inner brain layer the cavity mould was inserted and new batch of PVA solution was poured into the remaining space (in this new PVA batch a single drop of food colouring was added to provide a visual indicator of the contrasting brain layers). The phantom was then left for 1 additional freeze-thaw cycle, as shown in Figure 5.4d. In this procedure the outer layer therefore underwent a total of 3 cycles while the inner layer only underwent a single cycle. Samples from each PVA pour stages were used to create cylindrical testing samples of their corresponding PVA cryogel brain layers, both of which underwent the same freeze-thaw treatment as their respective tissue mimics. The velocities of these samples could then be measured to provide velocity values for these brain layers, as seen in Table 5.1.

The final brain model within the resin skull can be seen in Figure 5.2b. The end result closely matches the original numerical brain and skull model, however small differences can be seen in the brain model due to the expansion of the PVA tissue mimic during the freeze-thaw cycles, which is most noticeable when observing the reduced size of the central water cavity feature.

Table 5.1: Acoustic velocities of features seen when imaging the acoustic brain and skull phantom.

| **Phantom Layer** | **Acoustic speed, $\mathbf{c}_\mathrm{o}$** (m/s) |
|---|---|
| Resin Skull | 2550 |
| Outer Brain Layer | 1520 |
| Inner Brain Layer | 1500 |
| Water | 1480 |

### 5.2.2 Data Acquisition

USCT data was acquired using an ultrafast ultrasound research acquisition system with two 128 channel ports (256 Verasonics Vantage system, USA, WA), allowing for two P4-1 cardiac probes to be connected at once (96 element phased array, ATL, USA, WA). Once connected the two probes can be considered a single system which can simultaneously transmit and receive ultrasound signal. All imaging was performed in the centre of a large 1 $m^3$ water tank to prevent strong reflections from the water surface and the sides of the tank from being detected.

As we are running FWI in 2D for this study, we define our imaging regions as lying on the x-z plane, this means all space-dependent fields are considered invariant with respect to y, and any point source in this x-z plane can thought of as an infinitely long cylindrical source orthogonal to the plane [Igel, 2017]. The height of these transducer elements were found to be much greater in height than in length (width = 2.45 x $10^{-}1$ mm, height $\approx$ 13.00 mm), so we can consider these elements as infinitely long sources relative to the 2D imaging plane (assuming both probes are positioned so they are facing, co-planar and their elements are aligned with the vertical y-axis). Furthermore, as the width of the P4-1 elements are less than the smallest wavelength considered when running FWI (while imaging up to a maximum frequency of 1.6 MHz), these elements can be considered as point sources and receivers within this imaging plane.

Once in position, the ultrafast ultrasound imaging system allows for the fast acquisition of USCT data for all selected source and receiving elements. However, given that the aperture of a P4-1 probe is only 28.32 mm in length, the imaging region that can be sonified by stationary probes is limited. We therefore decided to translate the dual probes to effectively extend our ultrasound apertures, allowing for larger objects to be imaged. We investigated two different configurations to achieve this: **(1)** Linear array translations, where each probe is translated in 1D to create two facing sets of transducer array positions to increase the imaging

region, **(2)** Rotary array rotations, where both probes are rotated about a ring of array to surround the imaging target.

### Linear Array Configuration

We first considered the simple method for extending the imaging range of the dual probe system by applying 1D linear translations using the plane array configuration discussed in Section 4.2. Using the linear motors of the dual probe acquisition five transducer array positions were set either side of the 2.5D phantom over motor steps equal to the length of a P4-1 aperture. This created two parallel 480 element, 141.60 mm long transducer arrays either side of the imaging target, as illustrated in Figure 5.5a. A USCT acquisition sequence was applied to translate and acquire data over all unique 25 source-receiver array positions. All 96 elements of each array position were set as receivers while a subset of equally spaced 24 elements were selected as sources, providing a total of 240 sources and 960 receivers. Using this configuration, USCT data can be acquired in transmission by all receiving elements of the opposing transducer array positions while reflected signal could only by acquired using elements of the transmitting array (as shown by elements highlighted in blue either side of the source in Figure 5.5a).

### Ring Array Configuration

To provide a full 360$^{o}$ Deg scan of the 2.5D phantom, the rotary array configuration described in Section 4.2 was used to define a ring array of 16 rotated probe positions with a step size of 22.5$^{o}$ Deg. USCT data was acquired using this setup by transmitting with one probe set over these 16 array positions while the second probe was rotated about all possible receiving array positions in the ring for all transmissions. To achieve this the receiving probe was rotated about the imaging region using a large aperture rotary table (Standa, Lithuania), while the source probe was connected to smaller, centrally positioned rotary motor (PRMTZ8/M,

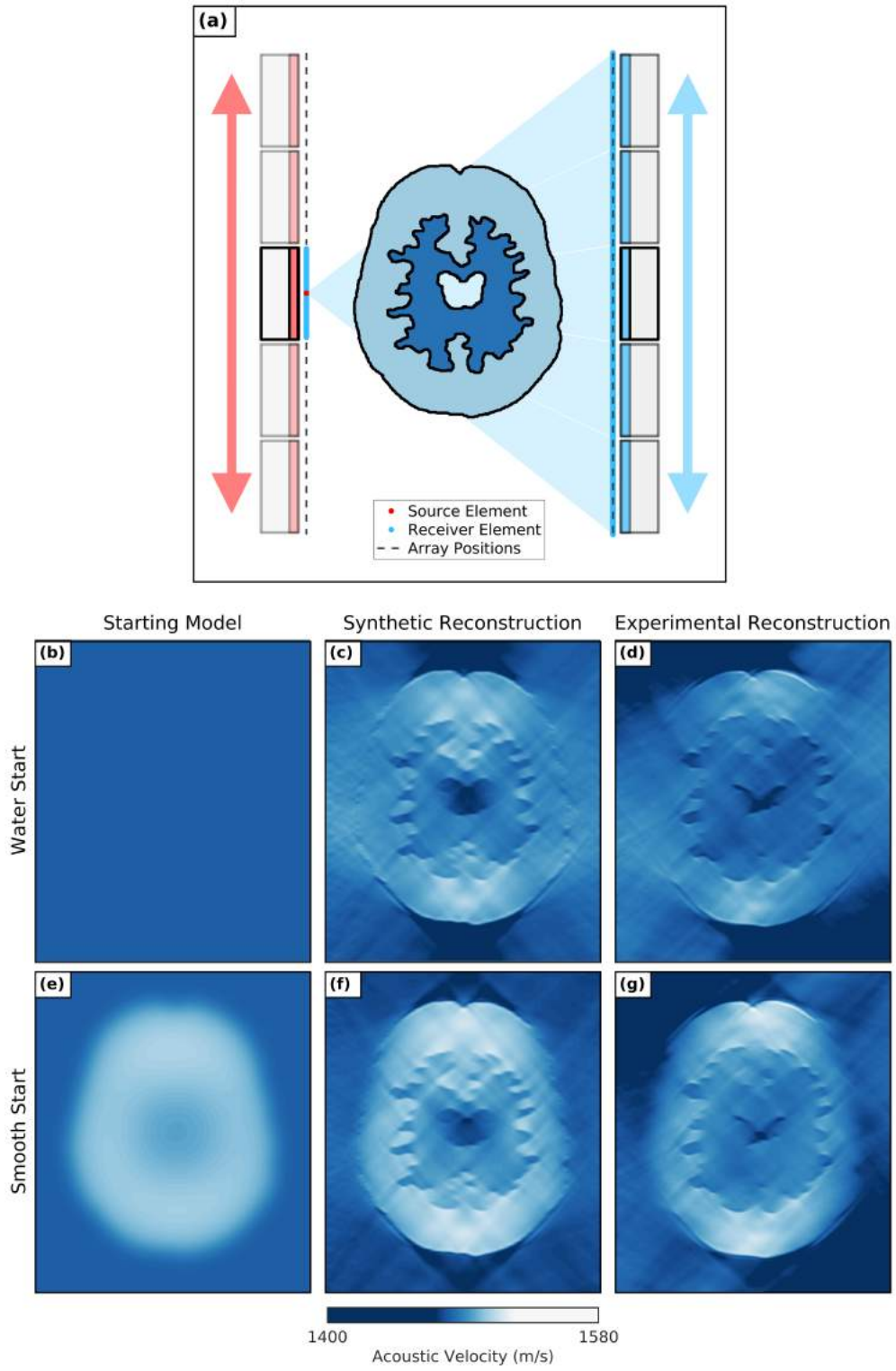


Figure 5.5: **Linear array full-waveform inversion results of the brain phantom**. (c)(d) Synthetic and experimental full-waveform reconstructions of the brain model for water starting model (b). (f)(g) Synthetic and experimental full-waveform reconstructions of the brain model for smooth brain starting model (e).

Thorlabs, Inc., USA, NJ). The size of the imaging region could then be adjusted by changing the radius of the ring array created when rotating these probes. For imaging the 2.5D phantom a radius of 75.00 was chosen. An example for the opposing receiving positions selected for a given source can be seen in Figure 5.7a. To avoid collisions a buffer regions of 2 array positions either side of the source array are not included in this set of receiving positions to prevent the probes from colliding, meaning each source array transmits to 11 receiving arrays (given a ring array of N positions, roughly 68% can be used as sources). However, by setting the source array to receive as well as transmit this setup still allows for good coverage of reflected signal data to be received (this can also indicated in Figure 5.7a by the blue receiving positions along the aperture of the source array).

### Phantom Positioning

For each configuration three USCT scans were performed: **(1)** imaging the 2.5D pahntom without the skull, **(2)** imaging the 2.5D phantom with the skull and **(3)** imaging when there is only water to provide a watershot dataset. Dataset **(1)** was acquired to first assess the performance of each configuration when applied to a soft tissue mimic imaging problem before attempting the more challenging inversion using dataset **(2)** due to the introduction of relatively high velocity material. Dataset **(2)** provides the watershot data that will be used to calibrated the dual USCT imaging system, as described in Section 4.5.1

As shown in Figure 5.8, by using the linear motors these three acquisitions could be performed by simply adjusting the vertical position of the 2.5D phantom and placing the brain model to be either fully or partially inserted into the skull casing. This approach was used to minimise the need to manually performed adjustments to the imaging rig during experiments where possible to avoid any possible misalignment between the transducer positions while imaging their positions during the watershot acquisition.

(a) Brain imaging mode

(b) Brain with skull imaging mode

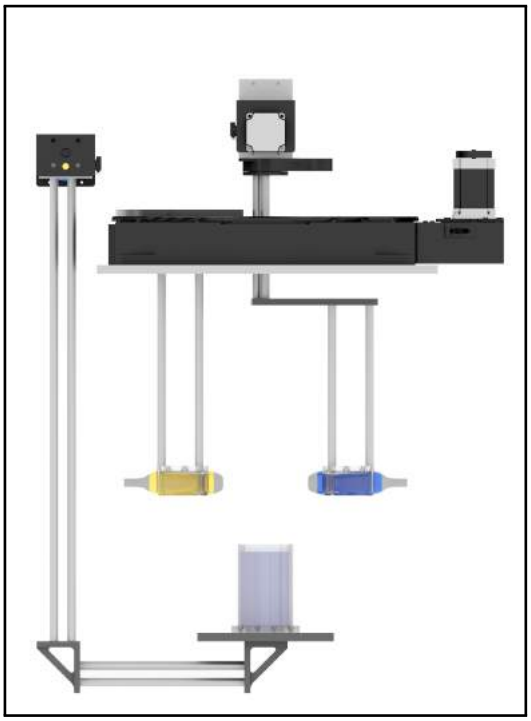

(c) Watershot mode

Figure 5.6: Phantom positioning modes
(a) Imaging the brain without the skull. (b) Imaging the brain with the skull. (c) Watershot acquisition.

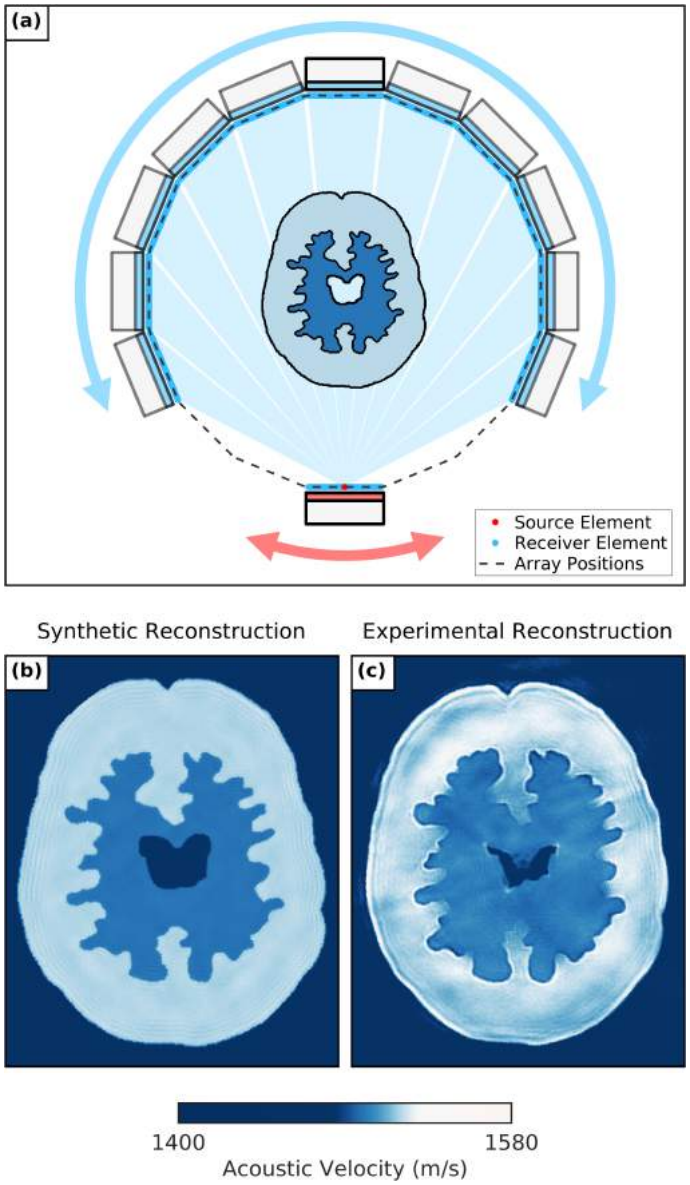


Figure 5.7: **Rotary array full waveform inversion results of the brain phantom**. (a) Dual probe rotary array configuration of 16 transducer array positions with the synthetic numerical brain model placed in a central position. (b) Full waveform inversion reconstruction of generated synthetic data for use as a reference. (c) Full waveform inversion reconstruction of data acquired experimentally

## 5.3 Results

In this section, results from the application of the FWI algorithm to recover velocity models using data acquired by linear and rotary dual probe acquisition configurations are presented, as discussed in section 5.2.2. As the true velocity and morphology of the fabricated 2.5D phantom are unknown, we would the

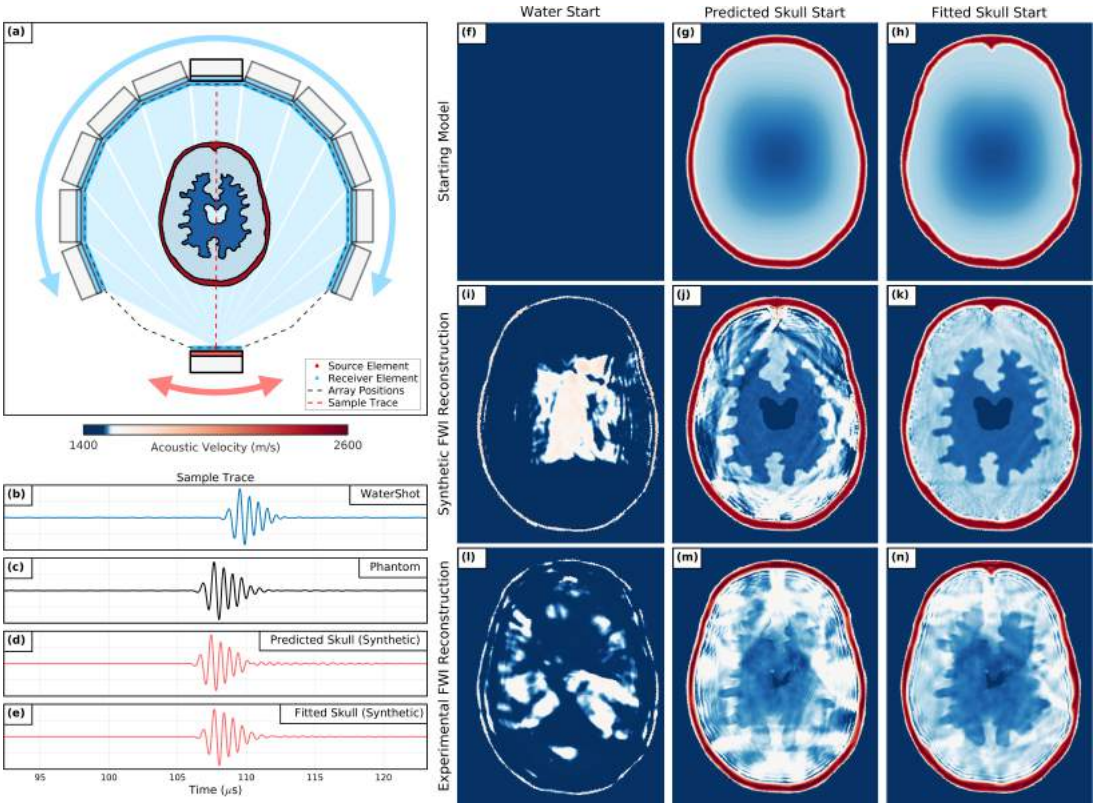


Figure 5.8: **Synthetic full-waveform inversion results when imaging the 2.5D phantom using the rotary array configuration**. (a) Experimental setup of the rotary acquisition showing the transducer positions for the shot gathers of the first source array; (b)-(e) Sample trace taken when transmitting through water, the 2.5D phantom, the predicted skull starting model and the fitted skull starting model; (f)-(h) Water, predicted skull and fitted skull starting models; (i)-(k) Full-waveform inversion reconstructions for the different starting models using synthetic USCT data; (j)-(n) Full-waveform inversion reconstructions for the different starting models using experimental USCT data.

expect the veloicty map of a 2D cross section of this phantom to be similar to the numerical brain phantom seen in Figure 5.2a. We therefore used this numerical phantom to create a corresponding synthetic reference model for each experiment while using injecting velocity values found experimentally for each of the different tissue mimicking layers. By then imaging this synthetic reference using the calibrated array positions and source wavelets an equivalent *in silico* dataset could be created for each experimental acquisition, allowing us to compare each experimental FWI reconstructions with a comparable, ideal synthetic FWI reconstruction for use as a reference.

### 5.3.1 Linear Array Brain Phantom Results

To test the feasibility of the dual probe linear array system described in Section 5.2.2, experimental USCT data was acquired by imaging the 2.5D phantom. As shown in Figure 5.5a, the phantom was placed in the centre of the imaging region formed by the two sets of transducer arrays. To provide a less challenging imaging problem to test this configuration, the phantom was scanned without the skull layer in place. Using the optimised FWI parameters found for this experiment and the brain model of the numerical phantom, a corresponding synthetic USCT dataset for this imaging problem was also generated.

As only a small difference in acoustic velocity was expected between water ($\sim$1484 $ms^{-1}$) and the highest velocity brain model layer ($\sim$1520 $ms^{-1}$), we first attempted to recover the brain phantom by FWI using a homogeneous water starting model, as seen in Figure 5.5b. A frequency stepping FWI sequence was applied starting from the lowest frequencies of signals seen when using P4-1 probes (0.55MHz to 1.05MHz, iterations = 114). The resulting reconstructions using synthetic and experimental USCT data both showed comparable partial recoveries of the phantom brain model, as shown in Figures 5.5c and 5.5d respectively. In both cases the irregular boundary between the brain layers were clearly visible, as were the central internal water cavities, while the top of the bottom surfaces of the phantom were recovered well with a strong contrast to the surrounding water. However, surfaces facing the two transducer apertures were not successfully recovered and, despite the numerical brain model consisting of homogeneous layers, the recovered values seen in the synthetic result are both lower than expected and heterogeneous within these layers (in both reconstructions recovered velocity values can be seen to be highest in the centre of the brain model and decrease when moving towards each transducer aperture). These results were most likely due to the limited distribution of receiving elements when receiving reflected signal from different locations in the imaging region created by this transducer configuration. This means more imaging data was acquired for centrally positioned features than those to the sides, forming blind spots. The root mean square (rms) error between

the synthetic reconstruction and the true synthetic numerical brain model was found to be 13.56 $ms^{-1}$.

We attempted to improve on these poor reconstructions by repeating the FWI sequence for both datasets while replacing the homogeneous water starting model with a smoothed brain starting model, as shown in Figure 5.5e, which was created by applying a 2D Gaussian filter to the numerical brain model. Despite providing little structural information, this starting model significantly improved the reconstruction of both the synthetic and experimental reconstructions, as can be seen in Figures 5.5f and 5.5g. In both cases the brain phantom can be easily distinguished form the surrounding water and the brain layers were found to contain higher velocities which are more consistent with values measured from samples. However, the same uneven distribution of velocities observed in the previous reconstructions can also be seen in these results. Likewise the sides of the phantom within the blind spots of this configuration change little from the smoothed edges of the starting model, supporting the previous observation that there seems to be insufficient information to successfully reconstruct features in these regions. This suggests this configuration is poorly suited for imaging the whole brain phantom. The rms error between this new synthetic reconstruction and the true synthetic numerical brain model was found to be 9.250 $ms^{-1}$, supporting the observation that a more accurate reconstruction was achieved by using this starting model. It's worth noting, however, that starting model made while already knowing the true synthetic model; for experimental applications this would need to be either predicted using prior information or found by used a less computationally demanding tomographic method, such as TOF tomography, which could introduce additional uncertainties and running costs.

### 5.3.2 Rotary array Brain Phantom Results

Like with the linear array case, we initially decided to assess the performance of the dual probe rotary array system, as described in Section 4.2, by first imaging

only the brain model layers of the 2.5D phantom with this configuration. As can be seen in Figure 5.7a, the brain model was placed in centre of the ring array which was formed by rotating both probes about the 16 transducer array positions. Once again the optimised transducer positions and transmitted wavelets from this experiment were used to image the numerical brain phantom to generate a corresponding reference synthetic dataset of this imaging problem.

Using this configuration we were able to recover high quality FWI reconstructions of the brain phantom for both the synthetic and experimental USCT datasets, as shown in Figures 5.7b and 5.7c respectively. Unlike in the linear array results, the increased number and distribution of receiving transducer positions for each source prevents any blind spots from forming in our imaging region of interest. As a result the full outer surface, inner brain layer boundary and central water cavity of the brain phantom can be seen clearly in both reconstructions. Furthermore, in the synthetic reconstruction the different velocity regions are shown to be homogeneous with closely matching values to the true velocity model for that problem. This can also be said for the experimental FWI result, albeit with greater variation in velocity values in the outer brain layer, however these differences likely reflect small variations in the acoustic velocity of the real PVA cryogel as the material set. The rms error between the synthetic FWI result and the true synthetic numerical brain model for this imaging problem was found to be 2.14 $ms^{-1}$, a significant improvement to the rms error seen in the linear array configuration results. As these reconstructions closely matched the expected velocity model of this brain phantom no follow up experiment using a smooth starting model was considered necessary.

### 5.3.3 Rotary Array Brain and Skull phantom results

After achieving promising results from the brain model withpout the skull, we then repeated the acquisition while including the 3D printed resin skull layer of the 2.5D phantom to provide a brain and skull imaging problem, as shown in

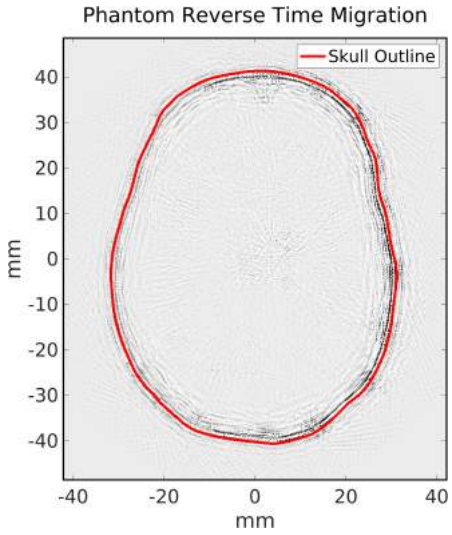


Figure 5.9: **Reverse time migration of the skull and brain phantom** was used to image the surface of the skull (as shown plotted here in red) to provide a prediction for its position relative to the dual probe imaging array.

Figure 5.8a. By introducing this high velocity skull layer (2500 $ms^{-1}$) a phase shift traces travelling through the phantom can be seen, as seen when comparing weastershot and phantom sample plots seen in Figures 5.8b and 5.8c. Here the the higher velocity material can be shown to reduce the travel time by 1.8480 $\mu$s. This time difference is sufficiently large that cycle skipping is likely when attempting to perform an inversion from a water start as there is insufficient low frequency content in the imaging data to mitigate this effect. This can be seen after attempting to reconstruct the 2.5D phantom from a water starting model when using both the synthetic and experimental USCT data, as shown in Figures 5.8i and 5.8l respectively.

However, while the 2.5D phantom was not successfully recovered in these inversions it's worth noting that the outer layer of the skull can be seen in both reconstructions. This is due to the strong reflections of the outer surface of the skull which can be used to provide useful information about position and morphology the skull. For this reason we applied reverse time migration (RTM) [Levin, 1984], a seismic imaging technique used to localise structures in the subsurface. This allowed us to provide a high resolution image of the surface of the 2.5D phantom using the USCT dataset, as shown in Figure 5.9, by tracing

the strong reflections of the skull layer from the RTM result. This provided us with prior information about the position of the 2.5D phanton and shape of the skull layer, allowing for starting models closer to the true case to be developed.

**Predicted Skull Starting Model**

Initially we attempted to design a starting model containing a predicted skull layer using the least amount of prior information possible. This included the position of the outer skull layer extracted from the RTM result, velocity estimates of the skull and smooth brain layers, which were given as 2500 and 1505 $ms^{-1}$ respectively, and a reasonable estimate for the mean skull thickness which we set as 2.00 mm (the true mean thickness was found to be 2.20 $\pm$ 0.26 mm). As shown in Figure 5.8g, this predicted skull was made the found outer layer of the skull inwards to create a skull with a constant thickness of 2 mm set to a velocity of 2500 $mms^{-1}$. The interior of the skull was then filled with a smooth brain model to account for the change in travel time due to the brain layers.

As shown in Figure 5.8d, the resulting sample trace through this starting model has a travel time that closely matches that of observed trace passing through the real phantiom shown plotted in Figure 5.8c. This suggests that this starting model can be used to reduce the initial mismatch between synthetic and observed data when running FWI to mitigate cycle skipping effects. This was confirmed to be true in both the synthetic and experimental FWI reconstructions of this imaging problem when using this starting model, as shown in Figures 5.8j and 5.8m respectively. In both results we can see the brain layers being reconstructed and the central water cavity in both reconstructions are clearly visible. However, without sufficiently low frequency signal content we can see only limited model updates to the predicted skulls themselves. To compensate for these skull layers from matching poorly with their true skull skull models, instead high velocity artefacts are can bee seen developing in the brain model layer, making it difficult to see fine features, such as the the irregular boundary between the outer and

inner brain layers. This would suggest that more closely matching skull starting models would be required for successful FWI reconstructions using this USCT dataset.

### Fitted Skull Starting Model

To improve on the FWI reconstruction results achieved whne using the predicted skull, a new starting model was designed by fitting the true synthetic skull seen in Figure 5.2a to the skull position providing by the RTM result. Like in the previous starting model, the interior of the skull is filled with a smooth brain model, as shown in Figure 5.8h. As the 3D printed resin skull was designed using this synthetic skull model, this skull model can be considered similar to the true skull layer being imaged in the experimentally acquired dataset. Once in position, the travel time seen in ou r sample trace for this starting model can again be seen to match closely to that seen in the sample trace through the real phantom found experimentally. FWI reconstructions from repeating the FWI sequence while using this starting model showed a significant improvement. The synthetic result can be seen to match closely to the true velocity model with a reduced rms error of 6.848 $ms^{-1}$ while the irregular structure can be seen to be recovered clearly in both synthetic and experimental reconstructions. When these sampling the recovered values from the experimental reconstruction, mean velocities 1478.45 $\pm$ 1.01 $ms^{-1}$, 1501.79 $\pm$ 1.01 $ms^{-1}$ and 1521.85 $\pm$ 4.29 $ms^{-1}$ were found for the water filled central cavity, inner brain layer and outer brain layer respectively. These match closely with the measured brain tissue mimic velocities and the water velocity measured for this experiment, suggesting this we have successfully reconstructed the inner brain model when imaging through our skull model. The outer brain layer does appear to be have some high velocity artefacts that are not seen in the synthetic reconstruction or in the experimental reconstruction of the brain model without the skull seen in Figure 5.7c. These are most likely a result of there still be some differences between this fitted skull model and the true skull.

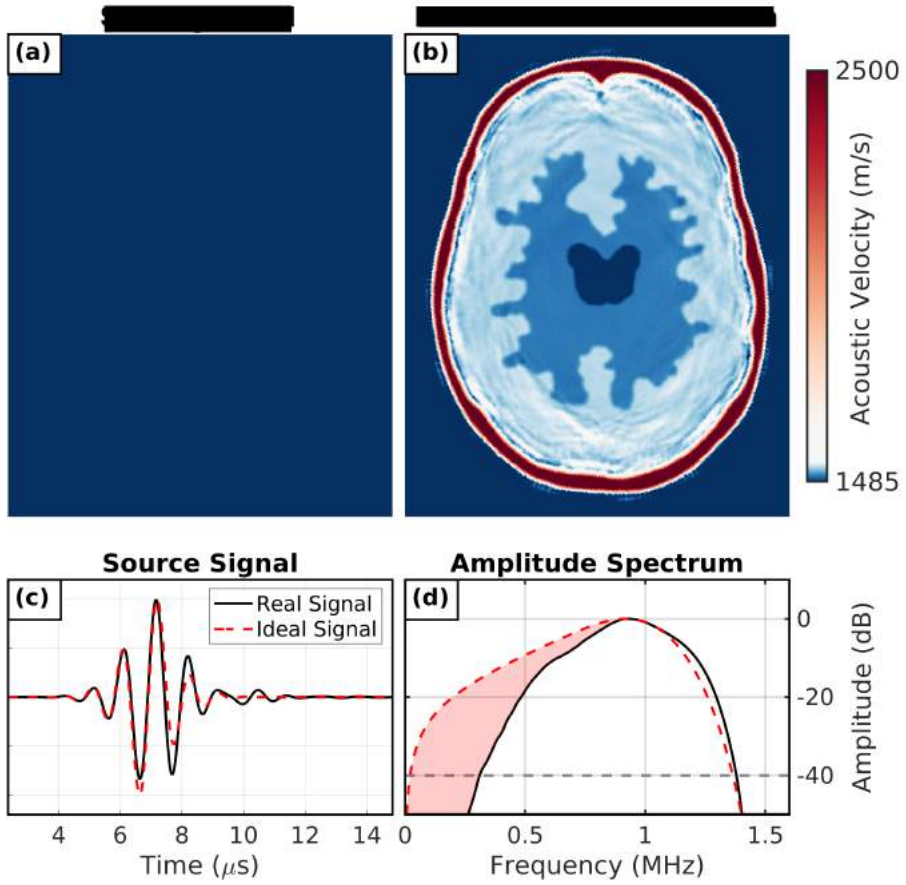


Figure 5.10: **An ideal synthetic full-waveform inversion reconstruction with broadband data** (a) Starting model of homogeneous water. (b) Ideal broadband full-waveform Reconstruction. (c) The real and ideal broadband source signals. (d) Amplitude spectrum of the real and ideal broadband source signal. Highlighted in red can be seen the low frequency content difference between these spectrums.

## 5.4 Discussion

Building on the *in silico* feasibility study for applying FWI to transcranial ultrasound imaging, in this work we take the first steps into translating what has been demonstrated through simulations into the real world and have shown that high resolution ultrasound imaging through dense, high velocity material such as the skull can be achieved when real data acquired experimentally. Furthermore, this was also achieved using a simple acquisition system comprised of low cost and readily available off-the-shelf equipment, suggesting that FWI could potentially have a significant impact as a medical imaging modality using existing hardware. This demonstrates the potential of using this methodology as a research tool

to explore the applications FWI in other fields with minimal investment; our experimental results for without the skull in place in particular demonstrate that this method would be well suited to imaging problems concerning soft tissue as in this application no prior information was required in order to achieve high quality, high resolution images. Due to the P4-1 probes used in this study having relatively limited lower frequency limit of ∼0.50 Mhz while having a relatively high upper frequency limit of ∼4.0 MHz, another potentially exciting direction for this research may be to apply this method on imaging targets on the smaller scale that are better suited to the bandwidth of these transducers. This could include high resolution neuroimaging in small animal as a potential non-invasive imaging tool.

Despite being able to successfully image our brain model through the skull layer, to achieve this using our method we has to provide a significant amount of prior information of the skull layer in order to acquire high quality images. This included the location, morphology and velocity of this skull layer in the starting model. Furthermore, we also showed that while providing a reasonable prediction of this skull model was able to mitigate cycle skipping and allow for the partial reconstruction of the brain model, discrepancies between this predicted skull and the real skull model were found to produce artefacts in the soft tissue layers of the phantom. This may present a limitation for applying FWI in a clinical setting as it would suggest that the skull model would either need to be found using a different imaging modality beforehand or more accurate methods for predicting hard tissue structures such as the skull need to be found. This would potentially increase the running costs and reduce the impact of method as an medical imaging tool. There is evidence, however, that this may be problem may be overcome in part by extending the bandwidth of the transducers used. To demonstrate this we repeated the synthetic FWI experiment discussed in Section 5.3.3 where we attempted to image 2.5D phantom with the skull in place with the rotary array configuration, though this time we replaced our real signal P4-1 source signal with a broadband source with a lower -40dB limit at 0.07 MHz,

as shown in Figures 5.10c and 5.10d. Using this new broadbad dataset, the FWI reconstruction was repeated using a frequency stepping approach from 0.1 to 1.0 MHz with a water starting model. Unlike the inversion run that failed when using a water starting model and the real P4-1 signal, as shown in Figure 5.8i, we instead saw a successful FWI reconstruction of both the skull and brain when using this synthetic broadband dataset and signal, as shown in Figure 5.10b. This suggests that if we replaced our P4-1 probes with transducer arrays with greater low frequency content we may be able to recover whole 2.5D phantom without any prior information. Further experimental work would be required to confirm this.

## 5.5 Conclusions

In this study we have successfully demonstrated the feasibility of applying our 2D FWI algorithm to acquire high quality, high resolution images of a skull and brain mimicking phantom using data acquired experimentally. Imaging data was acquired using a novel USCT acquisition system consisting of a pair of independently translated medical cardiac probes. It was found that the best approach for imaging this phantom was to rotate both probes about the imaging target. Transducer positions were successfully calibrated for by developing a TOF localisation method using watershot data. Reconstructions of the soft brain tissue phantom were achieved without any prior information while it prior information about the morphology and velocity of the skull layer were required to successfully perform transcranial reconstruction of the brain phantom.

# Chapter 6

# Deep learning Driven Full-Waveform Inversion Breast Imaging

This chapter contains extracts from the following MDPI article published in *Sensors*:

> Robins T, Camacho J, Agudo OC, Herraiz JL, Guasch L. Deep-Learning-Driven Full-Waveform Inversion for Ultrasound Breast Imaging. *Sensors*. 2021; 21(13):4570. https://doi.org/10.3390/s21134570

I would like to acknowledge my team members on this project, including Jorge Camacho, who provided the reflection ultrasound tomography reconstructions of the CIRS breast phantoms, and Joaquin L. Herraiz, who contributed towards the quantitative analysis of the SoS reconstructions. I would also like to acknowledge M.D. Vicente Martinez de Vega (Hospital Universitario Quiron Salud, Madrid) for his help with the CT acquisition of the phantom, and Patricia Martinez & Gabriela Moreno for their help in the initial processing of multimodal images.

In addition to the research funding provided by the EPSRC, this work was

funded by the European Commission (EC) under Grant Agreement 777,222, and from the Instituto de Salud Carlos III, under the project DTS19/00059, FEDER for the ATTRACT research project "Ultrasound Breast Imaging with Deep learning".

## 6.1 Introduction

Successful reconstructions using conventional FWI are dependent on how close the initial acoustic model is to the true solution and whether the low-frequency content of the signal is sufficiently low enough to mitigate cycle skipping, a well-documented problem in applications of FWI in geophysics. This occurs when the misfit between the lowest-frequency signal content of the observed and synthetic data exceeds a half-cycle difference in time, causing the inversion to converge to the local minima [Bunks et al., 1995]. This makes it challenging to invert band-limited acquisitions with insufficient low-frequency content. As demonstrated by an in silico FWI breast imaging study by Calderon Agudo et al. [Calderon Agudo et al., 2018], USCT data with frequencies below 0.50 MHz were required to mitigate cycle skipping when using a conventional FWI algorithm. However, medical ultrasound-imaging probes are not typically designed to image sub-1.00 MHz frequencies, making them poorly suited to this task.

Mathematical low-frequency extrapolation methods were investigated to generate low-frequency signal content that may be missing from acquired data (Li and Demanet et al. [Li and Demanet, 2016]). However, these bandwidth extension approaches are recognised as nonlinear operations that add additional costs and are only able to estimate low-frequency content in controlled situations. An alternative approach to using a physics-based bandwidth extension algorithm is to instead pose this task as a machine-learning problem. This concept is supported by the universal-approximation theorem that states that a deep neural network (DNN) with a sufficient number of hidden layers can be used to approximate

any nonlinear function [Hornik et al., 1989]. For this application, this DNN would be used to approximate an operation that directly extrapolates the true low-frequency signal phase and amplitude values from band-limited signal data. This was demonstrated for geophysical applications by Sun et al. using a 1D convolutional neural network (CNN) that was trained to perform this task using synthetic data of a signal transmitted through acoustic subsurface models [Sun and Demanet, 2020].

In this study, I further explore this approach for bandwidth extension by implementing a U-Net-based 2D CNN architecture to preserve the signal structure along the time axis and across transducer channels when extrapolating low-frequency signal content. In Section 6.2, I describe the architecture of this proposed bandwidth extension CNN, and the methodology for generating realistic in silico USCT breast imaging data for training and evaluating the CNN solutions. Furthermore, I provide an overview of the USCT acquisition systems used to provide experimental USCT data of a realistic breast phantom. In Section 6.3, I discuss the results from applying the CNN solutions to both in silico and experimental band-limited FWI breast imaging problems. Lastly, in Section 6.4, I discuss the impact of the proposed bandwidth-extension solution to overcome the inherent limitations of band-limited ultrasound hardware when imaging the breast with FWI.

## 6.2 Materials and Methods

Here, I discuss the methodology used for training and testing the bandwidth extension CNN solutions for the low-frequency extrapolation of band-limited USCT data. These include PyTorch implementations of both a proposed U-Net based 2D CNN solution and the 1D CNN model described by Sun et al. [Sun and Demanet, 2020]. Both CNNs were run on a GTX 2080 Ti GPU (Nvidia, Santa Clara, CA, US) using the same training and testing datasets, allowing for the

performance of both bandwidth-extension methods to be compared. I then discuss the method used to generate synthetic USCT training, validation, and testing datasets using numerical SoS breast models provided by the OA-Breast database [Lou et al., 2017]. Lastly, I provide an overview of the experimental acquisition system used to image a CIRS 073 acoustic breast phantom [CIRS, 2014] to provide real-world USCT testing data. This system consisted of a pair of translated P4-1 cardiac probes (ATL, Bothell, WA, US) commonly found in clinical settings, and they were selected for being among the lowest-frequency transducers available in medical ultrasound. Despite these selection criteria, I demonstrate that these probes were still unable to image at sufficiently low frequencies to mitigate cycle skipping when using a conventional FWI algorithm without prior information about the breast phantom. Experimental USCT data were, therefore, band-limited, providing an ideal case study for testing the bandwidth-extension CNN solutions. The resulting SoS reconstructions from these tests were validated using a micro-CT scan (using a XT H 225 CT scanner, Nikon, Tokyo, Japan) and ultrasound reflectivity images (performed using a full-angle spatial-compound technique [Salido et al., 2016] of the CIRS breast phantom.

### 6.2.1 Bandwidth-Extension Network Architecture

The low-frequency extrapolation method proposed by Sun et al. [Sun and Demanet, 2019] used a feed-forward CNN model design with an architecture that consisted of five convolutional steps, each with parametric ReLU (PReLU) and batch-normalisation layers, to extrapolate broadband data from 1D trace inputs. This neural network was trained with a supervised-learning approach, where simulated infrasound transmissions (sub-20 Hz) through numerical acoustic subsurface models were used to generate paired band-limited and broadband infrasound acquisitions. These were used as the input and target data, respectively. Once trained, this CNN was sufficiently robust enough to extrapolate low-frequency content in a blind band-limited numerical dataset, resulting in improved FWI reconstructions [Sun and Demanet, 2020].

In this study, I investigate the impact of using a 2D CNN architecture to perform low-frequency extrapolation on 2D samples of signal data. The rationale for this approach was from the observation that sequential traces acquired across the elements of transducer arrays provide spatial context to the received data that could complement the time-variation information available in individual traces. For this reason, it may be beneficial for a CNN to be trained to preserve wavefront structure along both the time axis and these consecutive traces. For this task, a U-Net architecture, a CNN originally developed for biomedical-image segmentation [Ronneberger et al., 2015], was used. It is now widely used as an image-transformation tool, including for image-completion and image-sharpening tasks [Chen et al., 2018, Yao et al., 2018].

The U-Net consists of a contracting path where successive convolutional, ReLU, and max-pooling operations are applied to extract greater amounts of feature information as spatial information is reduced. This is followed by an expansive path where successive upsampling is applied to increase spatial resolution, allowing for the network to produce an output with the same image dimensions as those of the input (Figure 6.1). A notable feature of a U-Net is the use of concatenated skip connections, whereby feature maps from the contracting path are reused by concatenating them with feature maps of the expansive path. This allows for the network to preserve spatial information when forming the output image that would otherwise be lost. Input images were defined as $256 \times 96$ samples of ultrasound data (this corresponds to a window of 256 times samples taken across the 96 elements of a P4-1 probe shot gather for a given source).

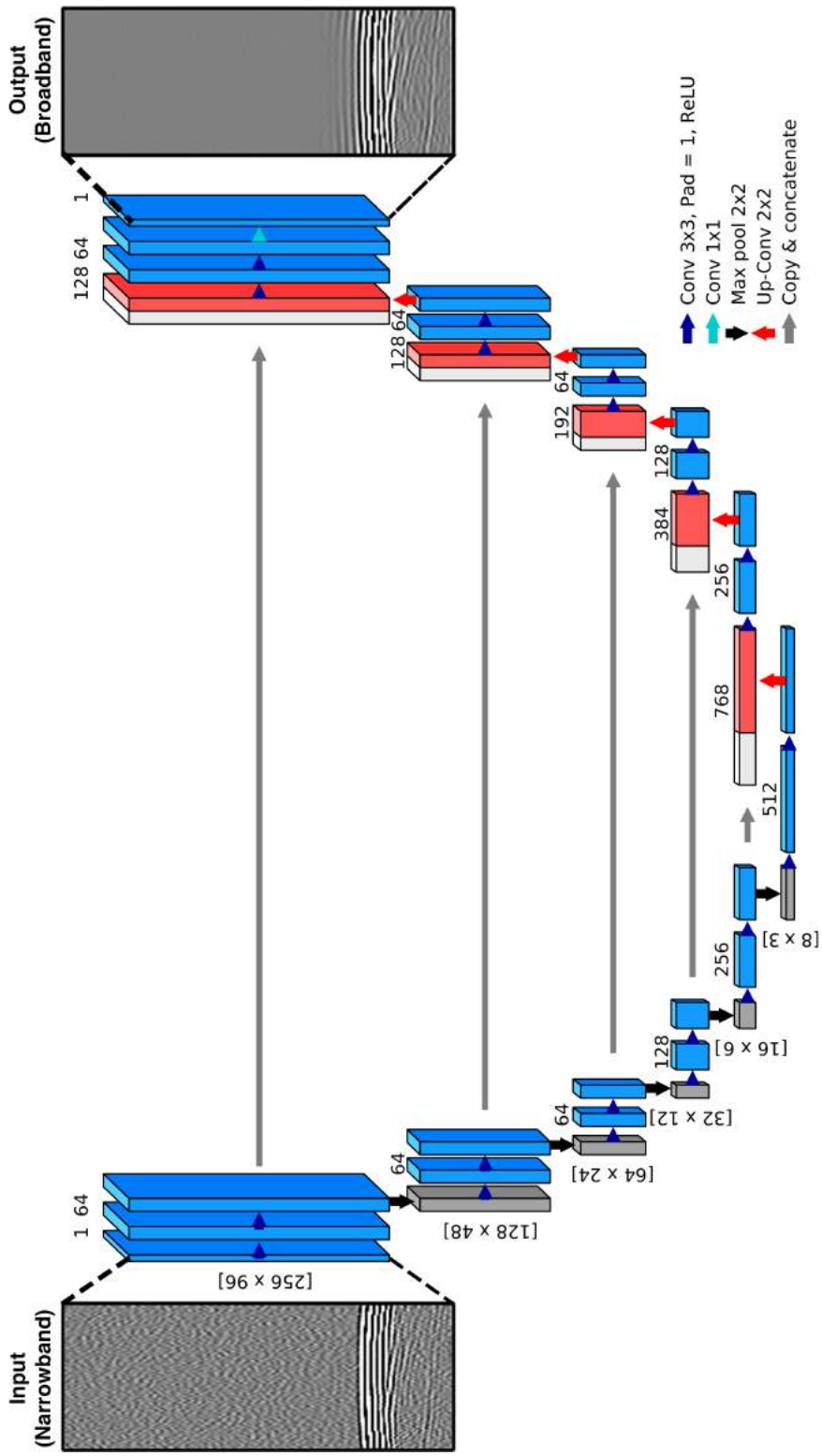


Figure 6.1: **U-net based CNN architecture for extrapolating low-frequency signal content for 2D input samples of ultrasound data.** Plotted volumes represent feature maps, with x,y dimensions given at the start of each row, while values above these blocks denote the number of channels. Grey blocks, downsampling steps; red blocks, upsampling steps; white blocks, corresponding feature maps that were copied over from the contracting steps.

### 6.2.2 Bandwidth-Extension Network Training

Synthetic USCT training data were generated by solving a numerical wave equation to simulate the propagation of acoustic waves through realistic SoS breast models. This allowed for corresponding band-limited and broadband USCT datasets to be generated for a range of different breast imaging problems, providing both the input and target data required to train the bandwidth extension CNNs by supervised learning. To avoid data overfitting, these datasets were created by imaging 8 randomly selected 2D slices from the OA-Breast database models. From the 8 sets of generated data, 4 were selected for training data, 2 were selected for use as validation data during training, and the remaining 2 were selected for testing. The set of transducer-element positions used to generate these datasets was modelled after the experimental acquisition system discussed in Section 6.2.5, which consists of a ring of 16 P4-1 probe positions around the breast models being imaged. Each of the resulting datasets provided 294,912 unique traces that could be randomly sampled for training the 1D CNN model, or 3072 unique sets of 96 element shot gathers for training the 2D CNN model. The augmentation of these data was performed by applying a random shift to the 256 time sampling window for each selected input datum ($\pm$144 time steps) and by applying a random flip to the order of the traces being sampled. By applying these augmentation steps, a total of $\sim$40 million unique 1D traces and 7,077,888 unique 96 trace shot gathers could be sampled for training the low-frequency extrapolation CNN models.

To ensure that the synthetic input data realistically represented real-world band-limited data, these datasets were generated using an input signal sampled from transmissions of the P4-1 probes. An example of the recovered P4-1 signal can be seen plotted in Figure 6.2b, which had a lower frequency limit at $-40$ dB of 0.52 MHz (as seen in the amplitude-spectrum plot for this signal in Figure 6.2d). According to the findings of the synthetic FWI study by Calderon Agudo et al. [Calderon Agudo et al., 2018], this suggests that the resulting datasets gener-

ated with this signal would have insufficient low-frequency content to mitigate cycle-skipping effects when running FWI. To demonstrate this, FWI was run (frequency stepping sequence, 0.50 to 1.20 MHz, 208 iterations) using a synthetic band-limited dataset generated by imaging the SoS breast model seen in Figure 6.2a using the P4-1 input signal. To perform this inversion without using any prior information about the breast model, a homogeneous water starting model set to 1484 $ms^{-1}$ was used. As shown in Figure 6.2f, this inversion was not able to successfully recover the true breast SoS model from this starting model, supporting the assumption that these datasets are not suitable for breast imaging using conventional FWI.

To generate the corresponding broadband target data, each simulated breast-model acquisition was repeated while instead using an ideal broadband source. This signal was designed to be both in-phase and morphologically similar to the observed P4-1 signal, but with greater signal content at lower frequencies. To create this signal, the high-frequency content of the P4-1 signal in the frequency domain (for amplitudes greater than 1.00 MHz) was combined with the lower-frequency signal content of an ideal 3-cycle broadband pulse. The resulting hybrid spectrum of these two signals had greater amplitudes at lower frequencies in Figure 6.2e than the original P4-1 signal did with a new lower $-40$ dB frequency limit of 0.07 MHz. An inverse fast Fourier transform of this hybrid frequency spectrum was then used to produce the ideal broadband signal seen plotted in the time domain in Figure 6.2e. To demonstrate the impact of using USCT data with this additional lower-frequency content, the breast model in Figure 6.2a was once again imaged, this time while using the ideal broadband source signal or generated broadband testing data. By running FWI with these broadband data (frequency-stepping sequence, 0.20 to 1.20 MHz, 208 iterations), a high-quality reconstruction of the breast model was recovered from a water starting model, as shown in the final iteration of this inversion in Figure 6.2e.

In addition to using an input signal sampled from real data, realistic noise designed to be similar noise to that observed when imaging with P4-1 probes was also

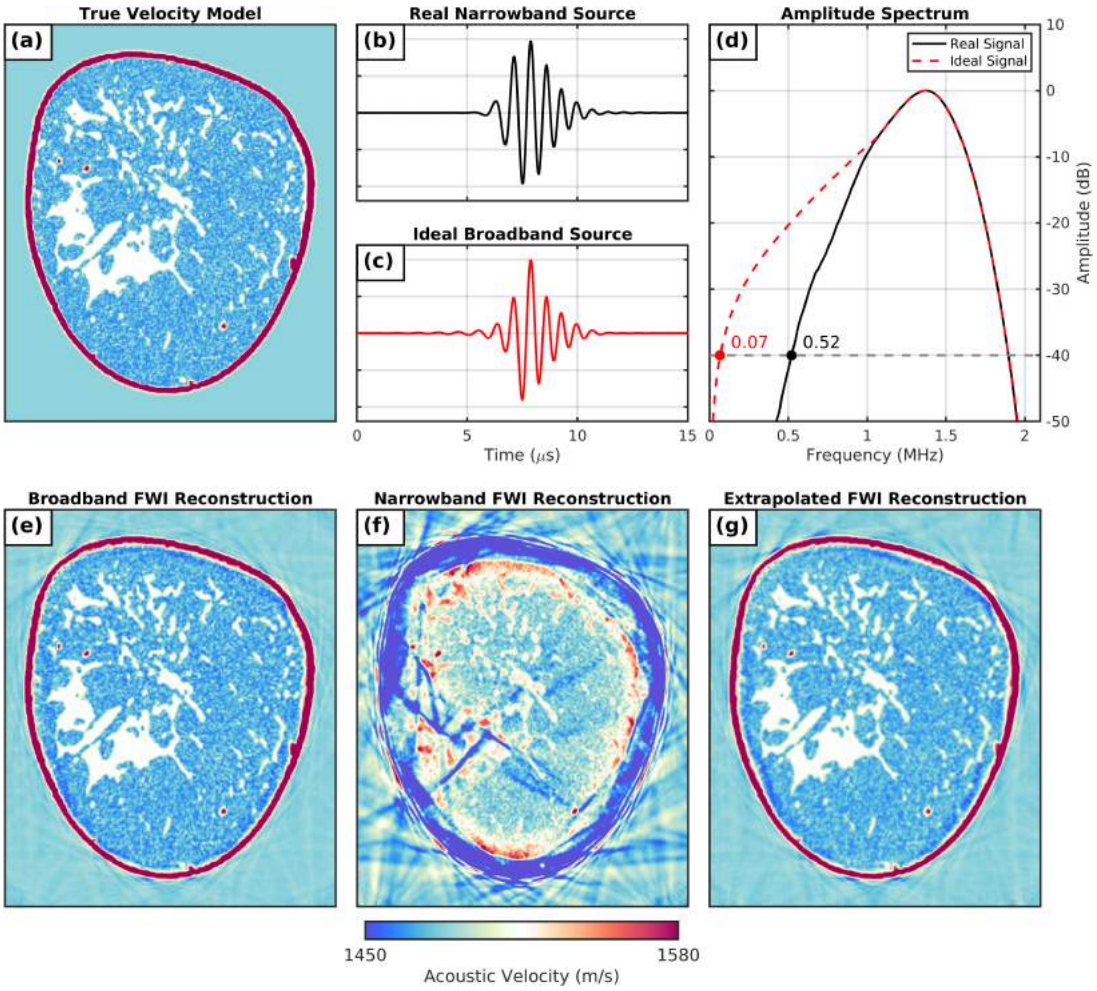


Figure 6.2: **Performance of the 2D U-Net low-frequency extrapolation in FWI**. (a) Coronal slice of a realistic numerical breast model. (b) Band-limited source signal extracted from real P4-1 transmission data and (c) Corresponding ideal broadband source signal. (d) Amplitude spectrum of real and ideal source signals. (e) Full-waveform inversion of broadband ultrasound data using ideal source signal. (f) Full-waveform inversion of bandlimited ultrasound data using real source signal. (g) Full-waveform inversion of narrow-band ultrasound data after being fed through a low-frequency extrapolation CNN.

added to the input datasets so that they would closely match real experimental data. This was achieved by training a simple Pix2Pix generative adversarial network (GAN) to produce noise maps until it was unable to distinguish between generated and real noise sampled from P4-1 imaging data. The target broadband data, however, did not receive this additional noise to encourage the network to suppress noise present in the input data, and to attempt to only preserve useful ultrasound signal content. These dataset pairs were then downsampled to reduce the computational load on GPUs.

### 6.2.3 Bandwidth-Extension Network Evaluation

Once trained, both the 1D and 2D bandwidth extension CNNs were evaluated by applying them to the band-limited input data of 15 additional synthetic breast imaging USCT testing datasets. These were generated using the same method as that described in Section 6.2.2 while only sampling breast models from OA-Breast data that had not already been used to create training data. For each of these cases, the resulting band-limited input dataset were passed to both CNNs to generate the extrapolated broadband data. For each test case, FWI was then performed across the different USCT datasets, including band-limited input data, ideal broadband data, and two extrapolated broadband datasets generated using the 1D CNN and U-Net-based 2D CNNs. All inversions were run using a homogeneous water starting model with a water velocity value of 1484 $ms^{-1}$.

As expected, none of the FWI reconstructions using band-limited data (frequency-stepping sequence, 0.50 to 1.20 MHz, iterations = 208) was able to successfully recover the true breast SoS models, and evidence of cycle-skipping artefacts was seen in all cases (as demonstrated by Figure 6.2f). Conversely, FWI reconstructions performed with ideal broadband data sets (frequency-stepping sequence, 0.20 to 1.20 MHz, iterations = 208) were all found to successfully recover the true numerical breast models for each test case (as demonstrated by Figure 6.2e). Lastly, FWI reconstructions using all extrapolated broadband datasets were also found to successfully recover the true SoS breast models for each test case. This suggests that both CNN solutions were able to both recover missing low-frequency content in the input data and, after performing this operation, to preserve the high-resolution imaging data of the input signal. An example of one of these successful FWI reconstructions using extrapolated broadband generated with the 2D CNN solution is shown in Figure 6.2g.

To compare the performance of the 1D CNN and 2D CNN bandwidth-extension models, the rms error between FWI reconstructions using extrapolated datasets

generated using both methods and the true SoS models was computed for each of the 15 test-case slices. The rms error found for all 1D CNN reconstructions was 5.287 $\pm$ 0.448 $ms^{-1}$, whereas the rms error for 2D CNN reconstructions was 4.530 $\pm$ 0.485 $ms^{-1}$. These results show that there were significantly smaller rms values when using the 2D CNN architecture then when using the 1D CNN method, confirming the hypothesis that including spatial information in the network results in more accurate predictions of low-frequency content in USCT data.

A closer look at the impact of the low-frequency extrapolation CNN models on ultrasound-signal data is shown in Figure 6.3, which shows collected data using one of the 15 in silico testing breast models. This includes traces plotted from the input band-limited data, ideal target broadband data, and the extrapolated broadband data generated by the CNNs. Each block of 96 traces represents the 96 receiving elements for probes moving clockwise in the ring array. To highlight the effect of the extrapolating low frequencies, a 0.10–0.25 MHz band-pass filter was applied to all datasets. Transmitted and reflected ultrasound signals were clearly present in the original broadband panel (Figure 6.3d), but this information was mostly lost in the band-limited data (Figure 6.3a). As shown in Figure 6.3b,c, this missing low-frequency signal was successfully recovered after applying the CNNs. However, in the 1D CNN traces, there were notable noisy artefacts that were not present in the true broadband traces or 2D CNN output traces. Again, this is evidence that it is beneficial to include spatial information during low-frequency extrapolation, as the network learnt that, while the noise did not have good lateral continuity, the USCT signal did.

Despite the successfully reconstruction of SoS breast models when using conventional FWI for all generated extrapolated datasets, there were notable limits as to how closely the CNNs were able to transform the input USCT signal into the corresponding ideal broadband target signal. This can be observed by calculating the rms error of each USCT dataset with respect to the ideal broadband

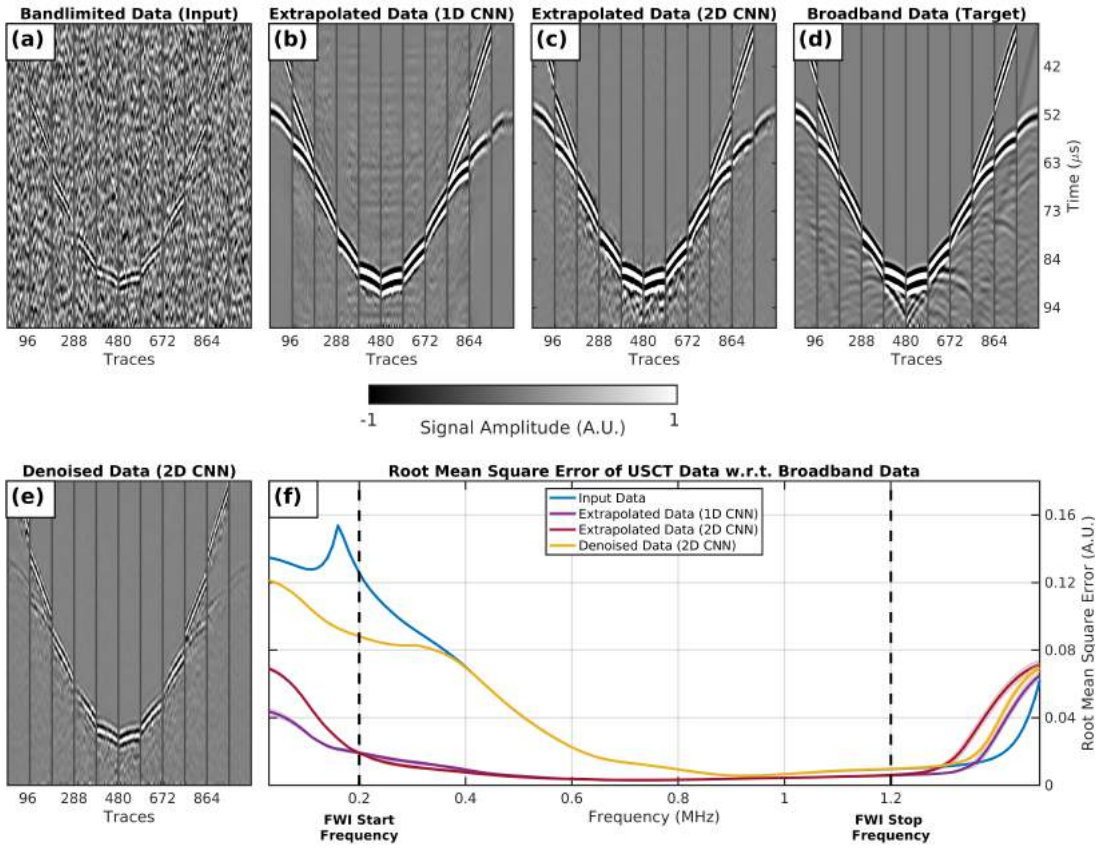


Figure 6.3: **Testing USCT data generated by imaging numerical breast models provided by the OA-Breast database**. Each set of 96 traces represents the received signal by the 96 elements of a P4-1 probe at 1 of the positions in the ring array. (a) Shot gather simulated using a realistic narrow-band P4-1 source signal and noise. (b) Shot gather after feeding band-limited signal data into the 1D CNN proposed by Sun et al. (c) Shot gather after feeding the band-limited signal data through the U-Net-based 2D CNN. (d) Shot gather simulated using a ideal broadband source signal without noise. (e) Shot gather after feeding band-limited signal data into the 2D CNN when trained to only perform a denoising operation. (f) Root-mean-square (rms) error of synthetic breast USCT data with respect to ideal broadband data with frequency.

case for different frequency bands, as seen plotted in Figure 6.3f. As expected, the rms error of the input USCT data for frequencies below the −40 dB data lower-frequency limit (0.52 MHz, as shown in Figure 6.2d) was significantly lower for the extrapolated data. This supports the observation that these extrapolated datasets match more closely with their ideal broadband cases compared to the input data. However, despite the ideal broadband having a −40 dB lower frequency limit of 0.07 MHz (as seen in Figure 6.2d) this error can be seen to increase for both extrapolated data cases for frequencies less than 0.2 MHz. This is due to the recovered signal content becoming gradually less coherent with the true

broadband low frequency signal for frequencies tending towards 0 Hz. Likewise, an upper limit of frequencies with low rms error values is visible around 1.20 MHz; after that, the rms error increased when moving towards higher frequencies. The extrapolated and ideal broadband datasets appeared to most closely match within the 0.2–1.2 MHz frequency range for all 15 testing breast model cases. For this reason, a starting frequency of 0.20 MHz and a stopping frequency of 1.20 MHz were chosen when running FWI with both the ideal broadband and the extrapolated broadband datasets.

### 6.2.4 Comparison with a Denoising U-Net Network

In addition to performing the bandwidth-extension operation, it can be observed that the investigated CNNs also denoise the input signal data. This can be attributed to training these CNNs using synthetic input training data with realistic noise while using ideal noise-free synthetic broadband target data. This encouraged the CNNs to not only predict missing frequency content, but to also filter out noise present in the input signal data. This can seen by comparing the noisy input signal data plotted in Figure 6.3a to the two output datasets in Figures 6.3b and 6.3c which have significantly reduced noise. Numerous other examples of denoising using CNNs with U-Net architectures like this can be found in the literature, such as those compared for denoising colour images in the review paper by Komatsu et al. [Komatsu and Gonsalves, 2020]. In this section I will discuss the contribution of this denoising application to improving the FWI breast reconstruction when using a water starting model.

For this study, a 2D U-Net denoising CNN was created by reppurposing the same CNN architecture described in Section 6.2.1. To train this CNN to only denoise input signal data, the target data consisted of the input of the data prior to applying the realistic P4-1 noise. This was to encourage the CNN to preserve the same band-limited input signal data while removing the added noise. Besides this change, the same training methodology discussed in Section 6.2.2 was applied. An

example of denoised output signal data can be seen in Figure 6.3e after passing through the noisy band-limited input data plotted in Figure 6.3a through the denoising CNN. While both sets of input and output data were found to share the same frequency spectra, the mean SNR of the input data was found to be $42.160 \pm 4.917$ dB, while a mean SNR of $67.258 \pm 5.0133$ dB was found for the denoiosed output data. This shows a significant increase in SNR compared to the input signal data, suggesting that this CNN has successfully performed the denoising operation.

To determine whether applying this denoising operation is sufficient to overcome cycle skipping, FWI was run using noisy band-limited input data, denoised band-limited output data (using the 2D denoising CNN) and extrapolated broadband output data (using the 2D bandwidth-extension CNN) for each of the USCT testing datasets discussed in Section 6.2.2. Example FWI reconstructions for of these breast model test cases can be seen in Figure 6.4. As demonstrated previously in Figure 6.2g, the 2D bandwidth-extension CNN can be applied to overcome cycle skipping and allow for a successful acoustic reconstruction of the breast to be recovered without prior information. This is again demonstrated in Figure 6.4d, which shows that the FWI reconstruction using extrapolated broadband data for this breast imaging problem closely matches the true SoS breast model seen in Figure 6.4a. However, the FWI reconstruction using both band-limited datasets, as seen plotted Figure 6.4b and Figure 6.4c for the denoised and noisy input cases respectively, clearly show very similar unsuccessful FWI reconstructions. This suggests that reducing the noise in the input signal data alone is insufficient to overcome cycle skipping when recovering acoustic breast models with band-limited input data.

### 6.2.5 Ultrasound-Tomography Acquisition

Two ultrasound imaging systems where used to acquire the experimental data. These were the Dual-Probe USCT Acquisition system developed at Imperial

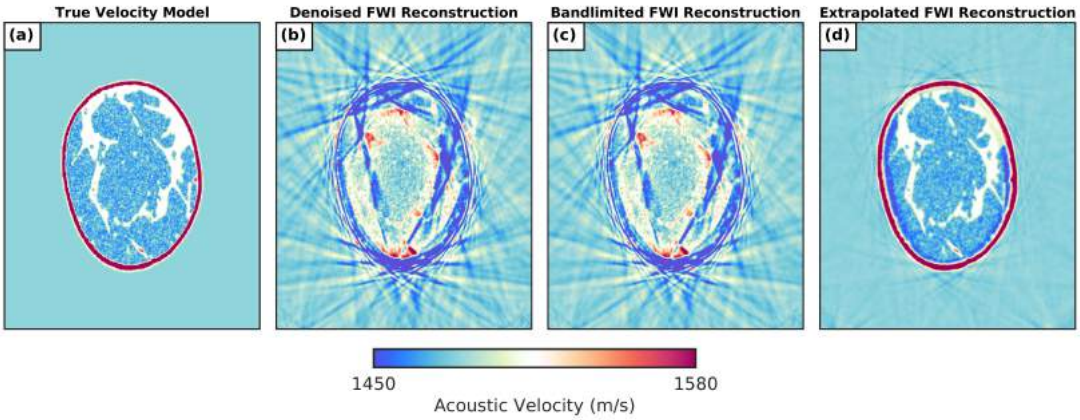


Figure 6.4: **Full-waveform inversion breast reconstruction using a 2D U-Net low-frequency extrapolation CNN compared to the 2D U-Net denoising CNN**. (a) Coronal slice of a realistic numerical breast model. (b) Full-waveform inversion using output denoised bandlimited ultrasound data generated using a 2D U-Net denoising CNN. (c) Full-waveform inversion using input bandlimited ultrasound data with noise. (d) Full-waveform inversion using output extrapolated broadband ultrasound data generated using a 2D U-Net bandwidth-extension CNN.

College London by the Transmission and Reflection Ultrasound Tomography (TRUST) research group, which was used to acquire USCT data for running FWI; and the Multi-Modal Ultrasound Breast Imaging platform (MUBI) developed at the Spanish National Research Council [Camacho et al., 2012], which was used to obtain reflectivity images. Both systems used pairs of independently rotated cardiac probes that could be positioned to allow for ultrasound data to be acquired for different source and receiver configurations. A 3D rendering of how a receiving probe (shown in blue) could be positioned relative to a transmitting probe (shown in yellow) while imaging the CIRS breast phantom is shown in Figure 6.5b. These acquisitions were performed in water tanks to provide a transmission medium between probes and breast phantom. The full volume of the phantom was acquired by adjusting its position in the vertical direction so that it could be imaged over several slices.

### Dual-Probe USCT Acquisition System

USCT was acquired using a system using dual 96-element P4-1 cardiac probes and a 256 channel Vantage ultrasound-imaging system (Verasonics, WA, USA).

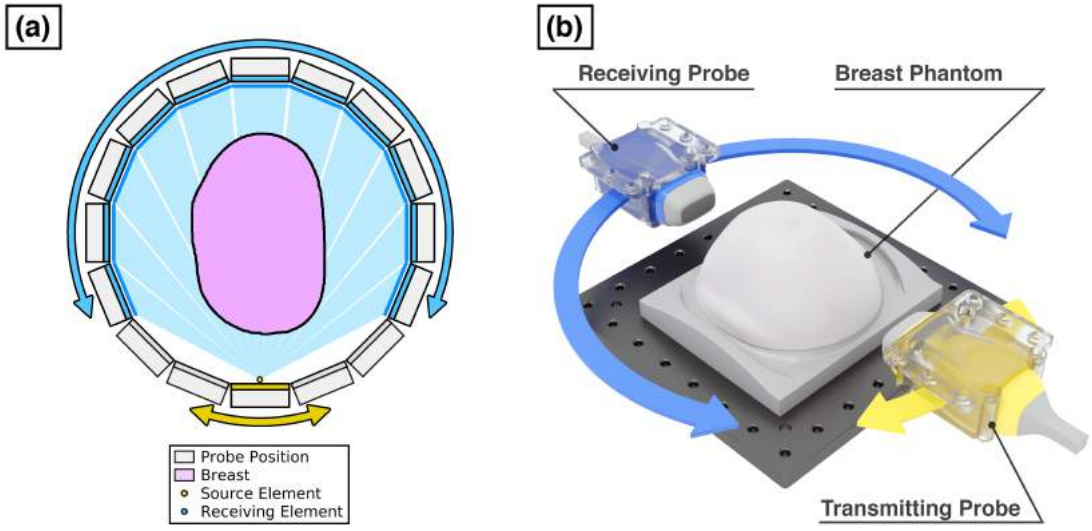


Figure 6.5: **Dual-probe ultrasound tomography acquisition system**. (a) Top-side view of acquisition ring formed by rotating receiving probe (blue) to acquire the signal at 11 opposing probe positions for all 16 source probe positions (yellow). Direct ray paths between a given source element shot to all receiving elements plotted in light blue. (b) 3D rendering of transmitting and receiving ultrasound probes relative to breast phantom.

Motors to control the rotation of these probes were a large aperture rotary motor (Standa, Vilnius, Lithuania) and a PRMTZ8/M motor (Thorlabs Inc.,Newton, NJ, US). To acquire the full USCT datasets for 2D slices of the breast phantom in both reflection and transmission, an imaging sequence was designed to simulate the data that could be acquired with a fixed ring array of ultrasound transducers. This resulting dataset then consisted of the acquired ultrasound signal for all possible source–receiver transducer element pairs. As illustrated in Figure 6.5a, this was achieved by rotating these probes to 16 possible source and receiver positions around the breast phantom to form a ring ∼200 mm in diameter. When the transmitting probe was placed at any one of these positions, the receiving prove could then be rotated to acquire data over the 11 opposing receiving positions (as indicated by the blue probe arrays for the single yellow transmitting element shown in Figure 6.5a). The full sequence consisted of repeating this acquisition for all 16 transmitting positions of the ring array.

Due to the nature of the scanning method used in this system, both the relative transducer positions and transmitted source wavelets were initially considered

to be unknown. These values were, therefore, estimated by extracting TOF information from a calibration USCT dataset acquired prior to placing the CIRS phantom for imaging. As the width of a P4-1 transducer element (width = 2.45 $\times$ $10^{-1}$ mm) was less than the minimal wavelength found in the observed data ($\lambda_{min} = 9.25 \times 10^{-1}$ mm), these elements were considered to be point sources and receivers in a 2D imaging plane. Element localisation was, therefore, performed by minimising the misfit between the computed travel of these modelled element points and the travel times experimentally found for all source–receiver element pairs. This was achieved by posing the problem as a nonlinear least-squares optimisation that could be iteratively solved using a Gauss–Newton algorithm [Filipík et al., 2012]. These optimised transducer positions could then be used to provide a wavelet estimate for each source. This was achieved by first applying a normal move-out (NMO) correction [Zhou, 2014] to all received signals for a given source, and then taking the mean signal across the resulting stack of coherently aligned traces. An example of a recovered source wavelet from these P4-1 probes is shown in Figure 6.2b.

**Reflectivity-Acquisition System**

Reflectivity images were acquired with the Multi-Modal Ultrasound Breast Imaging (MUBI) platform developed by CSIC [Camacho et al., 2012]. A single probe of 3.20 MHz, 128 elements, and 0.22 mm pitch (Prosonic, South Korea) was rotated around the phantom to the 16 positions of the probe ring array used by the Imperial College USCT system. At each probe position, a sector-scan reflectivity image was obtained, with 256 scan lines equally spaced between $-60$ and $60^{\text{o}}$, emission focus at 100 mm depth, and dynamic depth focusing on reception. The resulting images were formed in real time by a SITAU-112 ultrasound system with 128 parallel channels (Dasel SL, Madrid, Spain).

These 16 images were combined using the full-angle spatial-compound technique [Salido et al., 2016]. For each sector image, the interface between water and

phantom was automatically detected from ultrasound data, and the propagation direction of each scan line inside the phantom was corrected to account for the beam refraction. This process was repeated by changing the assumed average SoS of the tissue (unknown) between 1400 and 1600 $ms^{-1}$ with an optimization process that uses image sharpness as a beamforming quality measure to find the optimal SoS value [Medina et al., 2016]. Then, the 16 refraction-corrected images were converted into a common rectangular grid by bilinear interpolation and accumulated to obtain the full-angle spatially compounded image.

## 6.3 Results

In this section, I present results from applying a FWI algorithm and 2D CNN low-frequency extrapolation solution to two breast imaging problems with band-limited USCT data: (1) a 2D in silico dataset where the ground-truth breast phantom model was unknown, and (2) experimentally acquired 2D data by imaging a realistic CIRS breast phantom using the dual-probe acquisition system. Extrapolated broadband data were approximated for each problem set by feeding band-limited input data into a trained network, allowing for the study of the impact of extrapolating low-frequency signal content on the FWI reconstructions. To validate these results, the CIRS acoustic breast phantom was also imaged using reflection ultrasound tomography and X-ray computed tomography (CT).

### 6.3.1 in Silico Breast Phantom Experiment

An in silico breast phantom was used to provide both band-limited and broadband USCT data to test the 2D CNN bandwidth-extension solution. This was provided by the MUST 2019 Data Challenge and consisted of an SoS breast model that had been imaged using a ring array of 248 transducers acting as both

sources and receivers. FWI parameters, including true source signals, transducer positions, and water SoS were provided alongside this USCT challenge dataset. However, given that the aim of this challenge was to achieve the most accurate reconstruction of the numerical breast model, the true used SoS breast model was not released. This, therefore, provided an ideal blind imaging problem for this study.

The initial USCT dataset was found to be suitably broadband to overcome cycle skipping (0.20–4.00 MHz above −40 dB), allowing for a successful reconstruction of the numerical breast phantom to be recovered using FWI (frequency-stepping sequence, 0.20 to 1.20 MHz, 208 iterations), as shown in Figure 6.6a. This dataset was, therefore, used as a broadband reference. To provide a more realistic band-limited dataset, a high-pass filter (FIR, order = 40, cutoff = 0.55 MHz) was applied to the broadband dataset to remove frequency content below 0.50 MHz (this was to reflect the observed bandwidth when imaging with the P4-1 cardiac probes). As shown in Figure 6.6b, the FWI reconstruction using this filtered dataset resulted in cycle-skipping artefacts (frequency-stepping sequence, 0.50 to 1.20 MHz, 208 iterations). This prevented breast-tissue structures from being correctly recovered. A root mean square (rms) error of 36.593 $ms^{-1}$ was found between these band-limited and broadband (ground-truth) FWI reconstructions.

The 2D CNN bandwidth extension solution was then applied to produce an extrapolated broadband dataset. Rerunning the same FWI sequence used for the broadband ground-truth data resulted in an accurate reconstruction of the breast model that was comparable to the original broadband result (Figure 6.6c). High-resolution breast-tissue structures were also visible in the broadband ground-truth reconstruction, and a significantly reduced rms error of 6.965 $ms^{-1}$ was found between the extrapolated and ground-truth results, suggesting that the extrapolated dataset had sufficient low-frequency content to overcome cycle

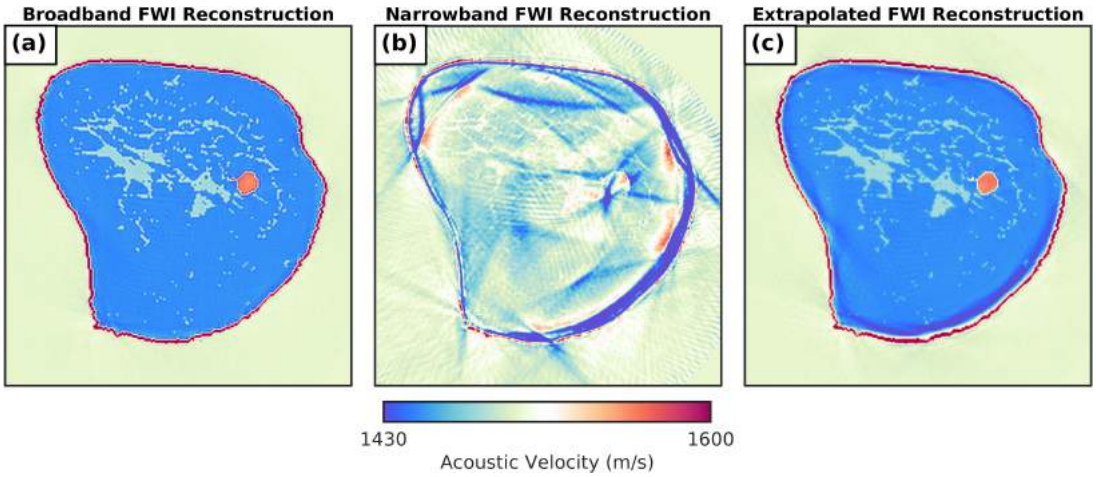


Figure 6.6: **Inversion results for in silico breast imaging data provided by MUST 2019 Data Challenge**. (a) Full-waveform inversion result using broadband signal data provided for the challenge. (b) full-waveform inversion result using narrow-band data acquired by high-pass filtering original broadband dataset. (c) Full-waveform inversion result using extrapolated broadband data generated using a U-Net CNN to recover missing low-frequency content removed from narrow-band data.

skipping. Inconsistencies in breast-tissue SoS values could be observed in some regions, but most notably along the lower boundary of the phantom. These may have been due discrepancies between how different output traces were encoded with information pertaining to the same model features within the extrapolated low-frequency signal.

### 6.3.2 CIRS Breast Phantom Experiment

Experimental USCT data were acquired by imaging the CIRS 073 breast phantom that had been designed to realistically reproduce breast morphology and acoustic SoS. This was performed using the dual-probe USCT acquisition illustrated in Figure 6.5 and discussed in Section 6.2.5 to image the phantom over 25 coronal slices, each separated by a step size of 2.00 mm.

FWI reconstructions of the CIRS breast phantom using USCT data acquired by the P4-1 probes did not appear to have sufficient low-frequency content to overcome cycle skipping. This resulted in numerous imaging artefacts and poorly reconstructed breast structures, as shown in Figure 6.7b. These results were

similar to those of the unsuccessful reconstructions discussed in Section 6.2.1, where cycle skipping was also observed when inverting the synthetic band-limited USCT data Figure 6.2f. When running FWI using the extrapolated data, however, the resulting reconstructions provided realistic breast phantom structures that were in good agreement with the micro-CT ground-truth model of the CIRS phantom, as shown in Figure 6.7d. In both extrapolated FWI and CT images, the phantom consisted of two distinct layers of breast-tissue mimicking material with contrasting density and SoS values to replicate the glandular and subcutaneous fat tissue layers of breasts in vivo. Furthermore, several small closely matching features were seen in both results including scatterers, cavities, and regions of higher density and SoS. However, the small cavities in the CT scan (outlined in cyan in Figure 6.7d) appeared to contain attenuation values similar to those of the air surrounding the phantom. This suggests that the phantom contained gas-filled cavities that I would not expect to see in real breast tissue. This appears to be a manufacturing defect in the CIRS 073 breast phantom, which was also reported in other publications [Kousaka et al., 2016]. Due to the limitations of the numerical-wave-equation solver in the presence of the large contrast between the acoustic properties of air (SoS $\approx$ 343 ms$^{-1}$, $\rho$ = 1204 kg m$^3$) and breast tissue (SoS $\approx$ 1400–1700 ms$^{-1}$, $\rho$ = 900–1057 kg m$^3$), the presence of these gas cavities had a detrimental effect on the quality of FWI reconstructions, resulting in reconstruction artefacts at positions that corresponded to these gas cavities.

### 6.3.3 Reflection Tomography

Figure 6.7a shows the reflectivity image for a slice of the CIRS phantom. The outer low-velocity layer present in the FWI image and the CT was also observed in the reflectivity image. In this case, it was a hypoechoic region of similar thickness, probably generated by less scattering material used for mimicking fat tissue. In the interior of the phantom, quite a different texture was observed. Filament-like structures were present in the reflectivity images, which could be explained by the nonuniform concentration of scatterers that locally affect material reflectivity

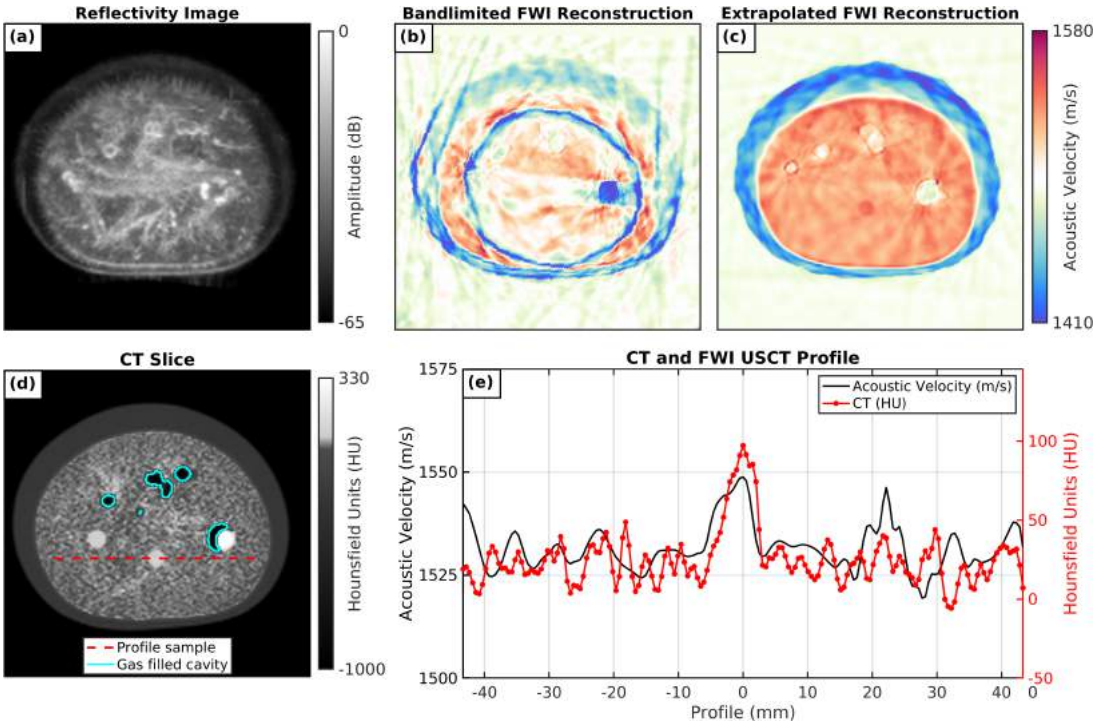


Figure 6.7: **Results from imaging a cross-sectional slice of the CIRS breast phantom**. (**a**) Reflectivity image with full-angle spatial-compound technique with refraction correction and 65 dB dynamic range. (**b**) Full-waveform inversion reconstruction using using narrow-band data. (**c**) Full-waveform inversion reconstruction using using low-frequency extrapolated data. (**d**) CT with gas-filled cavities highlighted in cyan. (**e**) Profile of CT and FWI USCT along the phantom in a region with a uniform background and a central area with higher density.

but do not significantly change the SoS, at least at the resolution range of the FWI reconstruction. This pattern was also observed in the CT by restricting the greyscale palette for observing subtle density changes (see Figure 6.7d), which confirmed its presence and discarded a possible reflectivity reconstruction artefact. On the other hand, not all cysts and masses seen in the FWI reconstruction (see Figure 6.7c) were seen in the reflectivity image. This was expected because some of the simulated lesions had different stiffness than, but similar reflectivity to, those of the background material. This observation reinforces the hypothesis that multimodal ultrasound imaging, combining reflectivity and SoS modalities, provides complementary information that could improve cancer diagnosis.

### 6.3.4 Quantitative-Analysis Results

In order to evaluate the accuracy of the reconstructed images with the proposed method, quantitative analysis was performed. First, the reconstructed FWI USCT images of the CIRS-073 breast phantom were coregistered with the CT acquisition by using a set of landmarks that could be easily identified in both image modalities, as is shown in Figure 6.7. Then, three different sets of regions of interest (ROI) were identified that were visible in both the CT and FWI images. These corresponded to a background with similar density to that of soft tissue (CT number between 0 and 50), regions with slightly higher density (CT number between 50 and 100), and ROIs with the highest density (CT number higher than 100). As the identified gas-filled cavities in the CT images were not realistic, they were omitted from quantitative analysis.

The analytical results of the values of these regions are summarized in Figure 6.8. SoS values were significantly higher for regions in Set 2 (moderate high density), while Set 3 (high density) had similar SoS to that of the background (Set 1). This agreed with the available information from the CIRS-073 phantom brochure [CIRS, 2014]. A profile along the CT and FWI USCT images (Figure 6.7e) confirmed that there was good agreement between the results of the two independent reconstructions. The region with HU around 100 had a significantly higher SoS (around 1550 $ms^{-1}$).

## 6.4 Discussion

FWI could transform ultrasound breast imaging. It can produce images at a comparable resolution to that in mammography but while using a safe, painfree, and more universally applicable solution. However, practical implementations require frequencies below 1.00 MHz to avoid cycle skipping and to reduce computational costs. The lack of sub-megahertz energy with sufficient SNR is common in USCT

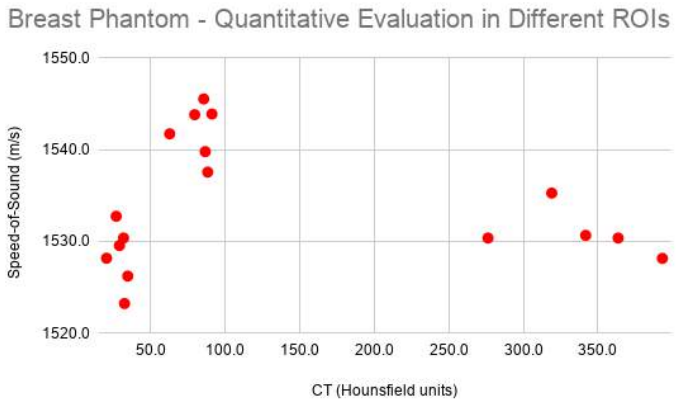


Figure 6.8: Values of speed of sound of different obtained regions from the FWI USCT images, and their corresponding Hounsfield units from CT.

acquisition devices, as they are often designed to generate data for ray-based imaging methods that require high frequencies to produce images with adequate resolution to be diagnostically useful.

To circumvent the deficit of low-frequency data, I implemented a solution based on a U-Net-based 2D CNN that could successfully extend the bandwidth of ultrasound datasets towards the low end of the amplitude spectrum. The output datasets from the network contained an accurate estimation of what this low-frequency information would be if broader-band transducers were available, and they could produce accurate FWI reconstructions where the original data with missing low-frequency information failed. I demonstrated that it is possible to train the network with in silico datasets, and that the trained network performed well when exposed to data acquired in the laboratory. This suggests that the method is robust against noise present in real data, and that it could learn the mapping between high and low frequencies purely from numerical simulations of ultrasound wave propagation.

The validation on laboratory data resulted in SoS images that were morphologically consistent with X-ray CT and ultrasound reflection tomography, with added quantitative information of physical properties. Nonetheless, the reconstructed images contained artefacts due to the geometry of the acquisition system: trans-

ducers were distributed in a ring that moved along its normal axis. Despite the relatively focused illumination on the ring plane, there was significant energy that propagated outside this plane that interacted with the acoustic heterogeneities that existed there. These interactions wre inevitably mapped onto the data, and the final images thereby suffered from a lack of resolution along the axis perpendicular to the ring plane. This problem could be solved by simply using data acquired with a 3D system that could capture ultrasound energy at all angles. The extension of the method to 3D datasets is straightforward. Comparisons of the performance of 1D and 2D CNNs on the 2D datasets showed some differences between the outputs of the two networks, but most of the performance gains that I observed in the 2D case could have been due to the presence of the spatial-distribution context. Extending the network inputs from 2D to 3D did not benefit as much from this extra information because the third added dimension contained already captured information in the addition of the second dimension. In other words, the difference between 1D and 2D was that the data transformed from a pure time series of values into a collection of spatially ordered time series; the third dimension only added a relatively redundant spatial dimension.

The continuous increase in computational capabilities is creating a shift in ultrasound imaging. Wave-equation-based reconstruction methods such as FWI continue to reconstruct images with better resolution and accuracy than those of ray-based alternatives. However, there is still a large computational cost to jump between the two that limits the applicability of wave-based methods to lower frequencies than those used in ray-tracing methods. The proposed method offers a solution that allows for both ray-tracing and wave-based ultrasound imaging on the same data by extending the original bandwidth. With further research into DNN USCT applications, it may be possible reduce this cost significantly by directly predicting SoS models of breast models from signal data. This could be achieved by providing a sufficiently large synthetic training data of USCT signal data as input and corresponding true SoS maps as target outputs. However, using this study as an example, a given input dataset can be more than 4 GB

to generate a high quality FWI reconstruction. Even with downsampling and small batch sizes, generating and loading a sufficiently large training dataset to train such a DNN would be computationally challenging. For this reason it may even be computationally infeasible to train a DNN to perform 3D FWI using conventional and affordable hardware. This training dataset would also need to contain a sufficiently diverse set of imaging problems to account for a large population of patients and the large number of potential pathologies to avoid overfitting. By training our CNN solution to instead perform a signal processing operations prior to running conventional FWI, we were able to ensure that our SoS reconstructions were instead acquired using a reliable, wave-equation-based solution. Alternatively, integrated DNN and FWI solutions have recently been proposed for FWI applications in geophysics, such as the approach discussed by Zhu *et al.* [Zhu et al., 2021], and this will no doubt be an exciting area of research when exploring further applications of FWI in medical imaging.

Lastly, the proposed method can not only be used for improving FWI. A reliable method to extend the frequency content of band-limited ultrasound signals can also be used to overcome the physical limitations of PZT crystals, extending the use of existing US hardware for other frequency ranges or predicting produced data by an ideal US hardware system.

## 6.5 Conclusions

In this work, I showed how a 2D CNN such as U-Net can be used to extend the frequency content of USCT data for FWI breast imaging. Realistic in silico USCT data were generated to provide input and target data to train a CNN to perform this bandwidth-extension operation. The performance of the CNN was then evaluated using simulated and experimental FWI breast phantom imaging problems with band-limited input data. I demonstrated how applying the CNN as a prepossessing step to the input data could be used to recover missing low frequencies, allowing for FWI to be run without cycle skipping. By doing so, I was

able to recover high-resolution quantitative SoS models of the breast phantoms despite starting with input data that were not suitable for FWI breast imaging. The preprocessing of acquired USCT data with trained bandwidth-extension CNN solutions may become a standard procedure prior to running FWI, similar to the application of some currently used filters. Lastly, this approach could be used to overcome the physical limitations of ultrasound hardware that images with suboptimal bandwidths.

# Chapter 7

# Towards 3D Full-Waveform Inversion in Small Animals

As previously discussed in Chapter 5, it has been shown that to successfully image complex three dimensional (3D) geometries like the brain with FWI, a 3D FWI algorithm is required to overcome out of plane effects. Furthermore, despite being among the lowest frequency medical transducers available, the P4-1 cardiac probes (ATL, USA) used in this study were found to have insufficient low frequency content to image the ultrasound breast phantoms discussed in Chapter 6 without the application of a deep learning low frequency extrapolation solution. However, given that the maximum resolution that can be achieved using FWI was found to be the resolution of half a wavelength, the upper bandwidth limit of in P4-1 data would allow for FWI to be run at higher frequencies than those previously considered in this thesis, potentially allowing for high resolution FWI applications of smaller imaging targets. This is assuming that the amplitudes and frequencies being considered would remain sufficiently low that the ultrasound propagation can still be assumed to be linear [Zhou, 2014]. From these observations I decided to investigate the application of dual probe 3D FWI tomography as a novel non-invasive neuroimaging technique for small animal subjects.

I have presented findings from this research at the International Ultrasonics

Symposium (Kobe, Japan):

> Robins, T., Cueto, C., Agudo, O. C., Guasch, L., Warner, M., Tang M. (2018). 3D Transcranial Ultrasound Tomography of the Brain in Small Animals using Full-Waveform Inversion – an Initial Feasibility Study. *In: International Ultrasonics Symposium*, Kobe, Japan, 22-25 October 2018.

and at the International Medical Ultrasound Tomography (MUST) conference in Detroit (MI,USA):

> Robins, T., Cueto, C., Agudo, O. C., Guasch, L., Warner, M., Tang M. (2019). Towards 3D Brain Imaging in Small Animals using Full-Waveform Inversion. *In: International Workshop on Medical Ultrasound Tomography*, Detroit, MI, 14-15 October 2019.

In this chapter I will cover both the *in silico* results presented at these conferences and the most recent findings in this work. This chapter also serves as a discussion about future work of the novel FWI imaging methods discussed in this thesis and the steps to be taken to further explore this imaging modality as a potential neuroimaging technique for animal research.

## 7.1 Introduction

Non-invasive neuroimaging is considered to be highly valued in translational animal model research, a field which aims to bridge the gap between observations made in animal subjects and humans to improve our understanding of neurological diseases and for the development of pharmacotherapeutic treatments [Belzung and Lemoine, 2011] [Hoyer et al., 2014]. These methods provide an ideal way of investigating the brain with minimal impact to the animal subjects and, by allowing for repeated measurements, the size of experimental groups can be reduced

(adhering to the first of the 3Rs for humane experimental approach proposed by Russel and Burch [Russell and Burch, 1959]) and allow for studies investigating changes in brain tissue and behaviour over time to be carried out. Furthermore, the use of non-invasive imaging also allows for multimodal investigations to be carried out on the same animal subject so that structural and functional imaging can be performed simultaneously [Walter et al., 2009][Waerzeggers et al., 2010].

Magnetic resonance imaging (MRI) is currently the gold standard for structural imaging of the brain in humans due to the high soft tissue contrast. While this is also true for neuroimaging small animals such as mice, the limited resolution presents a number of challenges when using this modality. With an average human brain volume of ∼1260 $mm^3$ [Peters et al., 1998][Allen et al., 2002] ∼440 $mm^3$ [Vincent et al., 2010], stronger magnetic fields are required to successfully image the mouse brain. To achieve comparable performance found when imaging the human brain with a 3-Tesla scanners a 9.4-Tesla scanner is required for mouse brain imaging. Even at this field strength repeated signal acquisitions are also required.

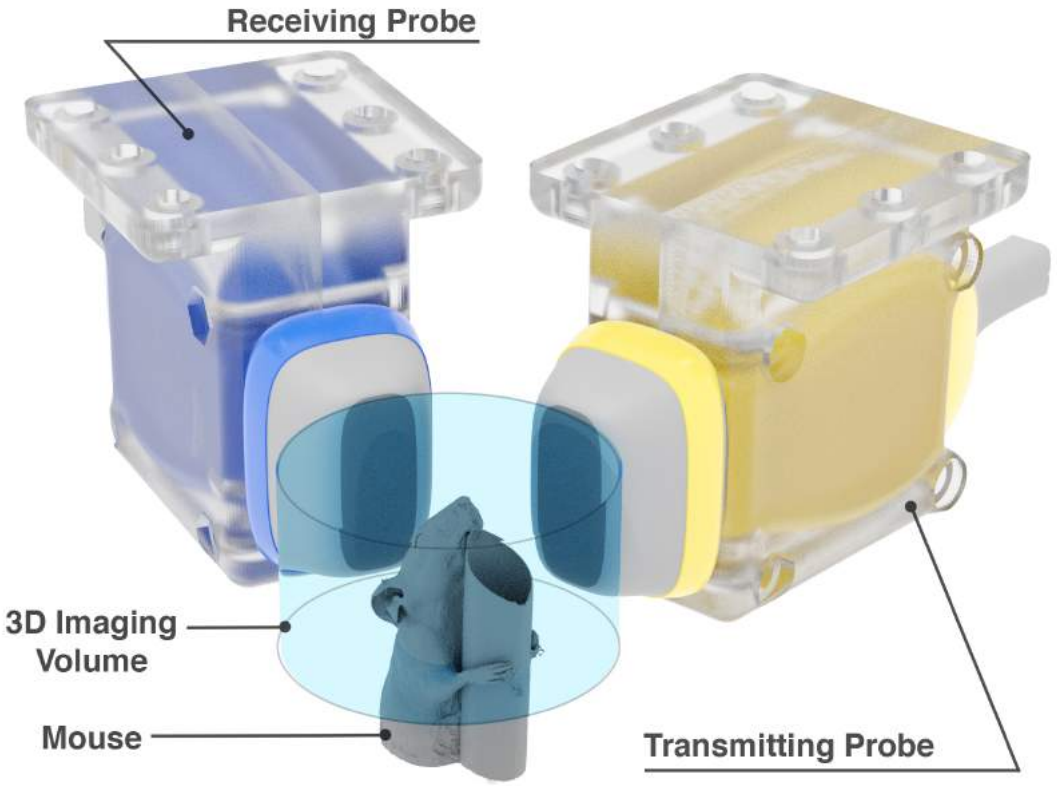


Figure 7.1: **Cylindrical 3D dual probe acquisition configuration for imaging a mouse head**. Here the cylindrical volume can be imaged in 3D by performing a rotary imaging sequence while the probes are placed vertically.

Compared to the high cost and limited availability of MRI, ultrasound could offer an alternative technology for non-invasive imaging of the brain in small animals. In this chapter I will demonstrate the feasibility of an novel neuroimaging method for small animals *in silico* using 3D FWI to perform transcranial tomography towards the development an alternative acoustic tomography based neuroimaging modality for animal research.

## 7.2 Materials and Methods

### 7.2.1 In Silico Mouse Head Phantom

To create a realistic mouse skull and brain acoustic model to image *in silico*, high resolution 3D CT and MRI models of the adult murine head for strains C57Bl/6j

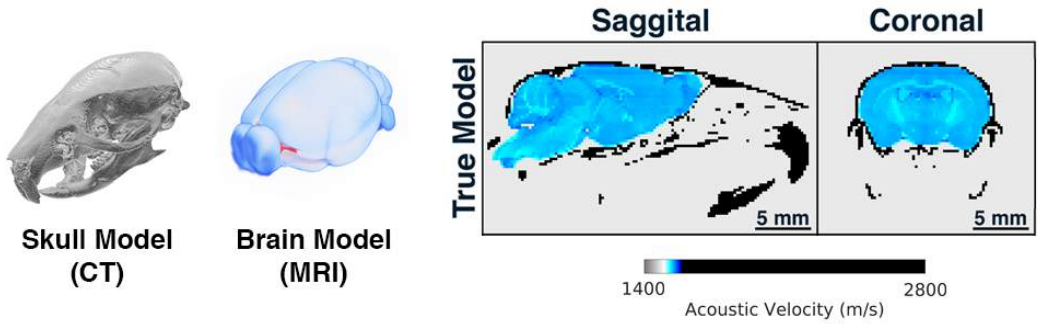


Figure 7.2: **3D mouse skull and brain imaging phantom**

were provided by the Henderson Laboratory at the University of Toronto [Chan et al., 2007]. Here a linear empirical relation between Hounsfield units (HU), density and acoustic velocity was used to estimate the sound speed of the skull from this CT model [Mast, 2000] while a scaling to estimate realistic acoustic velocity of the brain was achieved using the tissue properties datasbase V4.0 provided by the IT'IS Foundation [Hasgall et al., 2012]. Renders of the original CT and MRI models of this mouse head can be seen in Figure 7.2 alongside the generated *in silico* mouse brain and skull phantom.

### 7.2.2 Transcranial USCT Data Acquisition

3D USCT data of transcranial imaging problems were acquired by simulating scans of acoustic models using the 3D cylindrical configuration of the dual P4-1 probes shown in Figure 7.1. This is a variation of the 2D dual probe acquisition system discussed in Chapter 4. In this configuration, the P4-1 probes are orientated vertically to create the 3D cylindrical imaging volume. As these probes are rotated, each of the 96 probe element can transmit and receive ultrasound signal data across to the 96 elements of the other probe. This can be used to simulate a fixed cylindrical array consisting of a maximum of 96 stacked ring arrays formed the rotated P4-1 transducer elements. An illustration of this configuration when applied to image a mouse head can be seen in Figure 7.3.

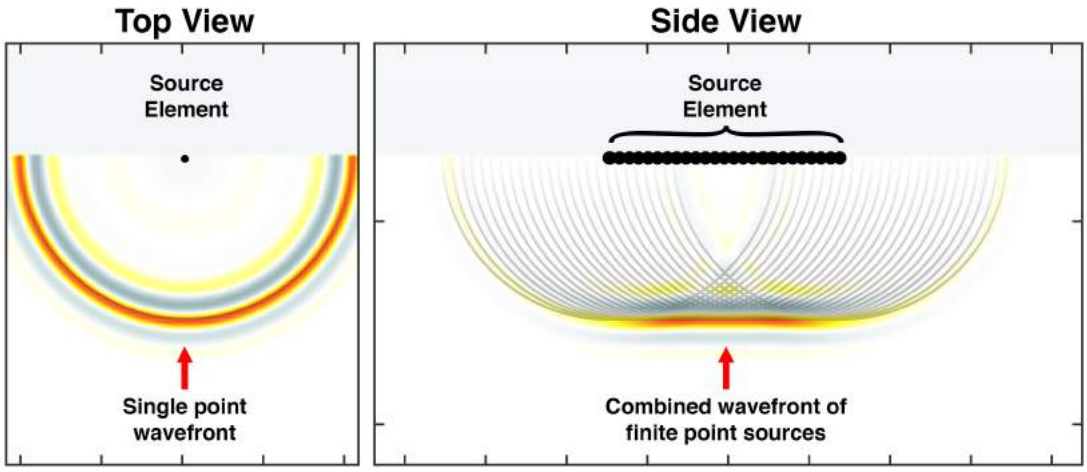


Figure 7.3: **Cylindrical transmission of P4-1 probe element in 3D**. By transmitting multiple finite point sources simultaneously it is possible to model to transmission of a P4-1 element in 3D *in silico* acoustic simulations.

### 7.2.3 Modelling Ultrasound Transducers

When attempting to use the dual probes to image in 3D, the elements of the P4-1 probe can no longer be modelled as point receivers and sources transmitting spherical waves. As the true P4-1 elements are long (height$\simeq$13 mm) and thin (element width = 2.45 x $10^{-}1$ mm), their transmission more closely resembles a cylindrical wave source. The simplest way to represent these elements in 3D imaging problems would be to model them as lines of finite points. The combined wavefront of these individual point sources allows for a cylindrical source to be modelled using the Huygens principle [Pinto, 2010], as demonstrated in Figure 7.3. The resulting wavefield is comparable to the real P4-1 seen in transmission when measured with the plane of hydrophone receivers described in Section 4.2.

### 7.2.4 Imaging Array Parameters Selection

In this section I will discuss the methodology for designing the configuration of the cylindrical array composed of the rotated dual probe positions. For the 3D dual probe system to be feasible, the cylindrical array would need to have a sufficiently high number of transducer elements distributed over a large enough cylindrical surface area to completely surround the imaging target. However,

for this method to be performed experimentally a low run-time is required to complete the imaging sequence for this method to be feasible. This is because the assumption that the water velocity remains constant and that the imaging target remains stationary throughout the scan becomes less likely to be true as the acquisition run-time becomes longer. For this reason, scan times should ideally be kept to less than 2 hours long. In addition to demonstrating the feasibility of 3D FWI for the transcranial imaging of small animals, this *in silico* study was also designed determine any potential imaging array configurations that would allow sufficiently large 3D USCT datasets to be acquired for the shortest possible USCT data acquisition run-time. To achieve this, a grid search using a simple transcranial imaging problem was performed to optimise across different source and receiver array configurations. This grid search was repeated while using both point and cylindrical transducer elements so that the performance of both transducer element types could be compared.

The benefit of imaging a target as small as a mouse head using the 3D dual probe system is that, unlike in previous dual probe FWI applications discussed in this thesis, the mouse head is smaller than the aperture of the probe, meaning that it's likely that linear translations of the probes in the transducer lateral direction will not be necessary. When used in tge 2D dual probe imaging configuration, it was possible complete a ring array with a large number of transducer elements quickly as a maximum of 96 element positions could be added to the ring array for every transducer array position, as seen in Chapters 5 and 6. However, when these probes are positioned vertically a significantly greater number of rotary steps is required to create ring arrays with many transducer elements. This makes experimental acquisitions with this method infeasible for a large number of source and receiver ring array positions. As transmitting and receiving wavefield signal data using stationary probes can be performed quickly, the rate determining step in each acquisition was determined to be the motor translation step in addition to the time required for the translated probe to come to rest. Given N as the number of transmitting source array positions within a ring array and M as the number of receiving array positions per source array position, the run-time of an

imaging sequence is largely determined by the time taken to perform $4MN + 2$ motor steps (when including initialising and resetting motor steps). From time measurements taken in the lab, the time taken to complete a motor step, allow for the probes to come to a complete stop and acquire USCT data was found to be 2.89 s when using this configuration. To minimise the time taken to complete a 3D USCT acquisition, the lowest possible values for M and N need determined to be while the acquired data is still sufficiently able to recover clinically useful acoustic models.

To perform the imaging array grid search, 2D FWI reconstructions were acquired using USCT data generated from imaging the *in silico* mouse head cross-section seen in Figure 7.4 for all combinations of N and M where N is a set of values denoting the number of source elements in the ring array ($N = \{8, 16, 32, 64, 128, 256\}$) and M is a set of values denoting the number of receiving elements per source ($M = \{20, 38, 74, 146\}$). This grid search was performed for a single ring array 2D imaging problem as running these grid searches using 3D FWI would have been computationally expensive and have required long run-times. Given that the mouse head is approximately 11.97 mm wide, the ring array was given a diameter of 20.00 mm. For each imaging problem, all sources were equally distributed about the ring array. As discussed in Section 4.2 for the 2D ring array USCT acquisition system, no receiver element positions were placed either side of the source array to prevent the probes from colliding during real acquisitions (in this case only the the furthest 57% of receiver positions from a set of equally spaced ring array positions were considered for any given source). All. receiver positions were equally distributed outside of this collision zone. This grid search was repeated when modelling with both point and cylindrical P4-1 elements to measure the impact of using more realistic P4-1 wavefield data. Each FWI image reconstruction was run for 160 iterations using a frequency stepping method from 0.60-2.50 MHz. The transmitted signals used for this were experimentally obtained from the P4-1 probes watershot data.

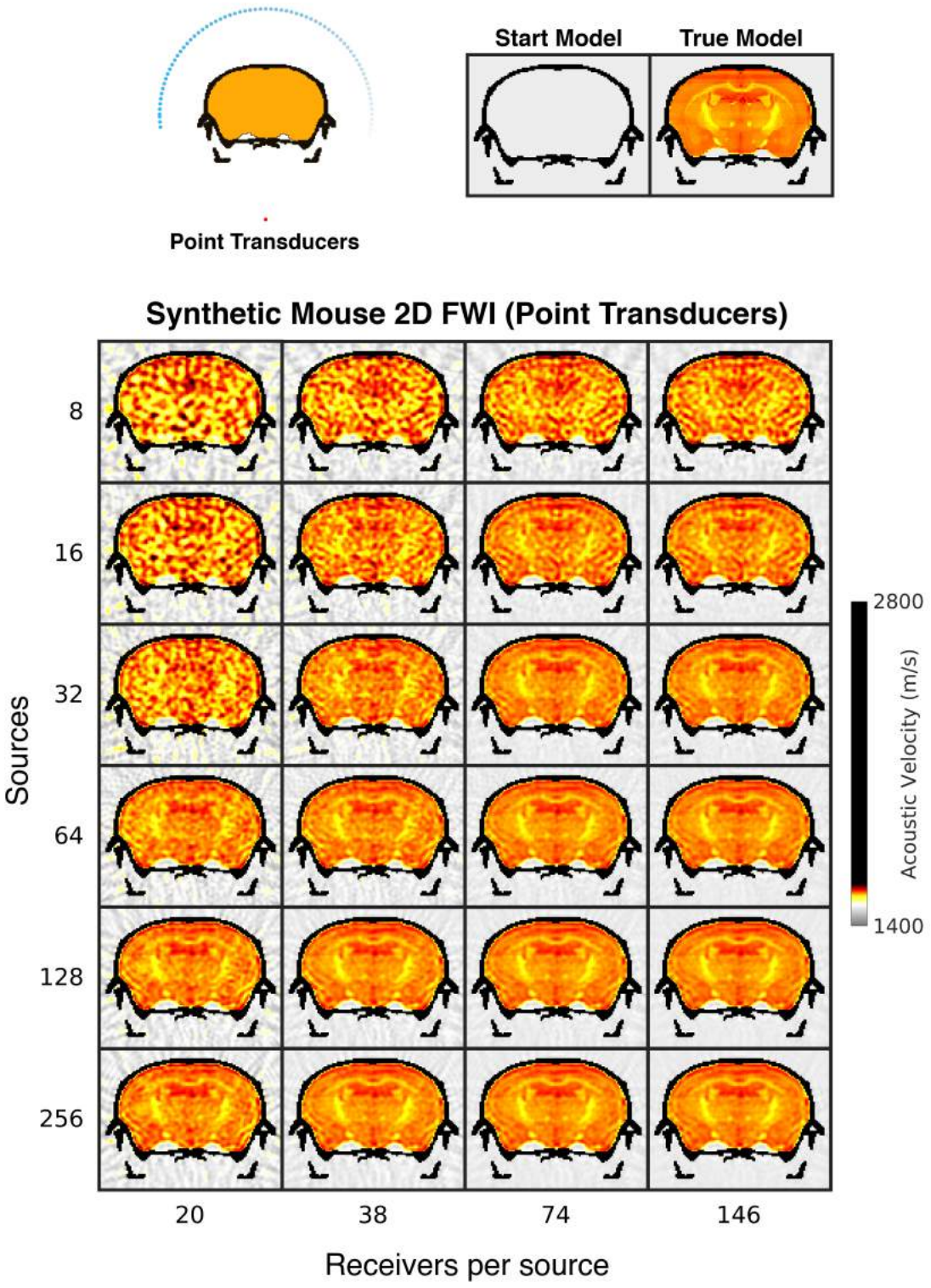


Figure 7.4: **Full-waveform inversion grid search results for evaluating the impact of the number of point sources and receivers on the reconstruction of a mouse head cross-section.**

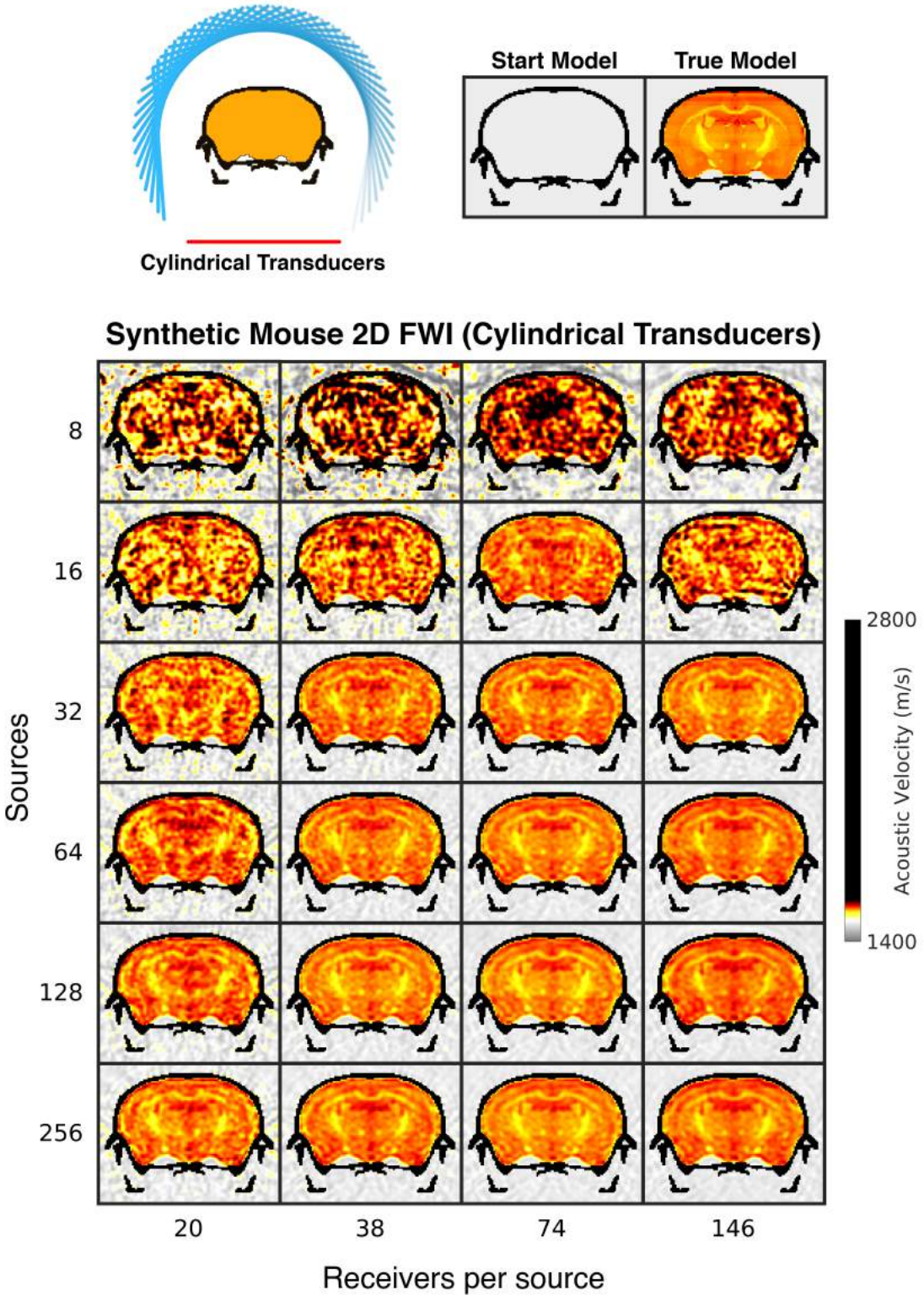


Figure 7.5: **Full-waveform inversion grid search results for evaluating the impact of the number of cylindrical element sources and receivers on the reconstruction of a mouse head cross-section.**

## 7.3 Results

### 7.3.1 Imaging Array Grid Search

In Figures 7.4 and 7.5, 2D FWI reconstructions of a mouse head can be seen for different combinations of source and receiver arrays while using both point and cylindrical elements respectively. Each reconstruction provides a grid point for the grid search discussed in Section 7.2.4 in order to determine the impact of using N sources and M receivers per source on the quality of FWI reconstructions. In both figures, the impact of having insufficient source and receiver positions can clearly been seen by how the reconstructions tend to more closely resemble the true model as N and M values were increased and by how the reconstructions tend to fail as fewer total transducer elements were used.

To evaluate each SoS reconstruction, the rms error relative to the true velocity model shown in Figure 7.4 were calculated and plotted in corresponding grids for each grid search in Figure 7.6 alongside the run time for each configuration. When comparing the set of rms values found when using point elements to those seen when using cylindrical elements, we can see that using cylindrical P4-1 elements results in reconstructions with a slightly higher error in the highest quality reconstructions (which in both cases can be considered to be those with 32 or more sources and 38 or more receivers per source). This is understandable due to the lost resolution that would be expected when transmitting and receiving with elements with greater surface areas. This effect is most obvious in the cases where fewer sources are used as this can be shown to result in significantly greater errors when using cylindrical elements. However, the difference between these error values becomes negligible as more sources are introduced. This suggests that the effect of running FWI using cylindrical elements can be mitigated to allow for high quality SoS maps to be recovered when compounding with a sufficiently high number of cylindrical sources. As shown in Figure 7.6, the lowest rms values measured for configurations with predicted run times less than 2 hours when

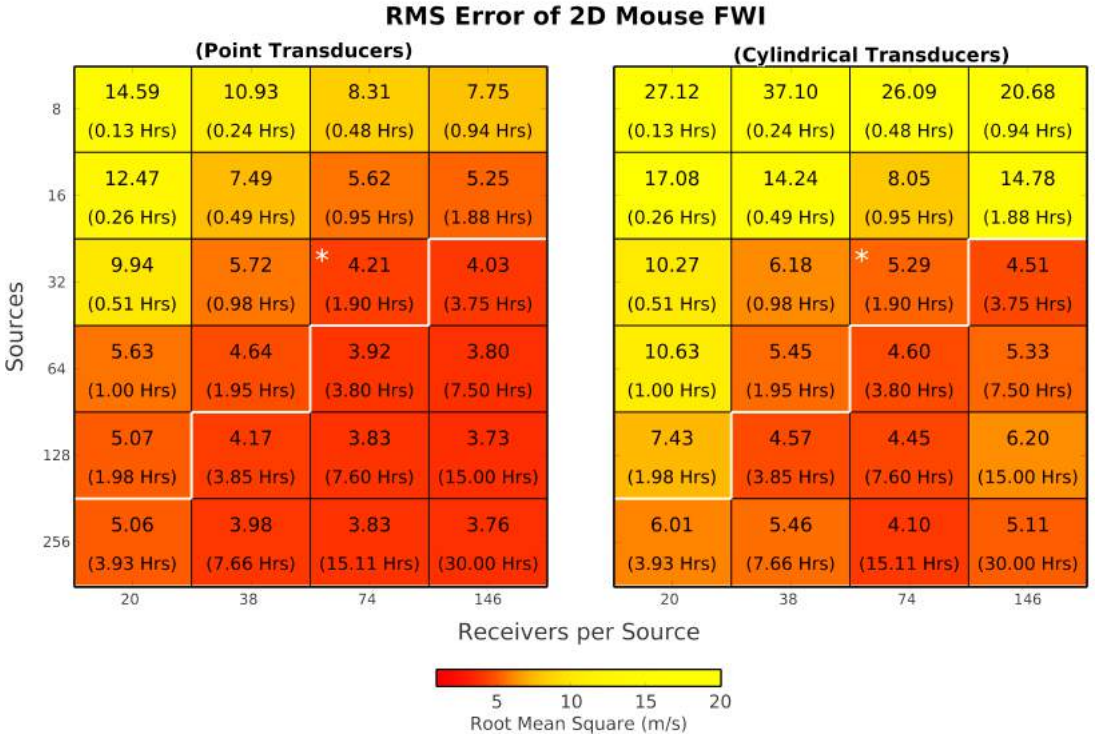


Figure 7.6: **Root mean square error and acquisition time plots for the resulting 2D FWI mouse head reconstructions for both point and cylindrical P4-1 elements**. Configurations which had run times greater than 2 hours are indicated by being below the white line. The configurations which were found to have the lowest rms values with run times less than 2 hours are labelled with white asterisks.

point elements were used was 4.21 $ms^{-1}$ for a run time of 1 hour and 54 minutes. This was observed when a ring array consisting of 32 source elements and 74 receiving elements per source were used. Likewise, the same imaging sequence of 32 sources and 74 receivers per source gave the lowest rms error detected using cylindrical elements and selecting for run times less than 2 hours, which as shown in Figure 7.6 was found to be 5.29 $ms^{-1}$. For this reason, the cylindrical array configuration selected for imaging the mouse head in 3D *in silico* was designed to simulate the rotation of 32 source array positions around the imaging target, each with 74 receiver positions. In practise this would be comparable to a fixed ring of 96 array positions, of which a set of 32 equally distributed arrays would be set as source arrays. As each array position in this ring consists of 96 elements along the vertical axis, the full cylindrical array would have a maximum of 9,216 transducer elements (or 96 stacked ring arrays of 96 elements, each separated by a vertical

spacing of 2.95 x $10^{-4}$). By applying the same density of source and receiver elements determined from the grid search (i.e. the distance between adjacent source elements and between adjacent receiver elements), the total number of elements can be further reduced by applying the same spacing to select for subsets of elements in each array. This significantly reduces the memory required to store the 3D USCT data. Likewise this also significantly reduces the computational expense of both the numerical simulation to generate the tomographic data and when running 3D FWI to reconstruct the head model. Given that in the 2D plane each of the 32 sources element positions would have an approximate distance of 2.00 mm from each neighbouring source element, a subset of 15 of the 96 elements from each array could be selected as sources to ensure the same spacing between elements vertically. Likewise, given that each receiving element would be separated by a distance of 0.98 mm, a subset of 28 elements from each 96 element array can be selected as receivers. In total this gives a transducer array of 2688 elements equally distributed over the surface of a 20.00 mm wide, 28.32 mm long cylinder, of which a subset of 480 of these elements were selected as sources.

### 7.3.2 Small Animal 3D FWI Reconstructions

#### 3D FWI Reconstruction of a Mouse Skull

Given the optimised configuration for the cylindrical transducer array discussed in Section 7.3.1, simulations of small animal imaging problems could be performed to generate the 3D USCT data required to test the feasibility of the proposed imaging modality. When imaging the 2.5D phantom in Chapter 5, it was found that the P4-1 did not have sufficient low frequency signal to reconstruct the high velocity skull mimicking material. While mouse skull tissue is also known to be high relative to soft tissue (a longitudinal wave speed of 2425 m$s^{-1}$ [Liang et al., 2019]), mice skulls are significantly thinner than human skills and so have a smaller impact on the travel time of propagating ultrasound waves. It is therefore possible that FWI reconstructions will not be susceptible to cycle skipping when

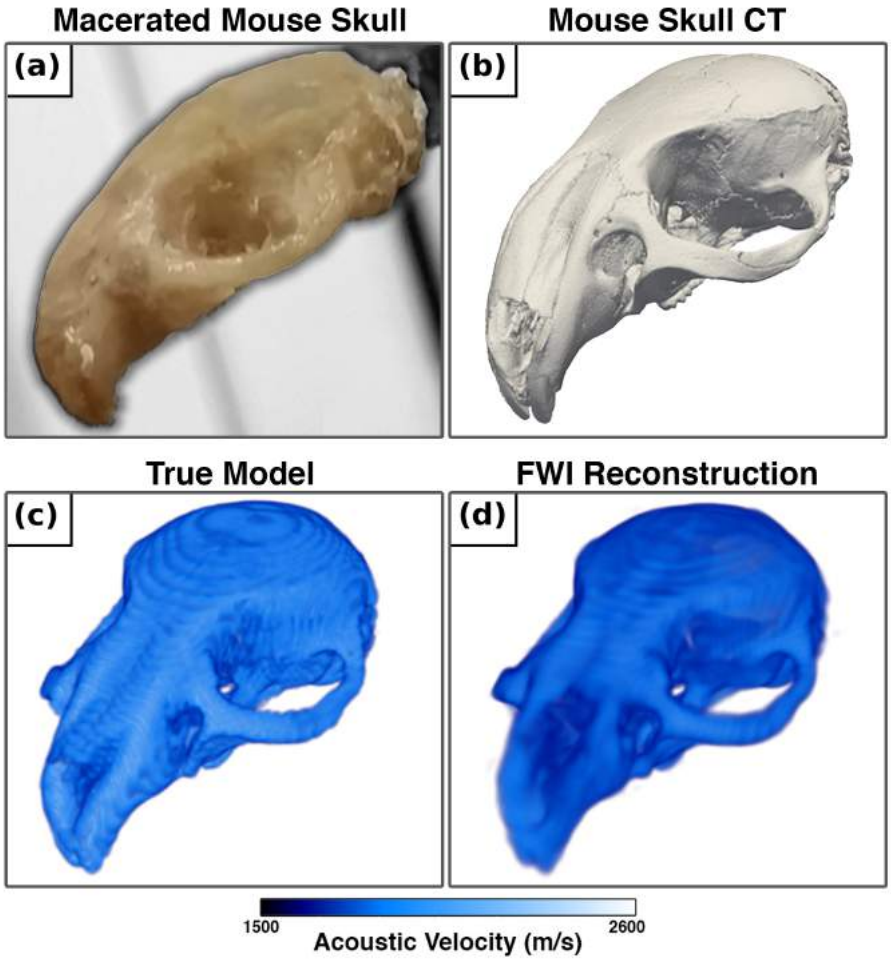


Figure 7.7: **Macerated mouse skull used to test the feasibility of reconstructing mouse skull tissue with full-waveform inversion**. (a) Photograph of macerated mouse skull. (b) CT acquisition of macerated skull (surface render). (c) Predicted acoustic model of skull derived from the CT acquisition. (d) Full-waveform inversion reconstruction of the mouse skull.

imaging without prior information about the mouse head (i.e. when running FWI using a starting model of homogeneous water SoS values) as the resulting lag after transmitting through the mouse head woudl be less than the half cycle of the lowest frequency band when imaging with P4-1 probes. To test this assumption, 3D FWI was first applied to reconstruct a full mouse skull *in silico*. To perform this inversion, a macerated mouse skull was imaged using a high resolution micro-CT scanner (XT H 225 CT scanner, Nikon, Tokyo, Japan) to provide an *in silico* imaging target. This skull can be seen in Figure 7.7a alongside the surface render of the CT mouse skull scan Figure 7.7b. Using the same method for deriving an acoustic SoS skull model using HU provided by CT acquisitions that was described

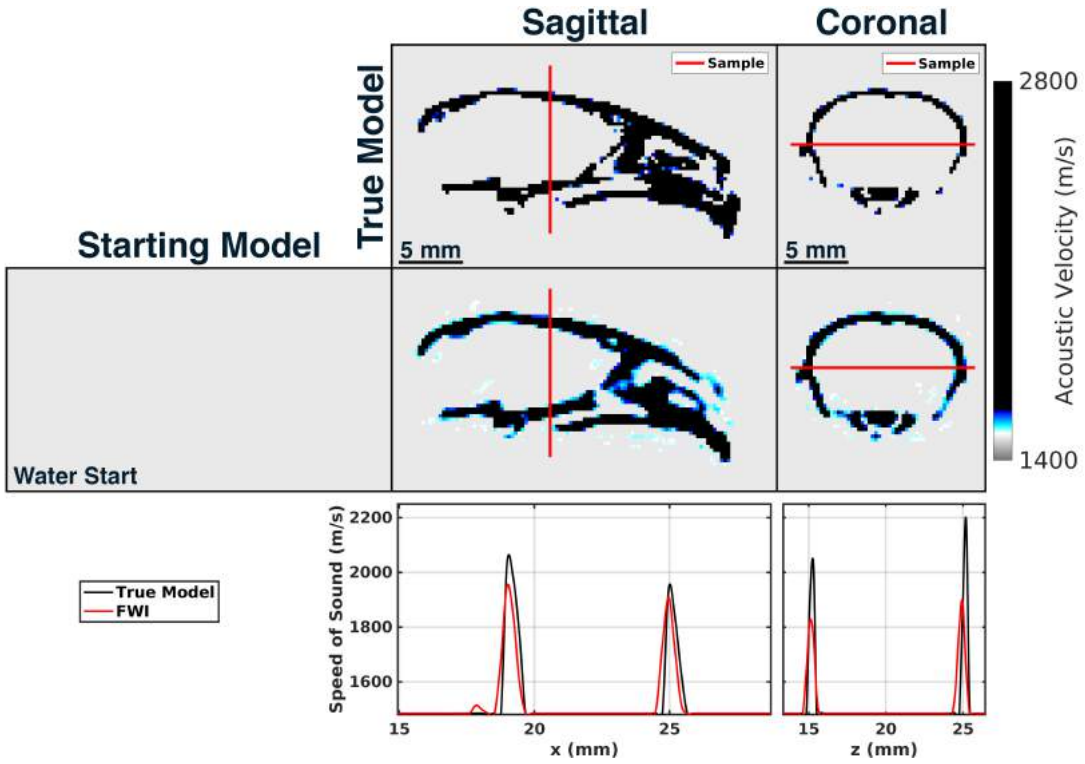


Figure 7.8: **Sagittal and coronal cross-sections of a synthetic full-waveform inversion reconstruction of an acoustic mouse skull model.** Alongside the reconstruction results are given the mouse skull true model and the starting model, which for this experiment was a homogeneous water starting model. Speed-of-sound value plots are shown to compare the true and reconstructed models using values sampled along the red line plots in each cross-section.

in Section 7.2.1, a acoustic SoS model of the *ex vivo* skull was calculated, as shown by the volume render in Figure 7.7c. Synthetic 3D USCT data from imaging this acoustic skull model was then generated by simulating a tomographic acquisition using the dual probe cylindrical array. The imaged acoustic skull model could then be used as the ground truth, or true model, in which reconstructed acoustic skull models can be compared. Finally, the FWI reconstruction of the skull can be seen in Figure 7.7d. This was acquired by running 3D FWI algorithm using the synthetic skull USCT dataset (frequency-stepping sequence, 0.55 to 2.50 MHz, iterations = 192). This *in silico* reconstruction was promising as it can be seen to match the true model of the skull closely. This suggests that the dual probe cylindrical array has a sufficient coverage of transducer elements to acquire data for fully recovering an imaging target the size of a mouse head. As the recovered model can be seen to closely match the geometry and SoS values of the true

model, this also suggests that cycle-skipping did not occur when recovering the mouse skull from water values, despite starting from a lower frequency band around 0.55 MHz.

A closer comparison between the true and the reconstructed skull models can be seen in Figure 7.8, which shows cross-sections of both models in the sagittal and coronal planes. Also seen are plots comparing SoS values using samples taken from the red line plot from each cross-section. The recovered skull can be seen to closely match the location, geometry and velocity values of the true model. However, the resolution of the recovered skull seems to be low, as indicated by the smooth gradient of high SoS tissue to the surrounding water SoS values. This is in contrast to the strong boundary between the true skull model and the surrounding water. This also means that the peak SoS values measured across the skull tissue are slightly lower in the recovered skull tissue compared to the true model, as can be seen in the SoS value sample plots. The effective change in travel time of waves moving directly through layers of skull may be similar in both models despite this smoothing. In which case it may be that model values in the centre of the skull will not be greatly affected. However, the impact of this smoothing and loss of the finer details of the skull will likely be greater for voxels as they get closer to skull and the uncertainty between skull tissue and the surrounding brain and water values increases. To determine the impact of this smoothed skull on the reconstruction of brain tissue, the acoustic mouse head model will be reconstructed by running FWI when the true skull is given in the FWI starting model and when no prior information of the skull is given (i.e. when the starting model only consists of water values).

### 3D FWI Reconstruction of a Mouse Brain and Skull

By using the cylindrical dual probe array to image the *in silico* mouse head model discussed in Section 7.2.1, a synthetic 3D USCT dataset of an acoustic mouse skull and brain imaging problem was generated by simulating a transcranial ultrasound tomography acquisition. Using the same approach used in Section 7.3.2, FWI

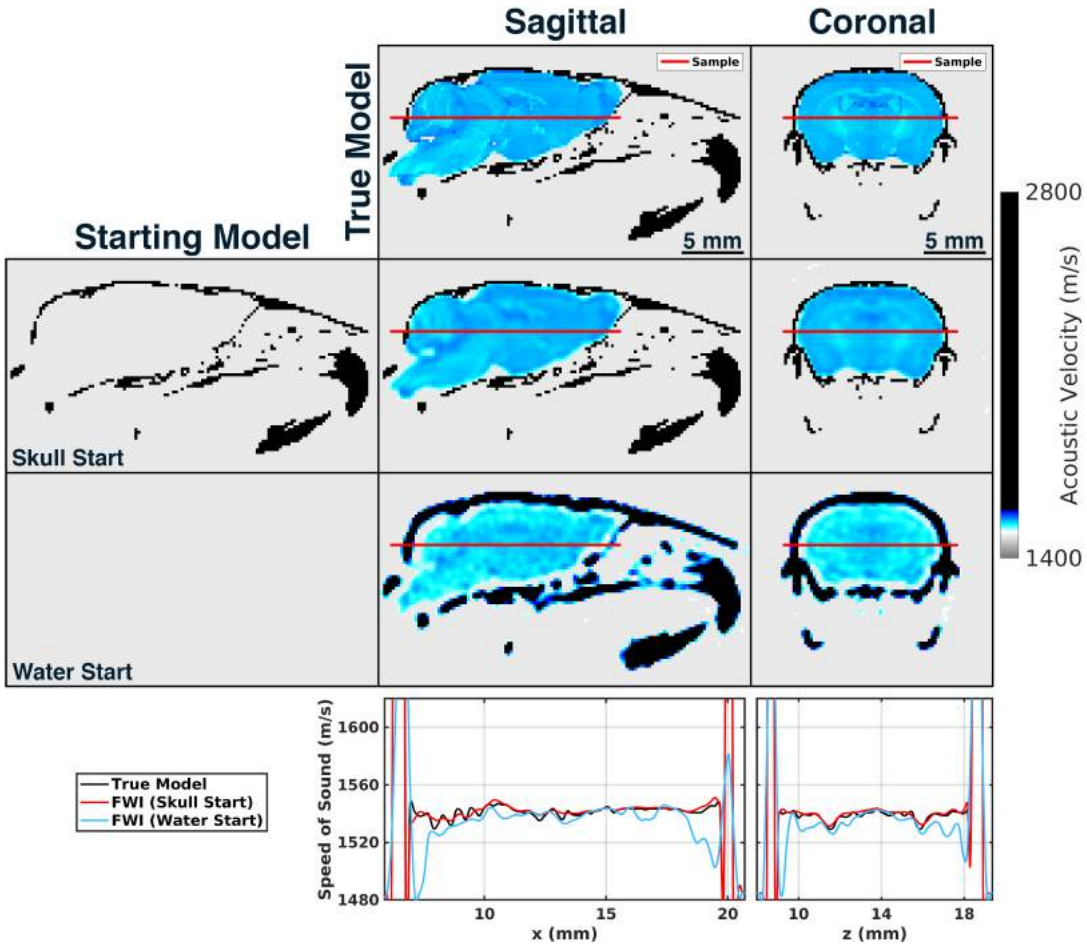


Figure 7.9: **FWI reconstruction of an acoustic*in silico* mouse skull model derived from a high resolution CT model, without surrounding tissue**

reconstructions of this skull and brain model were run using a 3D FWI algorithm (frequency-stepping sequence, 0.55 to 2.50 MHz, iterations = 192).

Reconstructions of the mouse skull and brain model were performed while using both a starting model containing the true mouse skull and a starting model containing only water SoS values and no prior information about the imaging target. By including the true skull in the starting, the inversion problem starts closer to the true velocity map of the problem, leaving only the brain model to be recovered. This inversion would therefore be expected to have a greater chance of tending towards the vicinity of the global minimum. When the water starting model is used, however, the imaging problem needs to recover both the brain and skull tissue, increasing the number of possible solutions in which the inversion problem could converge to.

As shown in Figure 7.11a, when FWI was run using the skull starting model, the brain model can be seen to have been successfully recovered when compared to the true model ground truth. High resolution features and accurate brain tissue SoS values can be seen in both sagittal and coronal cross-sections of this result and the sampled SoS value plots show that the recovered FWI matches well with the true model samples, albeit with some smoothing. When using the water starting model, distinct skull and brain tissues can be seen to have been recovered. However, while the position and geometry of the recovered FWI result are comparable to the True model, the recovered tissues are low resolution and it is not possible to clearly distinguish features of the brain. As shown in the SoS sample plots, even though the recovered SoS values of this FWI reconstruction do not closely match the features of the true model, the recovered SoS values do closely match the true model SoS values in the centre of the brain. However, the matching gets worse as the samples tend to decrease relative to the true model when moving towards the skull. Like in the results shown in Figure 7.7, the recovered skull model is smoothed relative to the true skull model. Together these results suggest that this imaging method is sufficient for recovering high resolution models of soft tissue such as the brain, but that the method is not able to sufficiently recover high resolutions of thin, high velocity material such as the skull which has strong boundaries to surrounding water and tissue. The smoothing error when reconstructing the skull then has a detrimental effect on the brain, resulting in lower velocity values in brain tissue near the skull and poor definition of brain features.

### 3D FWI Reconstruction of a Mouse Head

When attempting to recover the mouse skull and brain model described in Section 7.2.1, the only soft tissue included in the acoustic model was the brain. However, a real mouse head would be a more complex imaging target. This is because a real mouse head is composed of many other tissue besides the those

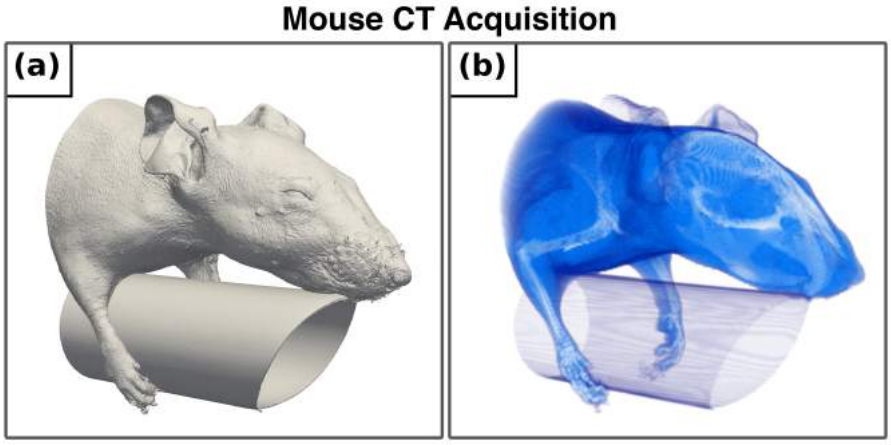


Figure 7.10: **Computed tomography scan of an *ex vivo* mouse head**. (a) Surface render of the mouse head. (b) Volume render of the mosue head.

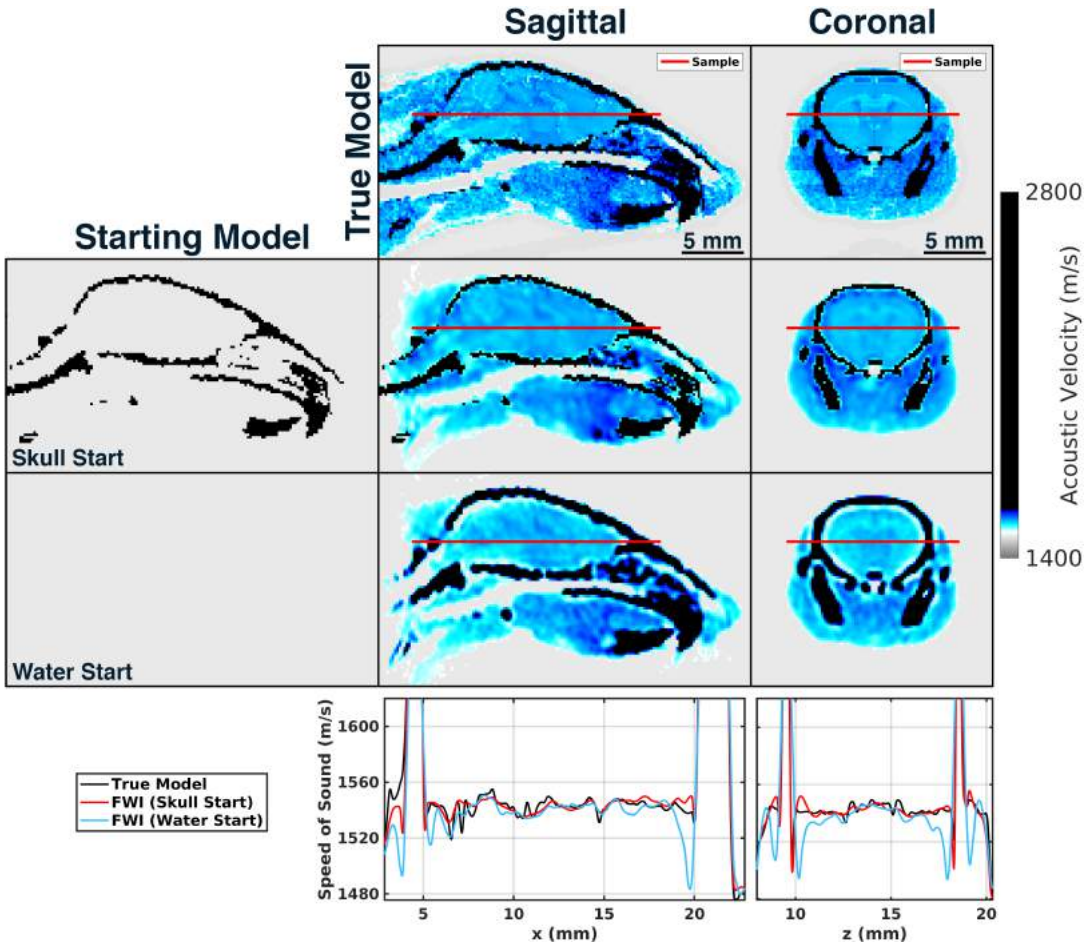


Figure 7.11: **FWI reconstruction of an acoustic *in silico* mouse skull model derived from a high resolution CT model, with surrounding tissue**

of the skull and brain, such as the surrounding muscle, skin, fat and sensory organs. To create a more anatomically correct mouse head model, an *ex-vivo*

mouse was scanned using a high resolution micro-CT scanner (XT H 225 CT scanner, Nikon, Tokyo, Japan) to acquire the density model of the mouse head, as shown by the surface and volume renders in Figure 7.10. Using the method for deriving acoustic models from CT data that was described in Section 7.2.1, this CT acquisition was used to generate a ground truth acoustic mouse head model to image using a simulation of the cylindrical dual probe array. However, CT is not well suited for imaging fine details in soft tissue. As a result the CT brain model was found to have limited high resolution detail. To correct this problem this mouse brain was replaced with the acoustic brain model derived from the MRI brain image discussed in Section 7.2.1 instead.

Using the same approach used in Section 7.3.2, FWI reconstructions using 3D USCT of the mouse head were run when using both starting models containing the true skull and a starting model containing only water SoS values, as shown in Figure 7.11. Much like the results seen in the mouse skull and brain case, the use of the skull starting model significantly improved the recovery of the mouse brain brain and once again some fine details of the brain can be observed. Likewise, when a water starting model was used a smoothed skull and brain model was recovered with little brain structure visible. However, even when the skull starting model was used the results are slightly further degraded compared to when only the brain and skull was present. This suggests that the impact of including the surrounding tissues and structure in the inversion problem may be detrimental to the recovery of the brain.

## 7.4 Conclusion

In this chapter, I have demonstrated through *in silico* imaging problems that it is feasible to generate a 3D ultrasound image of a mouse brain using FWI and a pair of low frequency clinical probes. It was shown that when a starting model containing the true skull was used that a high resolution 3D brain model can be recovered that closely matches the true mouse brain model. Unlike in the

previous FWI brain imaging problems considered in this thesis, it was also shown that this imaging modality could recover the complete skull and brain despite the limited frequency range of the P4-1 probes. However, as the recovered skull models tended to be smoothed compared to the true skull models, these reconstructions contained smoothed brain models without any visible high resolution brain structure. This suggests that for this method to be clinically useful, an inversion method which produces high resolution reconstructions of thin skull is required.

As only the first step in exploring the potential of this imaging modality, further studies with experimental validation is required.

# Chapter 8

# Conclusions and future work

## 8.1 Conclusions

The aim of this thesis was to develop technologies to overcome existing limitations of conventional ultrasound methods, particularly in transcranial imaging, by taking advantage of the recent advances in ultrasonics and computing.

In this thesis, a range of technologies and systems have been developed and studied. Firstly, techniques are developed and initially evaluated to image the mouse brain vasculature using a dual-frequency, ultrafast, contrast enhanced ultrasound imaging technique. Next, the focus of the research was moved to computed tomography using FWI. A sophisticated tomographic ultrasound data acquisition system was developed using computerised positioning system and two commercially available clinical low frequency imaging probes. A robust calibration methodology was applied to ensure that this system had precise positioning of the two probes and accurate models of the ultrasound wave-fields they generated for any given imaging experiment. A 2.5D brain phantom consisting of a soft brain tissue mimic surrounded by a hard, bone like skull mimic was developed. Having then devised a method for imaging this phantom using the dual probe acquisition system, I then demonstrated that it is feasible to image the brain through skull using FWI in an experimental phantom study. Furthermore, a deep learning

neural network was proposed to expand the bandwidth of the measurement data and improve the FWI image reconstruction. Finally, the FWI imaging is expanded to 3D on digital 3D mouse brain phantoms, and the feasibility of generating a 3D mouse brain image using FWI and existing commercial transducer is initially demonstrated.

The main contributions of this thesis include:

1. The first experimental demonstration of the feasibility of imaging brain through skull using FWI.
2. A novel method is developed based on deep learning using 2D CNN to expand the bandwidth of measurement data which is demonstrated to be able to improve FWI image reconstruction on experimental data.
3. The first demonstration of the feasibility of 3D FWI imaging of intact mouse brain through simulation.
4. The development of a 2.5D brain and skull mimicking phantom.
5. The development of the dual-transducer setup, and the demonstration of the importance of accurate transducer position calibration in ultrasound image reconstruction.
6. The development of a novel USCT acquisition system consisting of a pair of independently translated medical cardiac probes.

## 8.2 Future Work

Future work can expand in various directions. Firstly, 3D *in vivo* studies on imaging mouse brain using the technologies described in Chapter 7 would significantly strengthen conclusion of the study. Secondly, a clear direction is to develop a human helmet with distributed transducers so that a proper 3D FWI

reconstruction of human brain can be realised. Thirdly, the deep learning method proposed in this thesis could also be studied to investigate whether it can be used to fill any data acquisition gap in USCT datasets as it would be impossible to acquire, 360 data with a spherical acquisition system in practice.

# Bibliography

[ASP, 2014] (2014). Consolidated version of ASPA 1986 - GOV.UK. (January):1–40.

[Ahrens et al., 2013] Ahrens, M. B., Orger, M. B., Robson, D. N., Li, J. M., and Keller, P. J. (2013). Whole-brain functional imaging at cellular resolution using light-sheet microscopy. *Nat Methods*, 10(5):413–420.

[Allen et al., 2002] Allen, J. S., Damasio, H., and Grabowski, T. J. (2002). Normal neuroanatomical variation in the human brain: An MRI-volumetric study. *American Journal of Physical Anthropology*, 118(4):341–358.

[Anderson, 2010] Anderson, J. R. (2010). Cognitive psychology and its implications.

[Belzung and Lemoine, 2011] Belzung, C. and Lemoine, M. (2011). Criteria of validity for animal models of psychiatric disorders: focus on anxiety disorders and depression. *Biology of Mood & Anxiety Disorders*, 1(1):1–14.

[Bercoff et al., 2011] Bercoff, J., Montaldo, G., Loupas, T., Savery, D., M??zi??re, F., Fink, M., and Tanter, M. (2011). Ultrafast compound doppler imaging: Providing full blood flow characterization. *IEEE Transactions on Ultrasonics, Ferroelectrics, and Frequency Control*, 58(1):134–147.

[Broeders et al., 2018] Broeders, M. J., Allgood, P., Duffy, S. W., Hofvind, S., Nagtegaal, I. D., Paci, E., Moss, S. M., and Bucchi, L. (2018). The impact of mammography screening programmes on incidence of advanced breast cancer in Europe: A literature review. *BMC Cancer*, 18(1):1–11.

[Bunks et al., 1995] Bunks, C., Saleck, F. M., Zaleski, S., and Chavent, G. (1995). Multiscale seismic waveform inversion. *Geophysics*, 60(5):1457–1473.

[Calderon Agudo et al., 2018] Calderon Agudo, O., Guasch, L., Huthwaite, P., and Warner, M. (2018). 3D Imaging of the Breast Using Full-Waveform Inversion. *International Workshop on Medical Ultrasound Tomography*, (April):99–110.

[Camacho et al., 2012] Camacho, J., Medina, L., Cruza, J., Moreno Llamas, J. M., and Fritsch, C. (2012). Multimodal ultrasonic imaging for breast cancer detection. *Archives of Acoustics*, 37.

[Chan et al., 2007] Chan, E., Kovacevíc, N., Ho, S. K., Henkelman, R. M., and Henderson, J. T. (2007). Development of a high resolution three-dimensional surgical atlas of the murine head for strains 129S1/SvImJ and C57Bl/6J using magnetic resonance imaging and micro-computed tomography. *Neuroscience*, 144(2):604–615.

[Chee et al., 2016] Chee, A. J., Ho, C. K., Yiu, B. Y., and Yu, A. C. (2016). Walled Carotid Bifurcation Phantoms for Imaging Investigations of Vessel Wall Motion and Blood Flow Dynamics. *IEEE Transactions on Ultrasonics, Ferroelectrics, and Frequency Control*, 63(11):1852–1864.

[Chen et al., 2018] Chen, Z., Nie, S., Wu, T., and Healey, C. G. (2018). High resolution face completion with multiple controllable attributes via fully end-to-end progressive generative adversarial networks. *arXiv*, 1(1).

[Choi et al., 2010] Choi, J. H., Koch, K. P., Poppendieck, W., Lee, M., and Shin, H.-S. (2010). High resolution electroencephalography in freely moving mice. *Journal of neurophysiology*, 104(3):1825–1834.

[CIRS, 2014] CIRS (2014). Multi-Modality Breast Biopsy and Sonographic Trainer. Brochure.

[Dahlen, 2004] Dahlen, F. A. (2004). Resolution limit of traveltime tomography. *Geophysical Journal International*, 157(1):315–331.

[Delannoy et al., 1979] Delannoy, B., Torguet, R., Bruneel, C., Bridoux, E., Rouvaen, J. M., and Lasota, H. (1979). Acoustical image reconstruction in parallel-processing analog electronic systems. *Journal of Applied Physics*, 50(5):3153–3159.

[Demené et al., 2015] Demené, C., Deffieux, T., Pernot, M., Osmanski, B. F., Biran, V., Gennisson, J. L., Sieu, L. A., Bergel, A., Franqui, S., Correas, J. M., Cohen, I., Baud, O., and Tanter, M. (2015). Spatiotemporal Clutter Filtering of Ultrafast Ultrasound Data Highly Increases Doppler and fUltrasound Sensitivity. *IEEE Transactions on Medical Imaging*, 34(11):2271–2285.

[Doinikov and Dayton, 2007] Doinikov, A. A. and Dayton, P. A. (2007). Nonlinear dynamics of lipid-shelled ultrasound microbubble contrast agents. In *WIT Transactions on Engineering Sciences*, volume 56, pages 261–270.

[Droste and Metz, 2004] Droste, D. W. and Metz, R. J. (2004). Clinical utility of echocontrast agents in neurosonology. *Neurological research*, 26(7):754–759.

[Duffy et al., 2020] Duffy, S. W., Tabár, L., Yen, A. M. F., Dean, P. B., Smith, R. A., Jonsson, H., Törnberg, S., Chen, S. L. S., Chiu, S. Y. H., Fann, J. C. Y., Ku, M. M. S., Wu, W. Y. Y., Hsu, C. Y., Chen, Y. C., Svane, G., Azavedo, E., Grundström, H., Sundén, P., Leifland, K., Frodis, E., Ramos, J., Epstein, B., Åkerlund, A., Sundbom, A., Bordás, P., Wallin, H., Starck, L., Björkgren, A., Carlson, S., Fredriksson, I., Ahlgren, J., Öhman, D., Holmberg, L., and Chen, T. H. H. (2020). Mammography screening reduces rates of advanced and fatal breast cancers: Results in 549,091 women. *Cancer*, 126(13):2971–2979.

[Errico et al., 2016] Errico, C., Osmanski, B.-f., Pezet, S., Couture, O., Lenkei, Z., and Tanter, M. (2016). NeuroImage Transcranial functional ultrasound imaging of the brain using microbubble-enhanced ultrasensitive Doppler. *NeuroImage*, 124:752–761.

[Errico et al., 2015] Errico, C., Pierre, J., Pezet, S., Desailly, Y., Lenkei, Z., Couture, O., and Tanter, M. (2015). Ultrafast ultrasound localization microscopy for deep super-resolution vascular imaging. *Nature*, 527(7579):499–502.

[Ferlay et al., 2019] Ferlay, J., Colombet, M., Soerjomataram, I., Mathers, C., Parkin, D. M., Piñeros, M., Znaor, A., and Bray, F. (2019). Estimating the global cancer incidence and mortality in 2018: GLOBOCAN sources and methods. *International Journal of Cancer*, 144(8):1941–1953.

[Filipík et al., 2012] Filipík, A., Jan, J., and Peterlík, I. (2012). Time-of-flight based calibration of an ultrasonic computed tomography system. *Radioengineering*, 21(1):533–544.

[Gessner et al., 2010] Gessner, R., Lukacs, M., Lee, M., Cherin, E., Foster, F. S., and Dayton, P. A. (2010). High-resolution, high-contrast ultrasound imaging using a prototype dual-frequency transducer: In vitro and in vivo studies. *IEEE Transactions on Ultrasonics, Ferroelectrics, and Frequency Control*, 57(8):1772–1781.

[Gessner et al., 2013] Gessner, R. C., Frederick, C. B., Foster, F. S., and Dayton, P. A. (2013). Acoustic angiography: A new imaging modality for assessing microvasculature architecture. *International Journal of Biomedical Imaging*, 2013.

[Greenleaf et al., 1974] Greenleaf, J. F., Johnson, S. A., Lee, S. L., Hermant, G. T., and Woo, E. H. (1974). *Algebraic Reconstruction of Spatial Distributions of Acoustic Absorption within Tissue from Their Two-Dimensional Acoustic Projections*, pages 591–603. Springer US, Boston, MA.

[Guasch et al., 2020] Guasch, L., Calderón Agudo, O., Tang, M. X., Nachev, P., and Warner, M. (2020). Full-waveform inversion imaging of the human brain. *npj Digital Medicine*, 3(1):1–12.

[Gupta et al., 2016] Gupta, P., Sodhi, K. S., Saxena, A. K., Khandelwal, N., and Singhi, P. (2016). Neonatal cranial sonography: A concise review for clinicians. *Journal of Pediatric Neurosciences*, 11(1):7–13.

[Harvey et al., 2013] Harvey, J. A., Gard, C. C., Miglioretti, D. L., Yankaskas, B. C., Kerlikowske, K., Buist, D. S., Geller, B. A., and Onega, T. L. (2013).

Reported mammographic density: Film-screen versus digital acquisition. *Radiology*, 266(3):752–758.

[Hasgall et al., 2012] Hasgall, P. A., Neufeld, E., Neufeld, E., Gosselin, M.-C., Klingenbock, A., Kuster, N., Hasgall, P. A., and Gosselin, M.-C. (2012). Itis database for thermal and electromagnetic parameters of biological tissues.

[Hopp et al., 2014] Hopp, T., Šroba, L., Zapf, M., Dapp, R., Kretzek, E., Gemmeke, H., and Ruiter, N. V. (2014). Breast imaging with 3D ultrasound computer tomography: Results of a first in-vivo study in comparison to MRI images. *Lecture Notes in Computer Science (including subseries Lecture Notes in Artificial Intelligence and Lecture Notes in Bioinformatics)*, 8539 LNCS:72–79.

[Hornik et al., 1989] Hornik, K., Stinchcombe, M., and White, H. (1989). Multilayer feedforward networks are universal approximators. *Neural Networks*, 2(5):359–366.

[Hoyer et al., 2014] Hoyer, C., Gass, N., Weber-Fahr, W., and Sartorius, A. (2014). Advantages and challenges of small animal magnetic resonance imaging as a translational tool. *Neuropsychobiology*, 69(4):187–201.

[Huthwaite et al., 2010] Huthwaite, P., Simonetti, F., and Huang, L. (2010). The different structural scales of the breast and their impact on time-of-flight and diffraction tomography. *Medical Imaging 2010: Ultrasonic Imaging, Tomography, and Therapy*, 7629(March 2010):76290L.

[Iacono et al., 2015] Iacono, M. I., Neufeld, E., Akinnagbe, E., Bower, K., Wolf, J., Oikonomidis, I. V., Sharma, D., Lloyd, B., Wilm, B. J., Wyss, M., Pruessmann, K. P., Jakab, A., Makris, N., Cohen, E. D., Kuster, N., Kainz, W., and Angelone, L. M. (2015). MIDA: A multimodal imaging-based detailed anatomical model of the human head and neck. *PLoS ONE*, 10(4).

[Igel, 2017] Igel, H. (2017). *Computational Seismology*.

[Kaderli et al., 2015] Kaderli, J., McChesney, M. D., and Minkoff, S. E. (2015). Microseismic event estimation in noisy data via full waveform inversion. *SEG Technical Program Expanded Abstracts*, 34:1159–1164.

[Kolb et al., 2002] Kolb, T. M., Lichy, J., and Newhouse, J. H. (2002). Comparison of the performance of screening mammography, physical examination, and breast US and evaluation of factors that influence them: An analysis of 27,825 patient evaluations. *Radiology*, 225(1):165–175.

[Komatsu and Gonsalves, 2020] Komatsu, R. and Gonsalves, T. (2020). Comparing U-Net Based Models for Denoising Color Images. *Ai*, 1(4):465–487.

[Kondylis et al., 2014] Kondylis, E. D., Wozny, T. A., Lipski, W. J., Popescu, A., DeStefino, V. J., Esmaeili, B., Raghu, V. K., Bagic, A., and Richardson, R. M. (2014). Detection of high-frequency oscillations by hybrid depth electrodes in standard clinical intracranial EEG recordings. *Frontiers in Neurology*, 5 AUG(August):1–10.

[Kousaka et al., 2016] Kousaka, J., Nakano, S., Ando, T., Tetsuka, R., Fujii, K., Yoshida, M., Shiomi-Mouri, Y., Goto, M., Imai, Y., Imai, T., Fukutomi, T., Katsuda, E., Ishiguchi, T., and Arai, O. (2016). Targeted sonography using an image fusion technique for evaluation of incidentally detected breast lesions on chest CT: a pilot study. *Breast Cancer*, 23(2):301–309.

[Kruse and Ferrara, 2005] Kruse, D. E. and Ferrara, K. W. (2005). A new imaging strategy using wideband transient response of ultrasound contrast agents. *Ieee Transactions on Ultrasonics Ferroelectrics and Frequency Control*, 52(8):1320–1329.

[Kruse et al., 2003] Kruse, D. E., Yeh, C. K., and Ferrara, K. W. (2003). A new imaging strategy utilizing wideband transient response of ultrasound contrast agents. *Proceedings of the IEEE Ultrasonics Symposium*, 2(8):1081–1085.

[Lahti et al., 1998] Lahti, K. M., Ferris, C. F., Li, F., Sotak, C. H., and King, J. a. (1998). Imaging brain activity in conscious animals using functional MRI. *Journal of neuroscience methods*, 82(1):75–83.

[Levin, 1984] Levin, S. A. (1984). Principle of reverse-time migration. *Geophysics*, 49(5):581–583.

[Li et al., 2009] Li, C., Duric, N., Littrup, P., and Huang, L. (2009). In vivo Breast Sound-Speed Imaging with Ultrasound Tomography. *Ultrasound in Medicine and Biology*, 35(10):1615–1628.

[Li and Demanet, 2016] Li, Y. E. and Demanet, L. (2016). Full-waveform inversion with extrapolated low-frequency data. *Geophysics*, 81(6):R339–R348.

[Liang et al., 2019] Liang, B., Liu, W., Zhan, Q., Li, M., Zhuang, M., Liu, Q. H., and Yao, J. (2019). Impacts of the murine skull on high-frequency transcranial photoacoustic brain imaging. *Journal of Biophotonics*, 12(7):1–10.

[Logothetis, 2008] Logothetis, N. K. (2008). What we can do and what we cannot do with fMRI. *Nature*, 453(7197):869–878.

[Lou et al., 2017] Lou, Y., Zhou, W., Matthews, T. P., Appleton, C. M., and Anastasio, M. A. (2017). Generation of anatomically realistic numerical phantoms for photoacoustic and ultrasonic breast imaging. *Journal of Biomedical Optics*, 22(4):041015.

[Macé et al., 2011] Macé, E., Montaldo, G., Cohen, I., Baulac, M., Fink, M., and Tanter, M. (2011). Functional ultrasound imaging of the brain. *Nature Methods*, 8(8):662–664.

[Macé et al., 2013] Macé, E., Montaldo, G., Osmanski, B. F., Cohen, I., Fink, M., and Tanter, M. (2013). Functional ultrasound imaging of the brain: Theory and basic principles. *IEEE Transactions on Ultrasonics, Ferroelectrics, and Frequency Control*, 60(3):492–506.

[Madjar, 2010] Madjar, H. (2010). Role of breast ultrasound for the detection and differentiation of breast lesions. *Breast Care*, 5(2):109–114.

[Manbachi and Cobbold, 2011] Manbachi, A. and Cobbold, R. S. (2011). Development and application of piezoelectric materials for ultrasound generation and detection. *Ultrasound*, 19(4):187–196.

[Mast, 2000] Mast, T. D. (2000). Empirical relationships between acoustic parameters in human soft tissues. *Acoustic Research Letters Online*, 1(2000):37–42.

[Medina et al., 2016] Medina, L., Salido, N., Camacho, J., Pérez-Liva, M., Lopez Herraiz, J., and Udías, J. (2016). Refraction correction in full angle spatial image compounding. pages 1–4.

[Miglioretti et al., 2016] Miglioretti, D. L., Lange, J., Broek, J. J. V. D., Lee, I., Ravesteyn, N. T. V., Ritley, D., Fenton, J. J., Melnikow, J., and De, H. J. (2016). HHS Public Access. 164(4):205–214.

[Miller and Wilson, 2008] Miller, E. K. and Wilson, M. A. (2008). All My Circuits: Using Multiple Electrodes to Understand Functioning Neural Networks. *Neuron*, 60(3):483–488.

[Montaldo et al., 2009] Montaldo, G., Tanter, M., Bercoff, J., Benech, N., and Fink, M. (2009). Coherent plane-wave compounding for very high frame rate ultrasonography and transient elastography. *IEEE Transactions on Ultrasonics, Ferroelectrics, and Frequency Control*, 56(3):489–506.

[Naqvi et al., 2013] Naqvi, J., Yap, K. H., Ahmad, G., and Ghosh, J. (2013). Transcranial Doppler ultrasound: A review of the physical principles and major applications in critical care. *International Journal of Vascular Medicine*, 2013(March).

[O'Reilly and Hynynen, 2013] O'Reilly, M. a. and Hynynen, K. (2013). A super-resolution ultrasound method for brain vascular mapping. *Medical physics*, 40(11):110701.

[Pérez-Liva et al., 2017] Pérez-Liva, M., Herraiz, J. L., Udías, J. M., Miller, E., Cox, B. T., and Treeby, B. E. (2017). Time domain reconstruction of sound speed and attenuation in ultrasound computed tomography using full wave

inversiona). *The Journal of the Acoustical Society of America*, 141(3):1595–1604.

[Perez-Liva et al., 2020] Perez-Liva, M., Udías, J. M., Camacho, J., Merčep, E., Deán-Ben, X. L., Razansky, D., and Herraiz, J. L. (2020). Speed of sound ultrasound transmission tomography image reconstruction based on Bézier curves. *Ultrasonics*, 103(March 2019):106097.

[Peters et al., 1998] Peters, M., Jäncke, L., Staiger, J. F., Schlaug, G., Huang, Y., and Steinmetz, H. (1998). Unsolved problems in comparing brain sizes in homo sapiens. *Brain and Cognition*, 37(2):254–285.

[Pinto, 2010] Pinto, F. P. C. (2010). Signal Processing in Space and Time - A Multidimensional Fourier Approach [PhD Thesis]. *École Polytechnique Fédérale De Lausanne*, 4871.

[Razimi et al., 2019] Razimi, U. N. A., Ahmed, F. Y., and Mustapa, N. R. (2019). ATM reporting system. *2019 IEEE 9th International Conference on System Engineering and Technology, ICSET 2019 - Proceeding*, pages 166–171.

[Robins, 2016] Robins, T. (2016). *Development of Pulse Inversion Functional Ultrasound Towards the Functional Imaging of the Brain in Freely-Moving Subjects*. PhD thesis.

[Ronneberger et al., 2015] Ronneberger, O., Fischer, P., and Brox, T. (2015). U-net: Convolutional networks for biomedical image segmentation. *Lecture Notes in Computer Science (including subseries Lecture Notes in Artificial Intelligence and Lecture Notes in Bioinformatics)*, 9351:234–241.

[Russell and Burch, 1959] Russell, W. M. S. and Burch, R. L. (1959). *The principles of humane experimental technique [by] W.M.S. Russell and R.L. Burch*. Methuen London.

[Salido et al., 2016] Salido, N., Medina, L., and Camacho, J. (2016). Full angle spatial compound of arfi images for breast cancer detection. *Ultrasonics*, 71.

[Sandrin et al., 1999] Sandrin, L., Catheline, S., Tanter, M., Hennequin, X., and Fink, M. (1999). Time-Resolved Pulsed Elastography with Ultrafast Ultrasonic Imaging. *Ultrasonic Imaging*, 21(4):259–272.

[Schambach et al., 2009] Schambach, S. J., Bag, S., Steil, V., Isaza, C., Schilling, L., Groden, C., and Brockmann, M. A. (2009). Ultrafast high-resolution in vivo volume-CTA of mice cerebral vessels. *Stroke*, 40(4):1444–1450.

[Schulz et al., 2011] Schulz, D., Southekal, S., Junnarkar, S. S., Pratte, J.-F., Purschke, M. L., Stoll, S. P., Ravindranath, B., Maramraju, S. H., Krishnamoorthy, S., Henn, F. A., O'Connor, P., Woody, C. L., Schlyer, D. J., and Vaska, P. (2011). Simultaneous assessment of rodent behavior and neurochemistry using a miniature positron emission tomograph. *Nature methods*, 8(4):347–352.

[Sharan et al., 2018] Sharan, S., Kumar, R., Dumani, D. S., Louboutin, M., Wang, R., Emelianov, S., and Herrmann, F. J. (2018). Sparsity-Promoting Photoacoustic Imaging with Source Estimation. *IEEE International Ultrasonics Symposium, IUS*, 2018-October(October).

[Sharan et al., 2019] Sharan, S., Wang, R., and Herrmann, F. J. (2019). Fast sparsity-promoting microseismic source estimation. *Geophysical Journal International*, 216(1):164–181.

[Sheeran et al., 2011] Sheeran, P. S., Luois, S., Dayton, P. A., and Matsunaga, T. O. (2011). Formulation and acoustic studies of a new phase-shift agent for diagnostic and therapeutic ultrasound. *Langmuir*, 27(17):10412–10420.

[Smith et al., 1978] Smith, S. W., Von Ramm, O. T., Kisslo, J. A., and Thurstone, F. L. (1978). Real time ultrasound tomography of the adult brain. *Stroke*, 9(2):117–122.

[Sollini and Chadderton, 2016] Sollini, J. and Chadderton, P. (2016). Comodulation enhances signal detection via priming of auditory cortical circuits. *Journal of Neuroscience*, 36(49):12299–12311.

[Sun and Demanet, 2019] Sun, H. and Demanet, L. (2019). Extrapolated full waveform inversion with deep learning. *arXiv*.

[Sun and Demanet, 2020] Sun, H. and Demanet, L. (2020). Extrapolated full-waveform inversion with deep learning. *GEOPHYSICS*, 85(3):R275–R288.

[Szabo, 2014] Szabo, T. L. (2014). Diagnostic ultrasound imaging: Inside out (second edition). In Szabo, T. L., editor, *Diagnostic Ultrasound Imaging: Inside Out (Second Edition)*, page iv. Academic Press, Boston, second edition edition.

[Tan et al., 2015] Tan, W. Y., Steiner, T., and Ruiter, N. V. (2015). Newton's method based self calibration for a 3D ultrasound tomography system. *2015 IEEE International Ultrasonics Symposium, IUS 2015*, pages 0–3.

[Tanter and Fink, 2014] Tanter, M. and Fink, M. (2014). Ultrafast imaging in biomedical ultrasound. *IEEE Transactions on Ultrasonics, Ferroelectrics, and Frequency Control*, 61(1):102–119.

[Tarantola, 1984] Tarantola, A. (1984). in the Acoustic Approximation. *Geophysics*, 49(8):1259–1266.

[Thurber and Ritsema, 2018] Thurber, C. and Ritsema, J. (2018). Seismic Tomography A conceptual model of the Earth ' s crust of Icelandic type.

[Van Veen and Buckley, 1988] Van Veen, B. D. and Buckley, K. M. (1988). Beamforming: A Versatile Approach to Spatial Filtering. *IEEE ASSP Magazine*, 5(2):4–24.

[Vaseghi, 2008] Vaseghi, S. V. (2008). *Advanced Digital Signal Processing and Noise Reduction*. John Wiley & Sons, New York.

[Vincent et al., 2010] Vincent, T. J., Thiessen, J. D., Kurjewicz, L. M., Germscheid, S. L., Turner, A. J., Zhilkin, P., Alexander, M. E., and Martin, M. (2010). Longitudinal Brain Size Measurements in App/Ps1 Transgenic Mice. *Magnetic Resonance Insights*, 4:MRI.S5885.

[Virieux and Operto, 2009] Virieux, J. and Operto, S. (2009). An overview of full-waveform inversion in exploration geophysics. *GEOPHYSICS*, 74(6):WCC1–WCC26.

[Waerzeggers et al., 2010] Waerzeggers, Y., Monfared, P., Viel, T., Winkeler, A., and Jacobs, A. H. (2010). Mouse models in neurological disorders: Applications of non-invasive imaging. *Biochimica et Biophysica Acta - Molecular Basis of Disease*, 1802(10):819–839.

[Walter et al., 2009] Walter, M., Henning, A., Grimm, S., Schulte, R. F., Beck, J., Dydak, U., Schnepf, B., Boeker, H., Boesiger, P., and Northoff, G. (2009). The relationship between aberrant neuronal activation in the pregenual anterior cingulate, altered glutamatergic metabolism, and anhedonia in major depression. *Archives of General Psychiatry*, 66(5):478–486.

[Warner et al., 2013] Warner, M., Ratcliffe, A., Nangoo, T., Morgan, J., Umpleby, A., Shah, N., Vinje, V., Štekl, I., Guasch, L., Win, C., Conroy, G., and Bertrand, A. (2013). Anisotropic 3D full-waveform inversion. *Geophysics*, 78(2).

[Williamson, 1991] Williamson, P. R. (1991). A guide to the limits of resolution imposed by scattering in ray tomography. *Geophysics*, 56(2):202–207.

[Williamson and Worthington, 1993] Williamson, P. R. and Worthington, M. H. (1993). Resolution limits in ray tomography due to wave behavior: numerical experiments. *Geophysics*, 58(5):727–735.

[Yao et al., 2015] Yao, J., Wang, L., Yang, J.-M., Maslov, K. I., Wong, T. T. W., Li, L., Huang, C.-H., Zou, J., and Wang, L. V. (2015). High-speed label-free functional photoacoustic microscopy of mouse brain in action. *Nature methods*, 12(5):407–10.

[Yao et al., 2018] Yao, W., Zeng, Z., Lian, C., and Tang, H. (2018). Pixel-wise regression using U-Net and its application on pansharpening. *Neurocomputing*, 312:364–371.

[Yu et al., 2012] Yu, X., Glen, D., Wang, S., Dodd, S., Hirano, Y., Saad, Z., Reynolds, R., Silva, A. C., and Koretsky, A. P. (2012). Direct imaging of macrovascular and microvascular contributions to BOLD fMRI in layers IV-V of the rat whisker-barrel cortex. *NeuroImage*, 59(2):1451–1460.

[Yu et al., 2010] Yu, X., Wang, S., Chen, D. Y., Dodd, S., Goloshevsky, A., and Koretsky, A. P. (2010). 3D mapping of somatotopic reorganization with small animal functional MRI. *NeuroImage*, 49(2):1667–1676.

[Zhang et al., 2003] Zhang, H., Thurber, C. H., and Rowe, C. A. (2003). Automatic p-wave arrival detection and picking with multiscale wavelet analysis for single-component recordings. *Bulletin of the Seismological Society of America*, 93:1904–1912.

[Zhang, 2016] Zhang, J. (2016). Pulse-Echo Ultrasonic Inspection Defect detection , classification , and characterization using ultrasound Ceramic-Matrix Composites Development and Validation of Bonded Composite Doubler Repairs for Com- mercial Aircraft.

[Zhou, 2014] Zhou, H.-W. (2014). *Practical Seismic Data Analysis*.

[Zhu et al., 2021] Zhu, W., Xu, K., Darve, E., Biondi, B., and Beroza, G. C. (2021). Integrating Deep Neural Networks with Full-waveform Inversion: Reparametrization, Regularization, and Uncertainty Quantification. *Geophysics*, pages 1–103.